



**HAL**  
open science

# Internal dynamics of heme-based sensor proteins studied using advanced time-resolved optical spectroscopy

Laura Lobato

## ► To cite this version:

Laura Lobato. Internal dynamics of heme-based sensor proteins studied using advanced time-resolved optical spectroscopy. Biological Physics [physics.bio-ph]. Ecole Polytechnique X, 2013. English. NNT: . pastel-00866894

**HAL Id: pastel-00866894**

**<https://pastel.hal.science/pastel-00866894>**

Submitted on 27 Sep 2013

**HAL** is a multi-disciplinary open access archive for the deposit and dissemination of scientific research documents, whether they are published or not. The documents may come from teaching and research institutions in France or abroad, or from public or private research centers.

L'archive ouverte pluridisciplinaire **HAL**, est destinée au dépôt et à la diffusion de documents scientifiques de niveau recherche, publiés ou non, émanant des établissements d'enseignement et de recherche français ou étrangers, des laboratoires publics ou privés.

PhD THESIS AT THE ECOLE POLYTECHNIQUE

Speciality :

**Optics**

Defended by:

**Laura Lobato Bailón**

To obtain the title of PhD in Physics

**Internal dynamics of heme-based  
sensor proteins studied using  
advanced time-resolved optical  
spectroscopy**

Defended on 23<sup>rd</sup> September, 2013

Jury:

*Reviewers :* Catherine BERTHOMIEU

Wolfgang NITSCHKE

*Examinators :* Michael WILSON

Emmanuelle SCHMITT

*Advisor :* Marten VOS

*Co-Advisor :* Ursula LIEBL

**Laboratoire d'Optique et Biosciences, INSERM U696,  
CNRS UMR 7645, Ecole Polytechnique**

*A mi padres y mi hermana,  
por su devoción*

## Acknowledgments

I would like to thank Catherine Berthomieu, Wolfgang Nitschke, Michael Wilson and Emmanuelle Schmitt for having accepted to be part of the jury.

I am very thankful to my supervisor, Marten H. Vos, for largely providing me with all the means to successfully fulfill this thesis. Without him this work would not have been possible.

I am also very grateful to Ursula Liebl, for her good remarks in the biochemistry part of the project and also for encouraging me in key moments of this thesis.

I owe a deep gratitude to Latifa Bouzahir, for her infinite help with the biological issues, from my first day in the lab to the last one during three years, and also for the good moments we shared.

Thank you very much to Sergey Laptinok, because he made available his support in a number of ways with the experiments, the computer issues and the analysis of the data.

I am grateful to Jean-Christophe Lambry for the computational calculations provided. I would also like to thank François Hache and Lucille Mendonça for their interest in my project and their valuable help with the CD experiments.

Thank you to Xavier Solinas for his efficient help with the "burnt motor". Thank you also to Jean-Marc Sintès for the mechanical instrumentation provided. I would also like to thank Laure Lachapelle and Christelle Français for making easy all the administrative issues.

Thank you very much to Rivo Ramodiharilafy and Laura Antonucci for the good conversations and laughs we shared. I would also like to show my gratitude to all the doctorants in the LOB and people who supported me in any aspect during the completion of this project.

I am thankful to Jean-Louis Martin for allowing me to develop my thesis in the LOB.

Agradezco profundamente a la Obra Social de "La Caixa" que apostara por mí y me financiara los dos primeros años de mi tesis en Francia.

Me gustaría expresar mi más sincero agradecimiento a los profesores Juan Campos y María Yzuel por descubrirme la ciencia, creer en mí y animarme a realizar este proyecto desde Barcelona. No pude haber tenido más suerte al encontrarlos.

Mil gracias, Edu y Juan Antonio, por los miércoles de Polytechnique. Por esos momentos de risas sinceras y postres, que seguro anhelaré.

I a vosaltres tres, Josep, Alba i Àngel. Josep, perquè som uns autèntics corredors de fondo. Alba, perquè molts pocs cops la llunyania física amb una persona implica sentir-se tan a prop d'esperit. Àngel, deixa'm resumir-ho així: eXcel·lent companyia la teva, a Barcelona, a París, i on sigui amic meu!

Pau, no hi ha res millor que una llarga amistat que comença amb una polka durant les festes de l'Autònoma i que evoluciona a mesura que ens fem grans. Guillem, no és gens fàcil estar present cada cop et necessito, i tu sempre hi ets. Txus, necessito fer un café!!! Cris, gràcies per aquestes ganes bojes que compartíem de voler canviar el món des del seient d'un cotxe, amb la inocència dels 18 anys. I a tu Ire, gràcies per ser la meva confident, perquè juntes sumem en tot, en plors i sobretot en riures!

Gracias a vosotros tres, mis recuerdos huelen a cuentos por la noche, a Navidad, a la estufa del terreno los domingos, a crema de sol en las tardes de verano, a millones de disfraces, a "barbies" en caravanas, a largas horas de teléfono entre Barcelona y París. Huelen a vuestro apoyo incondicional. Gracias por darme esta hermosa vida!

Había una vez un hombre del que me enamoré profundamente. Él me cogió de la mano y desde entonces, paseamos juntos por un sendero, descubriéndonos entre risas, ayudándonos a sortear las piedras. Que nuestro camino no acabe nunca, Antonio.

# Contents

<b>1</b>	<b>Introduction</b>	<b>7</b>
1.1	Heme proteins . . . . .	8
1.2	Heme-based gas sensor proteins . . . . .	9
1.3	CooA . . . . .	14
1.4	DNR . . . . .	16
1.5	Optical spectroscopic techniques for monitoring heme protein structure	17
1.6	FRET observed by time-resolved fluorescence spectroscopy . . . . .	23
1.7	This work . . . . .	24
<b>2</b>	<b>Protein-Ligand binding</b>	<b>26</b>
2.1	Choice of fluorescence labels: ATTO-390 and Alexa-488 . . . . .	26
2.2	Fluorescence anisotropy measurements . . . . .	30
2.2.1	Theory of fluorescence anisotropy . . . . .	31
2.2.2	Values for anisotropy and excitation photoselection . . . . .	32
2.2.3	Results of fluorescence anisotropy measurements . . . . .	34
2.3	FRET observed by time-resolved fluorescence spectroscopy . . . . .	40
2.4	Circular dichroism measurements . . . . .	42
2.4.1	Results of CD measurements . . . . .	43
<b>3</b>	<b>Ultrafast ligand dynamics in CooA and DNR and comparison with other heme proteins</b>	<b>47</b>
3.1	CO-rebinding in CooA wildtype and mutant proteins . . . . .	48
3.2	Ligand-rebinding in DNR . . . . .	51

3.3	Temperature dependence study: activation barriers of ligand dynamics	55
3.3.1	Energy barriers in 6-c heme proteins: <i>CooA</i> and <i>DNR</i>	55
3.3.2	5-c heme sensor proteins: small temperature dependence for <i>DosT</i> and <i>Dos T Y169F</i>	62
3.3.3	Temperature dependence of CO-rebinding in cytochrome <i>c</i> variants	66
<b>4</b>	<b>Ligand dynamics in the heme-domain of the <i>EcYddV</i> sensor protein</b>	<b>73</b>
4.1	Quantum Yield determination of $O_2$ dissociation	76
4.2	Fe(II)-NO, Fe(III)-NO and Fe(II)-CO forms of <i>YddV</i>	78
<b>5</b>	<b>Conclusions and Perspectives</b>	<b>84</b>
<b>6</b>	<b>Materials and Methods</b>	<b>87</b>
6.1	Bacterial strains	87
6.2	Growth medium and antibiotics	87
6.3	Plasmids	88
6.3.1	<i>cooA</i> gene	88
6.3.2	<i>dnr</i> gene	89
6.3.3	<i>dosT</i> gene	90
6.3.4	Plasmid DNA purification	91
6.4	DNA Gel electrophoresis	92
6.5	Site-directed mutagenesis, <i>Dnp</i> I digestion and transformation	93
6.6	Protein expression and extraction	94
6.7	Purification of proteins	95
6.8	Protein gel electrophoresis (SDS-PAGE)	96
6.9	Steady-state absorption and protein concentration	96
6.10	Heme binding on <i>DNR</i>	99
6.11	Time-resolved visible absorption spectroscopy	100
6.12	Labelling of <i>CooA</i>	102
6.13	Anisotropy measurements	104
6.14	<i>YddV</i> Fe(II)- $O_2$ complex formation	105

6.15	Time-resolved fluorescence spectroscopy . . . . .	105
6.16	Circular dichroism . . . . .	108
6.16.1	Preparation of proteins for the CD measurements . . . . .	109

# Chapter 1

## Introduction

*The light of knowledge* is a particularly appropriate expression in the context of spectroscopy, since most of the currently known structures of atoms and molecules come from the study of the interaction of light with matter. Different ranges of the electromagnetic spectrum provide different kinds of information as a result of such interactions. For instance X-ray diffraction yields structural information on crystallized (macro)molecules, visible spectroscopy ( $\sim 400 - 800$  nm) on the electronic properties of coloured compounds and infrared spectroscopy gives detailed information on individual chemical bonds. Biological macromolecules can naturally contain, or be artificially labelled with, coloured entities that lend themselves to spectroscopic investigation of their static and dynamic properties using visible absorption and emission (fluorescence) techniques. Proteins can incorporate a variety of coloured cofactors, including chlorophyll, heme and flavin; these are often directly involved in functional reactions. In addition, external fluorophore markers can in principle be engineered at specific positions of the protein or used to label substrate molecules. Due to the extremely high time resolution possible with visible spectroscopic techniques, very fast dynamic processes involving the cofactors can be monitored. In heme proteins, the subject of this thesis, this can be achieved because photolysis of heme-bound ligands can start functional dynamics. In particular, this thesis project focuses on the functioning of a rapidly expanding class of proteins, the heme-based sensors, and aims to use (time-resolved) fluorescence and absorption spectroscopy to shine light on the dynamic interaction of these proteins with both, small gaseous sensing ligands and catalytic substrates.

## 1.1 Heme proteins

Heme proteins constitute an omnipresent class of proteins that are involved in a wide variety of biological functions. These include:

- Transfer and storage of oxygen. The mammalian proteins hemoglobin and myoglobin are well studied examples.
- Enzymatic catalysis. Heme often is part of the catalytic site, where it acts as binding site for the substrate. Reduction-oxidation reactions involving the heme cofactor are often part of the catalytic mechanism. Examples include nitric oxide synthase, cytochrome *c* oxidase and P450.
- Electron transfer. Many cytochromes, including cytochrome *c* in the mitochondrial respiratory chain [1] mediate single-electron transfer between distant complexes, either as separate soluble proteins or as part of larger complexes.
- Sensing of diatomic gas molecules. The mammalian NO receptor soluble guanylate cyclase (sGC) is the best-known example of a heme-based sensor protein. Bacterial proteins include the CO sensor CooA, the NO sensor DNR and the  $O_2$  sensors FixL, *Ec*Dos and HemAT [2, 3].

Bacterial heme-based sensor proteins play an important role in the adaptation to different environments, which is essential for the survival of the organisms [3]. More generally, bacteria have developed complex mechanisms in order to rapidly adapt to extreme and fluctuating environments. Among these fluctuating parameters are temperature, pH and the concentrations of diatomic gases.

It is obvious that a heme cofactor is essential for many bacterial functions [5]. The heme is a prosthetic group which contains an iron atom in the center of a heterocyclic ring, called porphyrin. The most common is the *b*-type heme (Fe-protoporphyrin IX, represented in Figure 1.1). Usually, the heme is embedded within the hydrophobic core of the protein and it is not accessible to the solvent [5] (we will see later on this work that this can be different for some proteins). The central iron atom is crucial for the functioning of heme proteins via its capacity to coordinate to diatomic molecules such as CO, NO or  $O_2$  and to change the oxidation state [6]. Moreover, the heme can, indirectly, act as a regulatory molecule which controls DNA transcription and protein stability [5]. At high concentrations, heme can also be toxic and therefore careful regulation is required.

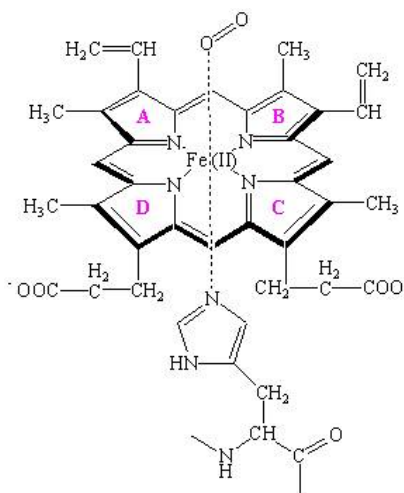


**Figure 1.1:** Scheme of (*b*-type) heme. The heme iron is shown hexacoordinate, with four bonds to nitrogens (N) of the porphyrin, which is a planar molecule. Perpendicular to this plane, usually a ("proximal") histidine is present (lower part in the Figure), which links the heme to the backbone of the protein. The sixth position, called distal position, can be unoccupied (5-coordinate heme), occupied by another backbone residue or occupied by an external diatomic molecule (as an example, in this figure, an  $O_2$  molecule is present, upper part). Figure taken from [4].

In this work we focus on heme-based gas sensor proteins. In the next section, the functioning and characteristics of this class of proteins is introduced.

## 1.2 Heme-based gas sensor proteins

Heme-based gas sensor proteins can essentially detect the physiological gaseous messenger molecules CO,  $O_2$  or NO [3]. The presence or absence of the effector gas triggers a conformational change by which the protein passes from the *off*-state (inactive) to an *on*-state (active), necessary for the functional activity of the gas sensor protein [3, 7, 2]. In isolated proteins, switching of a sensor may also be activated by other gases than the physiological effector, or by redox changes of the heme, but this does not necessarily occur in a natural environment. For example, oxidation of the heme iron in the CO sensor CooA inactivates the protein, but this does not mean that the CooA is a redox sensor, since no evidence exists that this happens *in vivo* [3]. Thus, in addition to the detection of the physiological effector, these sensor proteins have also evolved to be able to discriminate against other non-effector gases, which may be present in the environment. Heme based sensor proteins must alter an activity upon binding of the effector ligand and the switching mechanism generally involves a change of conformation in the protein backbone [3]. The switching mechanism is

initiated by a change in heme coordination (either 5-coordinate to 6-coordinate or exchange of ligands at the distal binding site in 6-coordinate heme-proteins), and propagates through the protein via conformational rearrangement of the protein towards a (distant) transmitter domain (*e.g.* a catalytic or DNA binding site) . In some cases, these events eventually lead to a large scale conformational change, including domain rearrangements.

Heme-based gas sensor proteins can be divided into different groups on the basis of the heme-binding domain motifs. We discern (i) heme-PAS, (ii) heme-GAF, (iii) analogues of CRP (cAMP Receptor Protein), (iv) globin-coupled sensor and (v) heme-NO-binding (HNOB) [1, 3]. The variations in the architecture of the binding domains add to the large diversity of roles played by these proteins [5]. Figure 1.2 shows the five different heme-binding motifs.

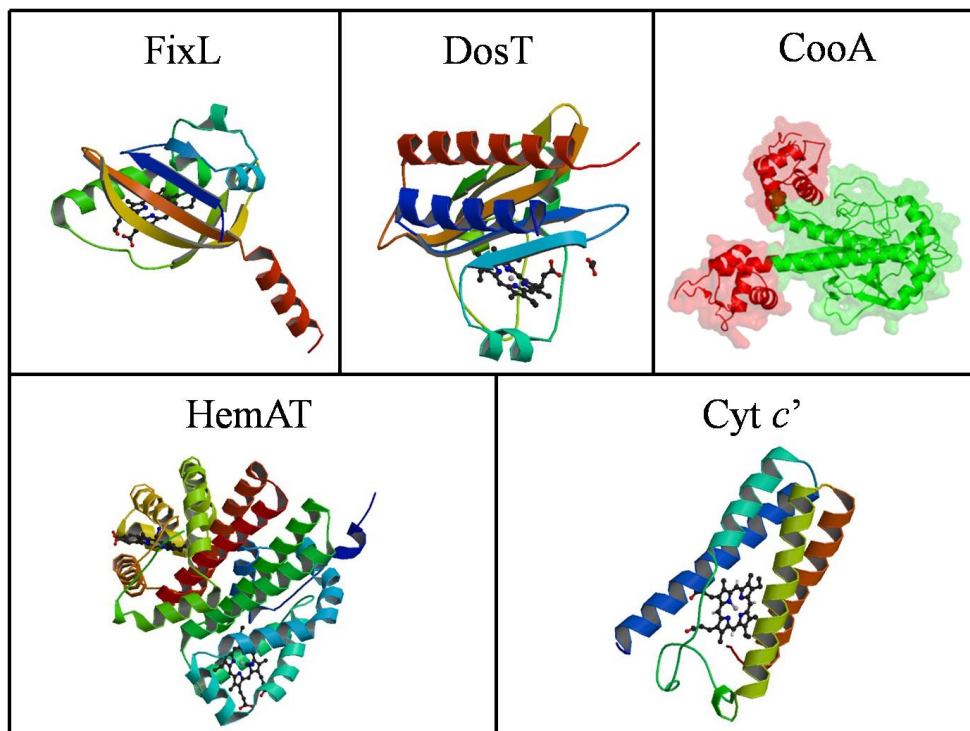


**Figure 1.2:** Examples of different classes of heme-binding motifs in heme-based sensor proteins: FixL (Heme-PAS) [8]; DosT (Heme-GAF) [9]; CooA (CRP analogous, in green heme-binding domain) [10]; HemAT (globin-coupled) [11]; cyt *c'* (HNOB) [12].

PAS domains are highly conserved structural folds, can contain a variety of cofactors (or no cofactor at all) and are found in many different sensor proteins, including light and voltage sensors. Heme-PAS containing sensors specifically sense gaseous molecules, and possibly redox changes, and are among the best studied PAS-domain proteins.

The PAS domain encompasses a region of  $\sim 270$  amino acids [6]. PAS (**P**er-**A**rn timer-**S**ignaling) is an acronym for the three proteins where the domain was first discovered [13]: **P**eriod circadian protein; **A**ryl hydrocarbon receptor nuclear translocator protein and **S**ingle minded protein.

The heme-PAS family has been relatively well-studied. The best-known example of this family is the rhizobial  $O_2$ -sensor kinase FixL. This protein is part of a two-component system (the other one being FixJ, which is the response regulator) which regulates the expression of genes involved in nitrogen fixation and denitrification [5, 14]. FixL contains three different regions: a hydrophobic region, which is not required for heme binding, but seems to prevent the heme from oxidation; the sensor PAS domain containing the heme cofactor, and the C-terminal histidine kinase domain [6] (see top part of Figure 1.3).

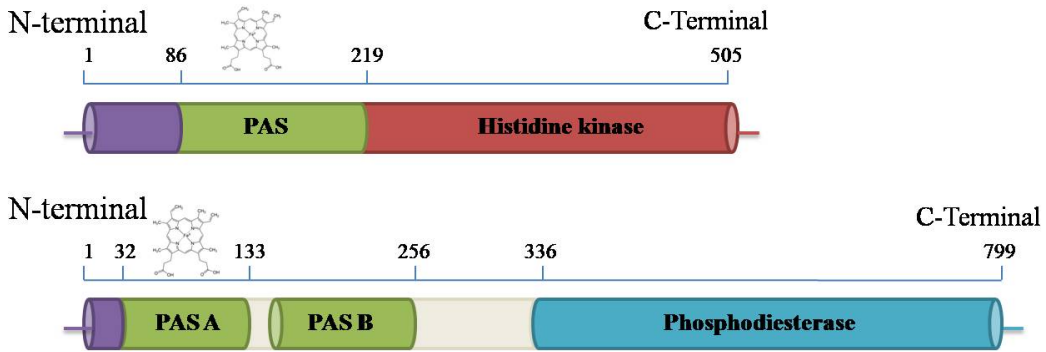


**Figure 1.3:** Schematic representation of the PAS domain-containing sensor proteins FixL and *EcDos*. **Top part:** Scheme of the three different domains in FixL. In purple, the hydrophobic domain. In green, the PAS domain, where the heme binds. In red, the histidine kinase domain. **Bottom part:** Scheme of the different domains in *EcDos*. In purple, the N-terminal. In green, the two PAS domains, PAS A and PAS B; PAS A has  $\sim 60\%$  homology to FixL-PAS and binds the heme cofactor. In blue, the C-terminal phosphodiesterase domain.

In FixL, the heme is 5-coordinate in the unliganded state and can bind  $O_2$  and also NO and CO (these two with higher affinities than  $O_2$  although they are not gas effectors for FixL; yet the CO affinity is much lower than for other heme proteins [15]). The  $O_2$  affinity is very small, in agreement with FixL's function of detecting changes between micro-aerobic and aerobic conditions associated with nitrogen fixation and oxidative respiration, respectively [16]. FixL heme domain crystal structures have been determined in different forms (ferric, ferric-cyadine, ferrous- $O_2$  and NO) [17, 18], which have helped elucidating its sensing mechanism, although it is not yet fully established and crystal structures of the full-length protein are not available.

The  $O_2$ -sensor Dos (Direct oxygen sensor) from the Gram-negative bacterium

*Escherichia coli* is another heme-PAS protein, initially described by Delgado-Nixon *et al.* in [19]. This protein reacts to variations in the concentration of  $O_2$  and helps to allow *E. coli* to survive in both aerobic and micro-aerobic environments. The heme-binding region in *EcDos* is  $\sim 60\%$  homologous (and  $\sim 25\%$  identical) to the  $O_2$ -sensing PAS domain of FixL. *EcDos* contains two different PAS domains, the heme only binding to the first PAS (PAS A) domain [6]. Other than FixL, here the heme is 6-coordinate in the reduced unliganded state (His-Met Fe coordination). Another difference is at the catalytic level: while in FixL, the PAS domain is associated with a C-terminal histidine kinase domain, the *EcDos* PAS domain is associated with a C-terminal phosphodiesterase (see bottom part of Figure 1.3). Although *EcDos* has been proposed to act as direct oxygen sensor because of the similarity with the heme domain of FixL, it could also act as a redox sensor, since it has been observed that in the ferric form of the heme, a  $H_2O$  molecule binds, and the activity of the protein strongly decreases upon oxidation [20]. We note that *EcDos* is functionally coupled to the YddV sensor (see below), which produces cyclic dGMP, the substrate of *EcDos* [21].

Particularly interesting are the recently discovered heme-based sensors DosS and DosT from the pathogen *Mycobacterium tuberculosis* [2]. DosT and DosS are two histidine kinases capable of diatomic ligand binding. They activate the transcriptional regulator protein DosR, which plays an important role in the regulation of the transition from the replicating form of the organism to a persistent latent state that is unresponsive to antibiotics [5]. The transition between the two states is activated by stimuli including hypoxia (DosT) [22] and exposure to NO (DosS) [23]. DosS and DosT both contain two GAF domains (named like this after proteins where this domain was first observed: cGMP-specific phosphodiesterases, Adenylyl cyclases and FhlA) A and B, which are similar in topology to PAS domains [24]. The heme can only bind to the GAF A domain, while the GAF B structure exhibits alterations that suggest that this domain may help GAF A to sample the convenient structure required for heme binding [24]. In the ferrous state of the heme, these proteins are able to bind external ligands such as  $O_2$ , CO or NO, and they are 5-coordinate in the absence of these ligands [23].

CooA is the best-studied example of the class of heme-based sensor proteins that is related to the cAMP-receptor family. CooA from the photosynthetic purple bacterium *Rhodospirillum rubrum* is a transcription factor that governs the oxidation of CO to  $CO_2$  [25] and has 30% sequence identity with *E. coli* CRP [26]. Figure 1.4 represents the two different domains in this protein, where the sensor domain contains the

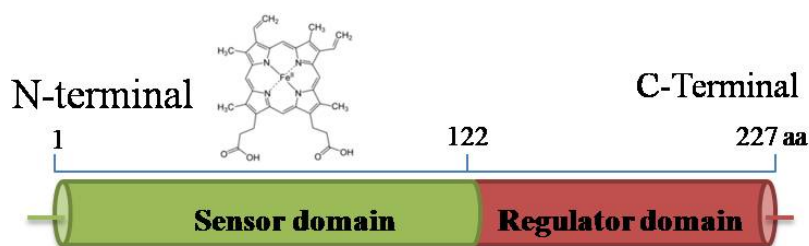


**Figure 1.4:** Schematic representation of the transcription factor and CO-sensor protein CooA. CooA has two different domains: an N-terminal sensor domain (in green) and a C-terminal regulator domain (in red). The N-terminal, in the sensor domain, can coordinate the heme cofactor.

N-terminal and the heme, where the CO binds. CooA is the only heme-based sensor protein from which a complete crystal structure has been determined (in the inactive form). A more detailed introduction to the function of this protein is given in the next section.

The globin fold is found in many heme proteins, in particular in the prototypical mammalian heme proteins myoglobin and hemoglobin, responsible for oxygen storage and transport, respectively. Only relatively recently, with the discovery of HemAT, globins were also identified as part of heme-based sensor proteins. HemATs from *Halobacterium salinarium* and *Bacillus subtilis* were first discovered by Alam *et al.* in 2000 [27]. In recent studies, this family of sensors has expanded to at least 30 members [3]. Here, a conserved globin-like heme-binding domain is always present and coupled to a great variety of enzymes which are predicted to play an important role in the regulation of second messengers and other still unknown functions. In the context of this thesis, an important member is the oxygen sensor diguanylate cyclase YddV from *E. coli* [21, 28], which acts in tandem with *EcDos* (see chapter 4).

Finally, in the HNOB group, we can find the soluble guanylate cyclase (sGC), which is an important NO-receptor involved in NO signaling in a number of mammalian tissues [16, 29]. This protein is a heterodimer. Each subunit contains similar N-terminal domains, only one of which binds the heme, a middle domain which contains the dimerization helices and the C-terminal domain which contains the catalytic region. The catalytic domain triggers the formation of the second messenger cyclic guanosine monophosphate (cGMP) from guanosine triphosphate upon binding of NO to the heme [16, 24]. No crystal structure for sGC has been reported yet. However the protein is thought to share properties with bacterial cytochrome *c'* (Fig. 1.2), in particular the NO binding mode, which occurs by replacing the proximal histidine in cytochrome *c'*.

Essentially, all these proteins act as bistable switches. For many proteins, the activity has been characterized in the *on* and *off* states, and sometimes structural information about these end states does exist, but determining the intraprotein switching mechanism and pathway remains a challenge.

Whereas the work in this thesis also aims at establishing general mechanisms for heme-based proteins and the classes of proteins presented in this section are used for reference, the main focus of this work are the two transcription factors and heme-sensors CooA from *R. rubrum* and DNR from *Pseudomonas aeruginosa*. The next two sections concern specifically these two proteins.

### 1.3 CooA

CooA can be considered a prototypical gas sensor transcription factor. It was the first protein where the binding of CO to heme was established to play a clear biological role [30]. CooA regulates the expression of genes responsible for CO oxidation; allowing the protein to use CO as the unique metabolic electron acceptor in the absence of oxygen. The structure of the inactive Fe(II) CooA has been determined [10] (see right part in Figure 1.5). The protein is homodimeric, each monomer containing two different domains: the N-terminal heme-containing sensing domain, where the effector molecule can bind, and the C-terminal DNA binding domain. The heme group is placed close to the interface of the dimers and connected to the protein via axial bonding to two protein residues: in the Fe(II) state a proximal histidine (His77, exchange to Cys75 in the oxidized form [31, 32]) and the N-terminal proline (Pro2), belonging to the opposite subunit of the dimer. Thus, in the inactive form, CooA has a 6-coordinate heme (see Figure 1.7). One unique feature of this protein is the heme coordination to the N terminus.

The crystal structure for the active Fe(II)-CO CooA form has not yet been determined, but it has been modeled by analogy to the homologous protein CRP [30]. The model for the CO activated form of CooA suggests that binding of CO to the sensing domain results in a delocalized motion within the protein by which the DNA binding domain reorients considerably with respect to the sensing domain, thus allowing for DNA to bind. CO displaces the N-terminal proline as a heme ligand; the N-terminal loop is then thought to reposition at the interface between the sensing domain and the DNA binding domain, stabilizing the protein in its active form [33]. In Figure 1.6 the assumed mechanism for CO activation in CooA is sketched.

Dynamics during the initial stages of the switching mechanisms can in principle be

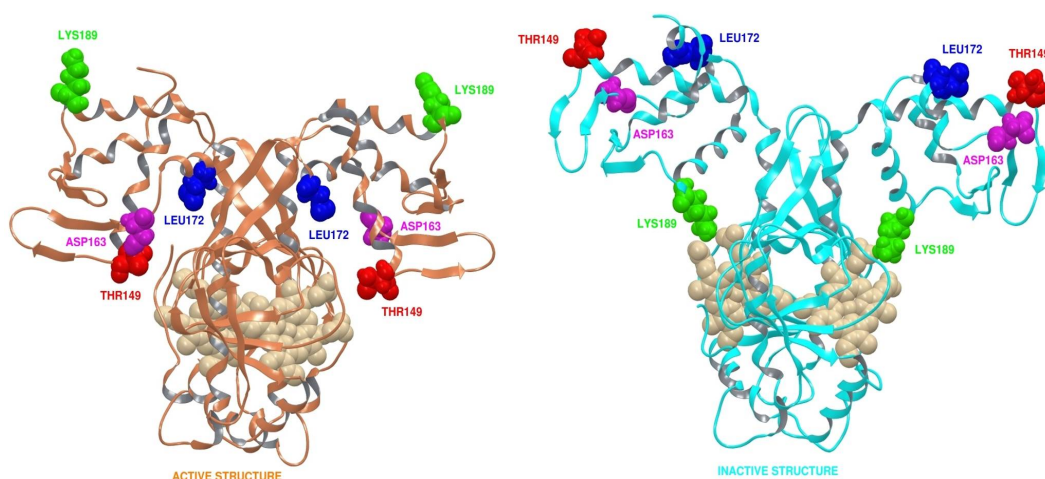


**Figure 1.5:** **Left part:** Model of active (CO bound) structure of CooA, based on homology with CRP. **Right part:** Inactive structure of CooA.

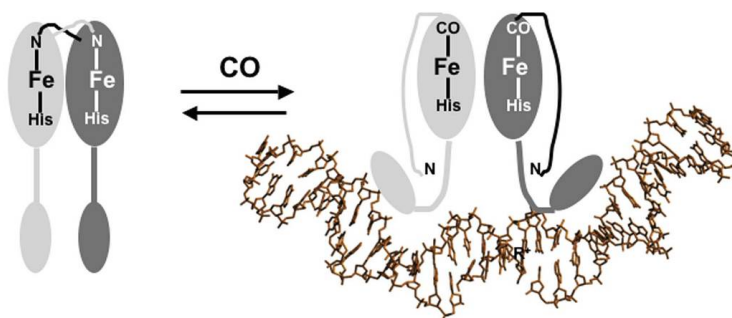


**Figure 1.6:** Cartoons for the active and proposed inactive structures of CooA. In the *off*-state of CooA (**left side**), the N-terminals are both attached to the heme of the opposing subunits. In the *on*-state (**right side**), CO binds at the position of the N-terminal, which moves away from the sensing domain, interacting with the loop connecting the heme-binding and the DNA-binding domains. This rearrangement stabilizes the protein in a configuration favoring DNA binding. Figure taken from [33].

studied using time-resolved spectroscopy, exploiting the property that in the ferrous form of the heme, the ligand at the 6<sup>th</sup> position can be photodissociated by using ultrashort light pulses. As in many other heme proteins, recombination of an internal amino acid ligand to CooA takes place in a monoexponential way and is very fast ( $\sim 6$  ps) [34, 35], possibly indicating that the sensed ligand CO is required in the heme pocket to displace the proline, as suggested also for ligand exchange in other 6-coordinate sensor proteins [36]. CO dissociation leads to remarkably efficient ( $> 90\%$ ) CO recombination in a multiphasic way on the hundreds of picoseconds timescale [34] and a very low escape (and thus ultimately switching) yield. This fast geminate (see below) CO binding is far more extensive than in most heme proteins, implying

that CooA acts as an efficient CO trap. This feature of low escape for the physiological ligand is presumably a common property for heme-based sensor proteins [2]. For CooA, CO rebinding may be a sensitive probe of the heme environment.

The timescale and pathway of the global conformational change required for switching between the active and inactive forms are essentially unknown.

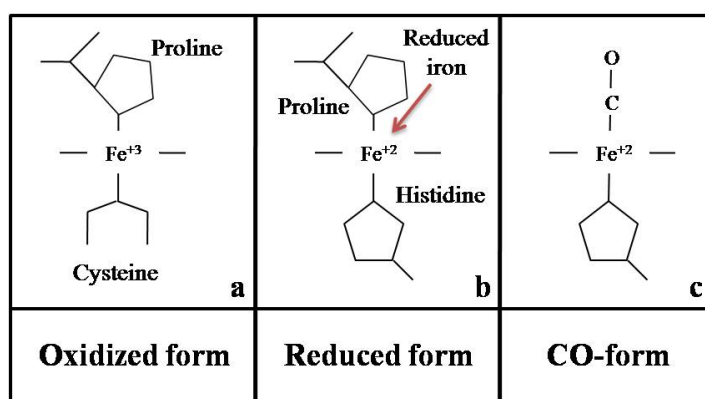


**Figure 1.7:** Heme coordination for CooA in the: **a)**oxidized form; **b)**reduced form; **c)**CO-form (active form).

## 1.4 DNR

Dissimilative Nitrate Respiration Regulator (DNR) is a recently discovered protein from *P. aeruginosa*, a bacterium responsible for nosocomial infections and capable of anaerobic respiration due to a process called denitrification which supplies energy by reduction of nitrate ( $\text{NO}_3^-$ ) to molecular nitrogen ( $\text{N}_2$ ). As CooA, DNR is a homodimeric heme-based gas sensing transcription factor homologous to the CRP superfamily. Its physiological trigger is thought to be NO, a compound in the denitrification pathway that is cytotoxic at high concentrations and also released by the host defense system. Binding of NO promotes transcription of genes involved in the denitrification pathway [37, 38, 39].

DNR is purified in the apo-form, without a heme cofactor. It is able to bind hemin ( $\text{Fe}^{+3}$  protophorphyrin IX) *in vitro* with a high affinity. However, the crystal structure has only been solved for the inactive apoprotein, showing structural similarities to that of CooA and other transcription factors from the CRP superfamily. An, *a priori*, unexpected feature in the DNR structure is the position of the sensing domain, which is  $55^\circ$  rotated with respect to the same domain in CRP and  $60^\circ$  rotated with respect to the inactive structure of CooA (see Figure 1.8). This unusual inactive conformation of

DNR, if it would be maintained in the heme-bound form, and assuming that the active conformation is similar to that in CRP, would suggest that this protein undergoes a very large conformational change, much bigger than in other sensor transcription factors, to be able to bind DNA [38]. The heme coordination ligands are not well established yet, but mutagenesis experiments suggest that the heme pocket is located more to the interior of the sensing domain than in *CooA* and that histidines are involved as coordinating ligands [39] (see Figure 1.9).

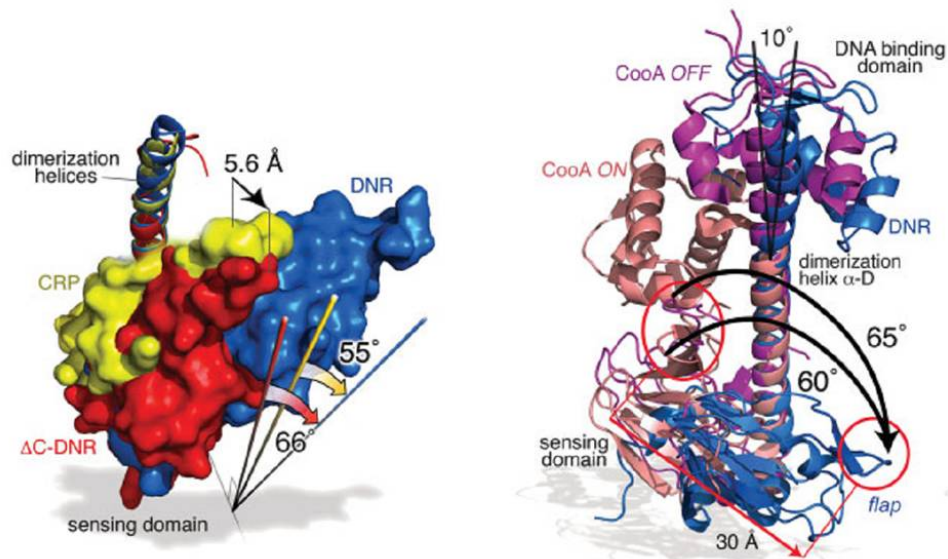


**Figure 1.8:** **Left part:** Comparison of the sensing domains for inactive DNR WT (blue),  $\Delta$ C-DNR (C-terminal deletion mutant) (red) and CRP (yellow). **Right part:** Comparison of the sensing and binding domains for DNR WT (blue), *CooA* off-state (pink) and *CooA* on-state (salmon). The structures are aligned on the dimerization helices, which connect the sensing and DNA-binding domains. Figure adapted from [38].

For its interest in microbial regulation processes and to get insight into its role as an NO sensor, studying dynamic processes in DNR is of great interest.

## 1.5 Optical spectroscopic techniques for monitoring heme protein structure

A large variety of spectroscopic techniques is used to study heme proteins. Many of them exploit the fact that they are metalloproteins. For instance, detailed studies of the heme coordination are possible with spin-sensitive magnetic techniques, in particular electron paramagnetic resonance (EPR) and magnetic circular dichroism (MCD). The visible absorption spectrum of the heme is a marker for heme redox and coordination

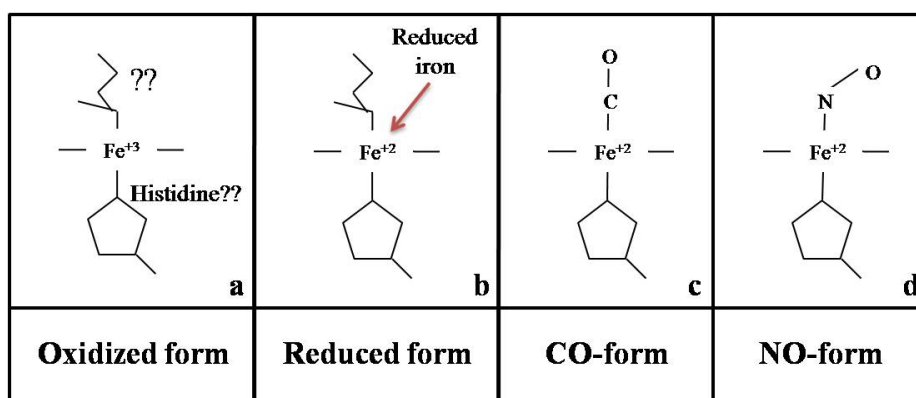


**Figure 1.9:** Heme coordination for DNR in: **a)** oxidized form. Notice that internal ligands have not been definitely determined yet. **b)** reduced form; **c)** CO-form (non-active form); **d)** NO-form (non-active).

states. Resonance Raman spectroscopy also exploits the electronic transitions of the heme and can yield detailed structural information on the heme configuration and the direct interaction with the protein environment. Infrared spectroscopy (in steady-state in particular Fourier Transform Infrared (FTIR)) is another vibrational technique that in principle gives detailed information on the chemical bonds of the entire protein-cofactor-ligand structure. Here, specifically differential approaches, monitoring effects of redox and ligation changes, or isotope substitutions, are sensitive markers of changes in the protein bonding, including hydrogen bonding and salt bridges.

Electronic absorption monitors the transition from the ground state to the excited state by photon absorption. The reverse transition can be accompanied by photon emission, *i.e.*, fluorescence. However, Fe-porphyrins have a very short-lived excited state and are virtually non-fluorescent. Therefore native heme proteins are not studied by fluorescence spectroscopy. However, fluorescence spectroscopy of engineered systems is possible. For instance Zn-porphyrins are highly fluorescent [40]. Also, extrinsic fluorescent labels can be attached to the protein or to substrates, and interaction between these fluorophores and the protein entity, including the heme, can be used to monitor protein properties. For instance, the extent of fluorescence quenching by heme has been used as a marker of the heme redox state in highly dilute solutions [41].

Liganded heme proteins possess a property that makes them highly suitable for time-resolved studies: the heme-ligand bond can be photodissociated with high quantum yield [16]. This property, although presumably not physiologically relevant as bond breaking is thought to occur via thermal activation, allows synchronisation of the dissociation in a macroscopic sample and therewith spectroscopic monitoring of the

time evolution of the heme-ligand-protein interaction. Photodissociation techniques are extensively used over a large range of time scales. Using very short light pulses, time resolution down to the femtosecond regime can be achieved [42].

In our work, we focus on the use of ultrafast time-resolved absorption spectroscopy and on fluorescence techniques. In the following subsections, the background of these approaches, in the context of our applications, will be shortly described.

### **Visible transient absorption spectroscopy**

As mentioned above, ultrafast spectroscopy of ligand dynamics in heme proteins is based upon the photoinduced cleavage of the heme iron-ligand bond with high quantum yield. For the best studied heme protein, myoglobin, this quantum yield is  $\sim 1$  for CO,  $\sim 0.5$  for NO, and  $\sim 0.3$  for  $O_2$  [16, 43], as determined after a few picoseconds. In addition, for cytochrome *c* it has been demonstrated that an internal residue (methionine) can be photodissociated with high quantum yield [44, 45] and this is presumably also the case for other 6-coordinate heme proteins [35]. The sub-unity quantum yields for  $O_2$  may be due to very fast recombination processes and have been found to be highly variable in different heme proteins [46]. Therefore, this property may be used as a probe of the heme-protein interaction.

Femtosecond lasers have been available for over 30 year, and have allowed for the development of a range of ultrafast spectroscopy techniques. Visible transient absorption measurements have been largely exploited for the study of heme proteins, since they provide valuable information about the ligand dynamics in the heme vicinity and indirectly about their structural properties. In particular, in such experiments, the rebinding of the dissociated ligand provides information about the intrinsic reactivity of the site for ligand binding to the heme iron and protein control over the ligand pathway. Generally, in these experiments, the absorbance spectrum of the sample is measured, using a short, weak and spectrally large probe pulse, as a function of time after excitation by a strong pump pulse tuned to match the absorption of the sample. Typically both pulses have durations in the range of  $\sim 100$  fs or shorter, and the delay between them is controlled by mechanical variation of the optical path lengths of the beams. The setup used in our experiments is described in section 6.11.

Several processes can contribute to the spectral evolution after heme excitation. First, the energy of the absorbed photon, even if chosen in the lowest energy transition ( $\alpha$  bands of the heme,  $\sim 550$  nm), is not fully used for breaking of the heme-ligand bond [42]. Therefore, higher electronic and vibrational states are populated directly

after excitation and bond breaking. These states typically dissipate within a few picoseconds [16]. They are relatively important for 5-coordinate unliganded heme and for dissociation of  $O_2$ , and weak upon dissociation of CO and NO, which are mostly studied in this work.

Subsequently, transient spectra corresponding to ligand dissociation are observed. For the heme Soret region, this corresponds to a red shift of the absorption band. Initially, the dissociated ligand is located in the heme pocket. It can then rebind to the heme, as monitored by overall decay of the transient spectrum, or migrate away from the heme through intra-protein migration routes, eventually leading to escape from the protein or rebinding from a position further away. The binding of a heme-ligand pair that involves the same ligand that has been dissociated is termed "geminate" recombination (see Figure 1.10, green trajectory). This is a unimolecular process, independent of the concentration of the ligand in the solvent, as opposed to bimolecular rebinding (out of the scope of this work), the rate of which is proportional to the ligand concentration. Geminate recombination typically occurs on the picosecond-nanosecond timescale [47] and competes with ligand escape to the solvent (Fig. 1.10, blue trajectory). It is often multiexponential, reflecting recombination from multiple configurations. NO is very reactive with heme and NO recombination dynamics almost invariably include fast phases on the time scale of 5-10 ps [16]. In many heme proteins, and in particular in myoglobin and hemoglobin, CO geminate recombination does not occur to a substantial extent. However, it plays an important role in the CO sensor CoxA.

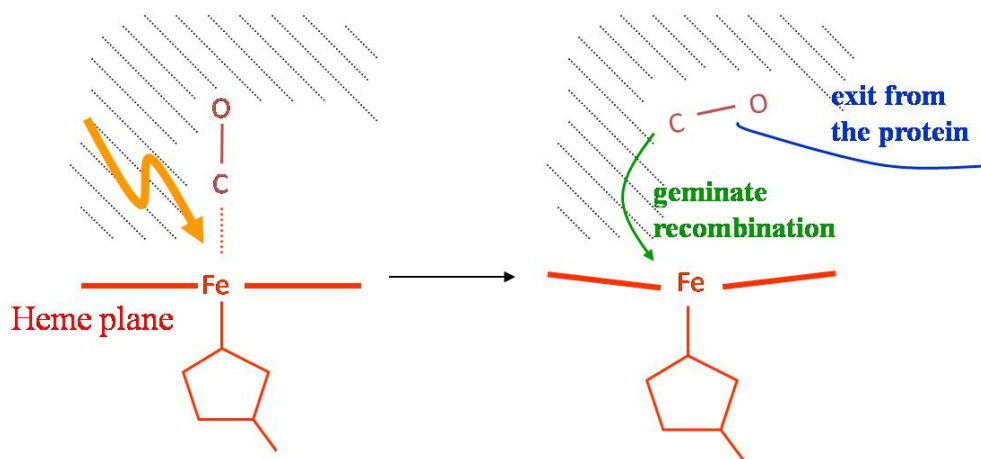


**Figure 1.10:** Schematic representation of the photodissociation (**left part**) and recombination/escape (**right part**) of gas molecule in heme-based proteins. Geminate heme-ligand recombination is represented in green and ligand escape in blue. Example of a CO-complex.

Finally, directly or indirectly, light-induced heme redox changes may occur [48, 49]. These do not play a significant role in the present work.

## Fluorescence spectroscopy

In biological sciences, the use of fluorescence has strongly developed over the last decennia, becoming a dominant methodology used in many standard applications such as flow cytometry, DNA sequencing or genetic analysis [50]. Improvements in the fluorescence detection and in the labeling of cells and molecules currently allow for the use of a large range of dedicated fluorescence applications in fundamental research.

Fluorescence is the result of a three-stage process occurring between the electronic states of a fluorophore, as illustrated in Figure 1.11 for an electronic two-level system. Absorption of a photon (blue) with energy matching the electronic transition places the molecule into a higher electronic state [51]. Within the excited state, the molecule relaxes to lower vibrational levels through non-radiative transitions (green lines). The system can return to the ground state through emission of a photon (fluorescence, red), a process occurring in competition with non-radiative intramolecular decay (green) and quenching due to interactions with the environment (purple). Due to the vibrational relaxation processes in excited and ground states, the emitted photons have a lower energy than the absorbing photons, as reflected by the Stokes shifted emission spectrum.

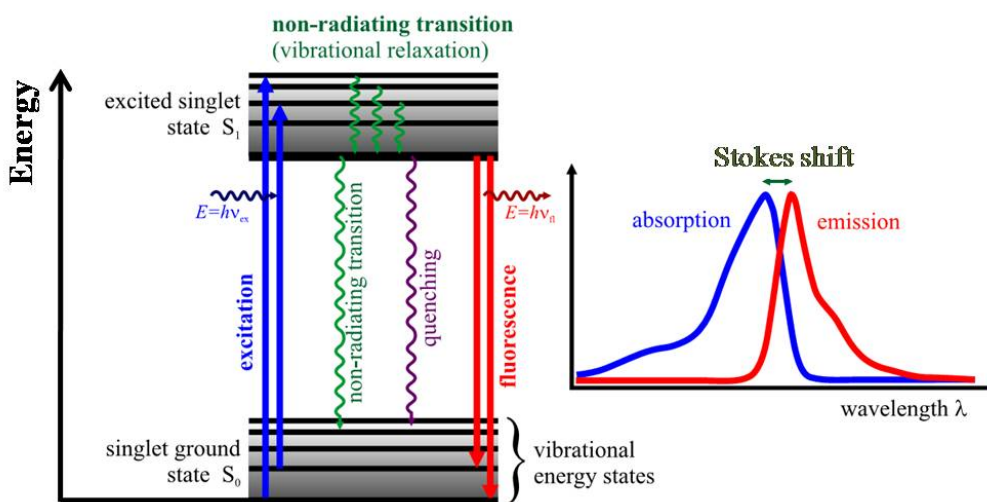


**Figure 1.11:** Jablonski diagram (left) and spectra (right), illustrating the process of creation and decay of an excited state. Picture adapted from [52].

Intrinsic decay by fluorescence generally occurs on the order of 1 to 10 ns. Com-

peting excited state deactivation processes can take place on the same timescale. These processes reduce the yield of fluorescence and diminish the effective decay time. Time-resolved fluorescence spectroscopy can provide direct information about such processes, which reflect properties of the environment of the fluorophore. Therefore, such techniques have been largely used for the study of the dynamics of molecules in biochemistry, biophysics and chemical physics on the picosecond-femtosecond timescale [53, 54]. They have been demonstrated to be particularly useful in the determination of protein interactions [55], inter- and intra-molecular distances, structural ordering or molecular mobility [56].

Relaxation processes in the excited states can occur over a range of timescales during fluorescence decay and such processes give rise to spectral shifts. In addition, fluorescence spectra are sensitive to the environment. For these reasons, spectral resolution is useful in studying time-resolved fluorescence, especially with potentially heterogeneous processes.

Several experimental methods are available for measuring time-resolved emission. They differ in temporal resolution, spectral resolution and sensitivity. Time-correlated single-photon counting (TCSPC), based on high-speed and highly sensitive detectors, is a widely used, commercially available, technique with a high sensitivity and dynamic range [50]. However, its instrument response is no less than tens of picoseconds, and the method is not spectrally resolved. Streak cameras, based on fast deflection of electron beams, combine high sensitivity with spectral resolution, but have a limited time dynamic range and resolution (mostly  $\sim 10$  picoseconds [57]).

Basically, two techniques exist based on gating by the pump-probe principle, with time resolution obtained by control of mechanical delay of the optical pathlengths. The most common is fluorescence upconversion, with a time resolution of less than  $\sim 200$  fs [55]. This technique is based on the mixing of the fluorescence with an ultrashort laser pulse in a non-linear crystal and detection of the sum-frequency signal [58]. In general, this method is also a single-wavelength technique. Broadband upconversion techniques also have been developed [59, 60, 61], which require a relatively complex alignment scheme. The other gating technique, used in this work, makes use of a Kerr cell, which combines high temporal and spectral resolution. Here the fluorescence is directly gated in a transparent Kerr medium placed between two crossed polarizers; it can subsequently be spectrally resolved. Using an ultrafast Kerr medium, the time resolution is essentially determined by the pulse duration ( $\sim 100$  fs) [54, 62]. The sensitivity of this method can be limited by background fluorescence when the fluorescence lifetime is very long with respect to the gate pulse duration; yet this can

be diminished by adapting the Kerr medium to the desired time resolution [62].

## 1.6 FRET observed by time-resolved fluorescence spectroscopy

Fluorescence Resonance Energy Transfer (FRET) is a technique where fluorophore-labeled (bio)macromolecules are involved in distance- and orientation-sensitive quenching processes. It has many applications including analysis of protein-protein interactions, conformational changes in proteins, and protein-ligand binding processes [63].

FRET is an electrodynamic process strongly dependent on the distance by which the excitation energy of one molecule (the donor, D) can be transferred to another (acceptor, A) by dipole-dipole coupling, hence without intermediate photon emission [64] (see Figure 1.12). In its simplest form, the rate of energy transfer from the donor to the acceptor,  $k_T(r)$ , is given by [50]:

$$k_T(r) = \frac{1}{\tau_D} \left( \frac{R_0}{r} \right)^6, \quad (1.1)$$

where  $\tau_D$  is the donor lifetime in absence of the acceptor,  $R_0$  is the Förster distance (where the rate of energy transfer equals that of the intrinsic donor decay) and  $r$  is the donor-to-acceptor distance. For FRET to occur, the absorption spectrum of the acceptor molecule must overlap with the emission spectrum of the donor [64] (see chapter 2). Following energy transfer,  $D$  is left in the electronic ground state and  $A$  in an electronic excited state.  $A$  may then act as a fluorescence emitter or as a quencher. The latter is the case when heme is an acceptor.

As equation 1.1 shows, the rate of energy transfer is strongly dependent on the distance between D and A, proportional to  $(1/r)^6$ . Thus the overall FRET efficiency is very sensitive over a limited distance range, usually within 20-90 Å, a size range well adapted to the typical size of biological macromolecules [50]. FRET can be used as a marker for proximity: if a donor-labeled molecule interacts with an acceptor-labeled molecule, FRET occurs and the donor is quenched; if it is free, the donor fluoresces. This on-off type of application is often used in single molecule studies. Quantitative information can be obtained either by measuring the amount of energy transfer upon changes in the interaction with an acceptor molecule by steady-state fluorescence techniques, or more directly by time-resolving the fluorescence of donor and/or acceptor. Here, initially one of the aims was to study intra-protein FRET

to characterize conformational changes between the active and the inactive states of CooA in macroscopic solutions, using steady-state and time-resolved fluorescence spectroscopy. After technical challenges with protein labeling, we first set out to quantify the protein-DNA distance.

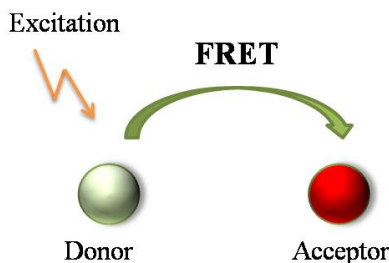


**Figure 1.12:** Simplified scheme of the energy transfer between the excited donor molecule (in green) and the ground-state acceptor (in red). After transfer, the donor is left in the ground-state and the acceptor is in the excited state, from where fluorescence or quenching occurs.

## 1.7 This work

The main focus of this work concerns dynamical aspects of the heme-based gas sensor transcription factors CooA and the recently discovered DNR. Structural and modeling studies have indicated that these sensors undergo a large global configurational change when they are activated by the binding of their corresponding physiological effector gas. Whereas the dynamic properties of heme-ligand interaction can be studied using well-established visible transient absorption spectroscopy, the delocalized conformational changes allowing DNA binding require spectroscopic observables sensitive to long-distance interactions. Fluorescence techniques in principle constitute a suitable approach. Altogether, work will be presented where, in combination with steady-state techniques, both ultrafast absorption and fluorescence are used to establish the interaction of these sensors, both with their gaseous effector ligands and with their DNA substrates. Comparative studies on related systems are performed to establish general mechanistic principles.

Chapter 2 focuses on the protein DNA ligand interaction. Labeling issues of protein and DNA with the ultimate aim of monitoring FRET with the heme as an acceptor are discussed. Fluorescence anisotropy is exploited as a probe for the DNA-protein binding and its sensitivity to the effector ligand. The direct observation of energy transfer from labeled DNA to heme in the CooA-CO-DNA complex using time resolved

fluorescence spectroscopy is reported, opening perspectives to map out dynamics of complex formation.

Chapter 3 deals with the characterization of ultrafast ligand dynamics in CooA and DNR by transient absorption spectroscopy. The effects of site-specific replacement of the heme-coordinating residue in CooA are investigated and importantly, the dynamics of the ligand recombination to DNR are studied for the first time. DNR is found to be a particularly suitable system to study the thermodynamics of CO migration and comparison with other protein systems are used in an attempt to determine general (activation) mechanisms.

Chapter 4 regards a ligand dynamics study performed on the newly-discovered oxygen sensor YddV, with an emphasis on clarifying the dynamic role of a distal tyrosine residue.

In the conclusions we summarize the most relevant findings and offer perspectives for future studies. Finally, the Materials and Methods section contains detailed information on the biochemical and molecular biology protocols and procedures, as well as descriptions of the optical experimental setups.

## Chapter 2

# Protein-Ligand binding

Protein-DNA interactions play a central role in transcription regulation. In *CooA* and *DNR*, the binding properties of specific protein-DNA complexes have been investigated [65, 37] and affinities to promoter sequences in the nanomolar range have been determined. However, to date structural information on the DNA-binding active forms of *CooA* and *DNR* is missing. For *CooA*, only a crystal structure of the non-active, reduced form has been obtained. For *DNR*, three-dimensional information exists only on the apo-protein. Therefore, the relative positions of these proteins with respect to the DNA target are not known. In addition, no information exists on the dynamics of protein-DNA complex formation and the general conformational changes occurring in the protein's backbone after binding to DNA.

In this chapter, we describe our efforts to obtain insight into aspects of protein-DNA binding. We have performed steady state fluorescence anisotropy and quenching measurements, transient fluorescence spectroscopy and circular dichroism spectroscopy. In particular, the fluorescence anisotropy and quenching measurements using fluorescence labeled DNA allowed us to determine interactions between DNA and protein-bound chromophores and to estimate their distance. This chapter starts with the description of the choice of the fluorescent labels.

### 2.1 Choice of fluorescence labels: ATTO-390 and Alexa-488

In order to visualize FRET with steady state and transient Fluorescence Quenching measurements, the target DNA was labeled with ATTO-390 (ATTO-TEC GmbH, see section 6.13). ATTO-390 ( $\lambda_{abs} = 390$ ;  $\lambda_{flu} = 479$  nm) is an uncharged coumarin

derivative, specifically intended for the labeling of DNA and proteins due to its high fluorescence quantum yield of 0.9. Its use is convenient since its relatively small size [66] in principle minimizes perturbation of the properties of the DNA to be labeled.

For the Fluorescence Anisotropy measurements, as an alternative to labeling with ATTO-390, we labeled the presumed DNA target sequence for DNR with Alexa-488 (see section 2.2.3), a popular highly photostable fluorescent dye that is larger than ATTO-390, with excitation and emission in the visible and a very high quantum yield (0.92) [67]. Figure 2.1 shows the molecular structures of both fluorescent labels.

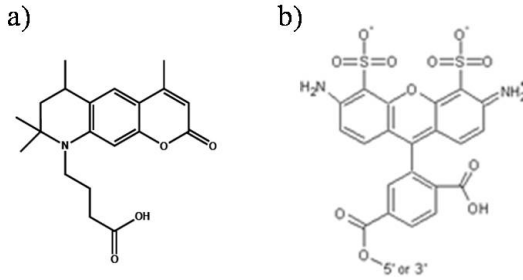


**Figure 2.1:** Molecular structures of: **a)** ATTO-390 (Figure from [66]) and **b)** Alexa-488 (Figure from [67]).

In our system, the fluorescent dye acts as FRET donor and the (itself non-fluorescent) heme as FRET acceptor. A main reason for the choice of ATTO-390 is the overlap between the donor emission and the acceptor absorption. Figure 2.2 shows the absorption and emission spectra of ATTO-390, the heme absorption (in the CO-bound form) and the spectral overlap.

The overlap integral,  $J(\lambda)$ , can be expressed in the following way [50]:

$$J(\lambda) = \frac{\int_0^\infty F_D(\lambda)\epsilon_A(\lambda)\lambda^4 d\lambda}{\int_0^\infty F_D(\lambda) d\lambda}, \quad (2.1)$$

where  $F_D(\lambda)$  is the fluorescence spectrum of the donor and  $\epsilon_A(\lambda)$  is the extinction coefficient (in  $M^{-1}cm^{-1}$ ) of the acceptor.  $J$  is expressed in units of  $M^{-1}cm^{-1}nm^4$ . Via numerical integration, in our system, the  $J$  value is calculated at  $\sim 9 \times 10^4 M^{-1}cm^{-1}nm^4$ .

The Förster distance,  $R_0$ , is defined as the distance between the donor and the acceptor where 50% of the excited molecules of the donor decay by energy transfer and the other 50% decay via their intrinsic decay path [53].  $R_0$  (in  $\text{Å}$ ) can be calculated as [50]:

$$R_0 = 0.211(\kappa^2 n^{-4} Q_D J(\lambda))^{1/6}, \quad (2.2)$$

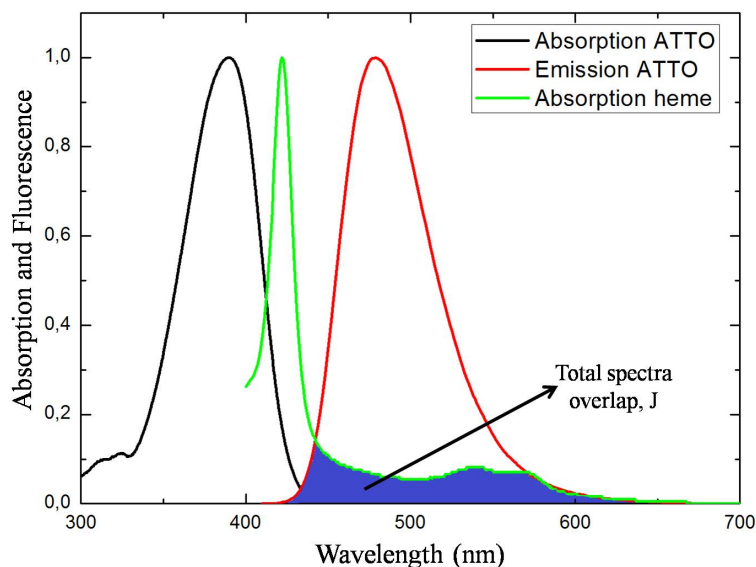


**Figure 2.2:** Normalized absorption (black) and emission (red) spectra of ATTO-390; normalized absorption of the heme (green). The overlap between ATTO-390 and the heme is indicated as a blue surface.

where  $\kappa^2$  is the factor describing the average relative orientation in space of the transition dipoles of the donor and the acceptor. We assume it to be  $2/3$ , the value corresponding to random orientation.  $n$  is the refractive index of the medium. We assume the water refractive index,  $n=1.34$ , since the sample is in an aqueous solution.  $Q_D$  is the quantum yield of the donor fluorophore in absence of the acceptor, 0.9 for ATTO-390 [66]. The value for  $R_0$  is then calculated at  $\sim 50 \text{ \AA}$ . For reasons of comparison, we point out that  $R_0$  has been determined for a variety of donor-acceptor systems, obtaining values which range predominantly from  $\sim 30$  to  $\sim 70 \text{ \AA}$  (the largest  $R_0$  reported is  $90 \text{ \AA}$  for the pair Europium-APC [50]).

Another reason for choosing ATTO-390 is its compatibility with the excitation conditions in the transient fluorescence set-up described in section 6.15. As shown in Figure 2.2, the ATTO-390 absorption is close to maximal at 400 nm, allowing efficient excitation of the sample (see Figure 6.13).

Finally, we point out that the largest source of error in calculating distances via FRET is the incomplete labeling of the molecules with the acceptor [50], which can lead to a large change in the calculated transfer efficiency. In our case, the use of heme as FRET acceptor avoids labeling of the protein with artificial dyes, which often is very challenging (see below). Any substoichiometric labeling of the molecules with the donor fluorophore is less problematic, as non-labeled molecules do not contribute to

the donor intensity (*i.e.* they do not modify the results; they only become "invisible" to the detection system).

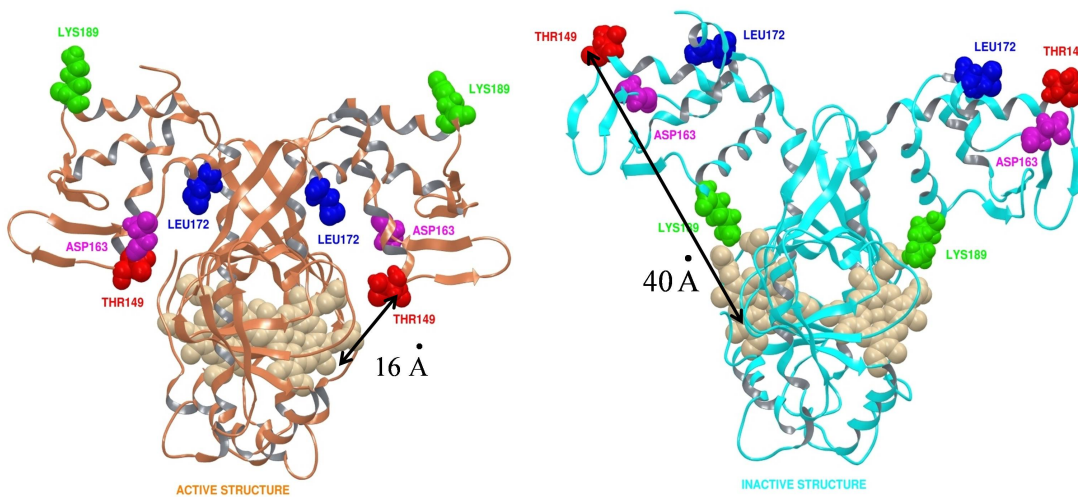


**Figure 2.3:** Structure of the inactive form (right) and model of the active DNA-binding form (left) of CooA from *R. rubrum*. In red, Thr149, which has been used for labeling.

Initially, we also aimed at using intra-protein FRET in order to characterize the active and the inactive structures of CooA. Similarly to what has just been described, the idea was to label CooA with ATTO-390 as FRET donor and to use the heme of CooA as FRET acceptor (following the procedure explained in section 6.12). Molecular modeling of the inactive *R. rubrum* CooA structure (performed by J.-C. Lambry in the LOB), using as basis the inactive X-ray structure [68], the crystal structure of the imidazole-bound form of CooA from *Carboxydotherrmus hydrogenoformans* [69] and the *E. coli* CAP-DNA structure [70] indicated the residue threonine 149 (T149) in CooA as good candidate for labeling. T149 is surface-exposed in the non-active form of CooA (in which the labeling is performed) and its relative position with respect to the heme is expected to change quite substantially between the active and the non-active forms (see Figure 2.3). As both donor-acceptor distances ( $\sim 40 \text{ \AA}$  in the inactive form and  $\sim 16 \text{ \AA}$  in the active form) are smaller than the estimated Förster distance, quenching times close to the picosecond range are expected; a range readily accessible by the time-resolved fluorescence set-up.

However, a low overall labeling yield and loss of the heme cofactor during the labeling procedure using click-chemistry on non-natural amino acids has prevented such measurements to date. Other labeling methods are currently considered that might allow a more efficient labeling of the protein and therefore the study of intra-protein FRET in CooA.

## 2.2 Fluorescence anisotropy measurements

Fluorescence anisotropy measurements were carried out in order to determine the affinity of the transcription factors *CooA* and *DNR* to their target double strand DNA. Such measurements are a powerful tool in biochemical research because of their versatility and simplicity. Fluorescence anisotropy has been widely used, for example, to study the structural order in lipid membranes and proteins [71], to investigate DNA-protein interactions, for example binding of the *CRP* to DNA [72] and to determine the specificity of the tryptophan Repressor - Operator recognition [73].

In fluorescence anisotropy measurements, the anisotropy of excited fluorophores is created in an isotropic sample by excitation with polarized light. The polarization of the emitted light depends on the relative orientation of the absorption and emission transition moments at the time of absorption and emission, respectively. When exposed to polarized light, fluorophores that have their absorption transition moments oriented along the electric vector of the incident light will be preferentially excited. Rotational diffusion of the labeled molecule in solution randomizes the direction of the emission transition moments of the fluorophores, therefore partially depolarizing the fluorescence emission [50].

In particular, fluorescence anisotropy is a measure of the average angular displacement of the fluorophore that takes place during the lifetime of the excited state. This angular displacement is dependent upon the rate of rotational diffusion, which in turn depends on the viscosity of the solvent and also on the size and shape of the rotating molecule. The viscosity of the solution remains constant throughout the experiment, whereas the shape and size of the fluorescent molecule change as protein is added to the DNA ligand solution in order to form a DNA-protein complex. In our case, the fluorescent molecule is *ATTO-390* attached to a double stranded DNA oligonucleotide (see section 6.13 in Material and Methods for the characteristics of the labeled DNA). Protein-DNA complex formation increases the molecular volume of the labeled entity, slowing down its rotational movement and therefore increasing anisotropy values. DNA is preferentially labeled because it is the smallest partner in the DNA-protein complex. This implies that, upon complex formation, the change of shape and size (and hence also the change of anisotropy) will be larger than when labeling the protein.

### 2.2.1 Theory of fluorescence anisotropy

Fluorescence anisotropy is a dimensionless quantity independent of the total fluorescence intensity of the sample, and therefore, also independent of the concentration of the fluorophore. In a common experiment, outlined in Figure 2.4, the fluorescent sample is excited with vertically polarized light and the intensity of the vertical ( $I_{\parallel}$ ) and the horizontal ( $I_{\perp}$ ) components of the emitted light are determined. The anisotropy, ( $r$ ) is defined as:

$$r = \frac{I_{\parallel} - I_{\perp}}{I_{\parallel} + 2I_{\perp}}. \quad (2.3)$$

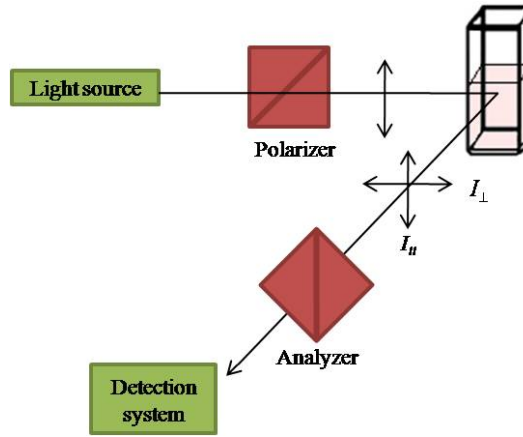


**Figure 2.4:** Schematic drawing for the measurement of fluorescence anisotropy. The sample is excited with vertically polarized light.  $I_{\parallel}$  and  $I_{\perp}$  respectively represent the parallel and the perpendicular components of the emission light.

An L format set-up is often used because only a single emission channel is required. Emitted light is detected with a system with usually different transmission efficiencies for vertically and horizontally polarized light. As a consequence, the measured intensities  $I_{VV}$  and  $I_{VH}$  cannot be directly used and a correction factor ( $G$ ) must be determined, that describes the ratio of the sensitivities for vertically and horizontally polarized light. The  $G$  factor can be determined as shown in Figure 2.5 by using horizontally polarized excitation.

$$G = \frac{I_{HV}}{I_{HH}}. \quad (2.4)$$

Therefore, Eq 2.3 becomes:

$$r = \frac{I_{VV} - GI_{VH}}{I_{VV} + 2GI_{VH}}. \quad (2.5)$$

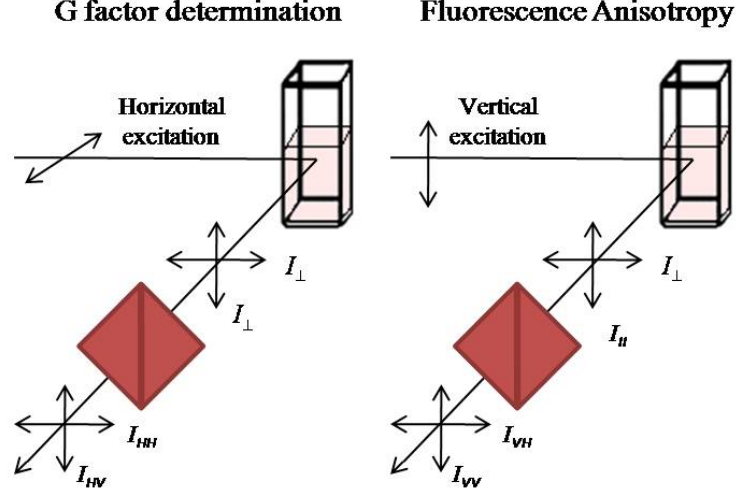


**Figure 2.5:** The left part of the scheme shows how the G factor can be determined by exciting the sample with horizontally polarized light. In this case, both horizontally and vertically emitted light components are perpendicular to the incident light and therefore have identical intensity. The fluorescence anisotropy can be obtained by exciting with vertically polarized light and by applying afterwards the G correction factor to the measured  $I_{VV}$  and  $I_{VH}$ .

## 2.2.2 Values for anisotropy and excitation photoselection

For the sake of simplicity, we first describe eq. 2.6, which corresponds to the anisotropy for a given set of fluorophores, distributed over the angle  $\theta$  with respect to the z-axis (in our case, the z-axis coincides with the orientation of the excitation light). We consider parallel absorption and emission transition moments, absence of rotational diffusion and symmetry with respect to the z-axis. Then, the anisotropy is given by [50]:

$$r = \frac{3 \langle \cos^2 \theta \rangle - 1}{2}. \quad (2.6)$$

Equation 2.6 is obtained when considering that the emitting fluorophores behave as radiating dipoles. In this case, the parallel and the perpendicular intensities can be calculated, being proportional to the square of the electric field, as explained in [50]. Eq. 2.6 is obtained by substitution of intensity values in eq. 2.3.

Assuming a single vertically oriented fluorophore ( $\theta=0$ ) and taking into account eq.

2.6, the maximum obtained anisotropy is  $r=1$ . For a set of fluorophores with random ground-state distribution, anisotropy is induced by photoselection: the probability of absorption of a fluorophore in the one-photon excitation regime is proportional to  $\text{Cos}^2\theta$  [50]. Integrating an isotropic distribution over  $\theta$ , we obtain an average value  $\langle \text{Cos}^2\theta \rangle = \frac{3}{5}$ , which, substituted in eq. 2.6, gives an observable value for the anisotropy of  $r=0.4$  (case where  $I_{\parallel} = 3I_{\perp}$ ). Again, this value corresponds to a solution of fluorophores excited along the z-axis which have collinear absorption and emission transition moments and in the absence of any depolarization process.

For most solutions, however, experimental anisotropy values are smaller than 0.4 because the absorption and the emission transition moments make an angle  $\alpha$  (intrinsic to the fluorophore, not due to rotational diffusion or any other depolarizing effect). As a consequence, the anisotropy must be multiplied by a factor which can be expressed, by analogy to the derivation of eq. 2.6, as  $(\frac{3\text{Cos}^2\alpha-1}{2})$ , giving the following expression for the fundamental anisotropy:

$$r_0 = 0.4 \left( \frac{3\text{Cos}^2\alpha - 1}{2} \right). \quad (2.7)$$

Anisotropy values can be also negative for specific fundamental anisotropies, with a minimal value of  $r_0 = -0.2$ . Therefore, we can conclude that for any solution with randomly distributed fluorophores and in the single photon absorption regime, the fundamental anisotropy will range from -0.2 to 0.4.

In our experiment, the fundamental anisotropy is given by the fluorophores' properties, which are considered to remain constant throughout the experiment (if we assume that binding of the protein to DNA to form the DNA-protein complex does not affect the fluorophore itself). We are interested in changes in anisotropy due to the rotational diffusion of fluorophores, *i.e.* by reorientation within the fluorescence lifetime. In this case, in order to calculate the anisotropy due to the rotational diffusion,  $r_{rd}$ , another decreasing factor must be taken into account, which, again by analogy to eq. 2.6, can be defined as  $\frac{3\langle \text{Cos}^2\beta \rangle - 1}{2}$ , giving the final expression for the anisotropy:

$$r_{rd} = r_0 \left( \frac{3\langle \text{Cos}^2\beta \rangle - 1}{2} \right), \quad (2.8)$$

where  $\beta$  is the angle that a fluorophore rotates within its excited state.

Finally, we note that we can *avoid* the polarization effects by placing the emission analyzer at  $\varphi = 54.7^\circ$  (where  $\varphi$  is the angle of the analyzer with respect to the vertical axis), called *magic angle*,  $\text{cos}^2\varphi = 1/3$ .

### 2.2.3 Results of fluorescence anisotropy measurements

In order to quantitatively investigate the DNA binding affinity of the protein, fluorescence anisotropy measurements have been performed of labelled DNA as a function of protein concentration.

Figure 2.6 shows binding titrations for the CooA-CO DNA-ATTO-390 complex. CooA-CO is the active form of the protein, where binding to DNA is enabled. We first focus on the anisotropy results.

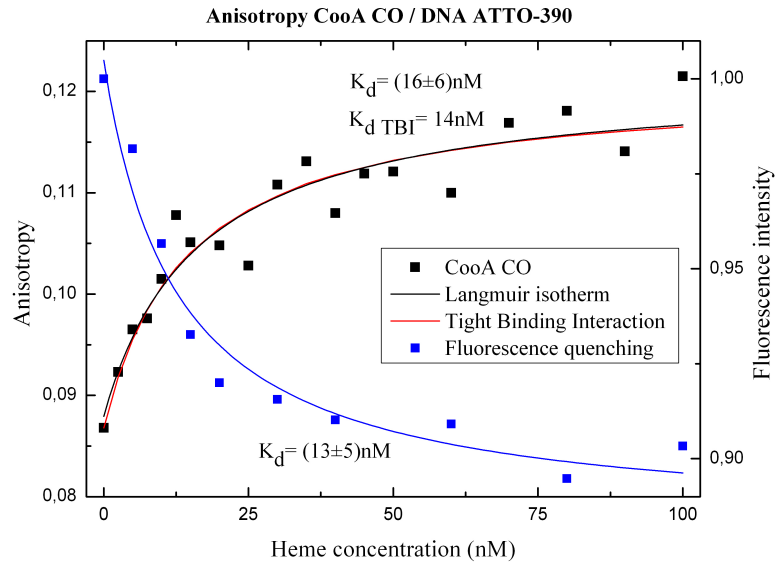


**Figure 2.6:** In black, anisotropy results for ATTO-390 labelled DNA binding to CooA CO-form (active) binding.  $K_d$  has been obtained using fits to both the Langmuir isotherm (black curve) and the Tight Binding Interaction formalism (TBI, red curve), showing similar values. In blue, total fluorescence (total fluorescence calculated as:  $I_{VV} + 2GI_{VH}$ ) is plotted, which occurs as a result of energy transfer going from ATTO-390 to the heme when the protein binds the labeled DNA. Dilution due to the addition of protein to the DNA solution has been corrected and the fluorescence quenching has been fit with the Langmuir isotherm, giving a similar  $K_d$  to the one found for the anisotropy.

From the anisotropy measurements, the dissociation constant  $K_d$  can be calculated. We assume equilibrium conditions (waiting  $\sim 30$  seconds after protein addition to the DNA solution so as to ensure complete protein-DNA equilibration) and we consider that under most conditions, the concentration of DNA is less than that of the protein. Therefore, formation of the complex does not significantly diminish the concentration of the free protein in solution [74]. Within these conditions, we can use the Langmuir isotherm equation:

$$\frac{[DP]}{[D]} = \frac{1}{1 + \frac{K_d}{[P]}}. \quad (2.9)$$

where  $[DP]$ ,  $[D]$  and  $[P]$  refer to the concentration of binary complex, DNA and unbound protein respectively. Fitting to this equation yields a dissociation constant of  $K_d = 16 \pm 6$  nM, which is very similar to the value  $K_d = 13 \pm 2$  nM published in [65]. Because CooA presents a binding affinity of the same order of the DNA concentration (6.4 nM), we also calculate the dissociation constant using the more general Tight Binding Interaction formalism [74], where the diminution of the free protein concentration  $[P]$  by complex formation is taken into account.

$$[DP] = \frac{([D] + [P] + K_d) - \sqrt{([D] + [P] + K_d)^2 - 4[D][P]}}{2} \quad (2.10)$$

The dissociation constant obtained by fitting the data to equation 2.10 is within the error of the one found using the Langmuir isotherm, indicating that the assumption of a constant concentration of free protein is reasonable given the signal to noise.

Because energy transfer is largely dependent on the distance between ATTO-390 and the heme (see section 1.6), by using this fluorescent label we can study not only changes in anisotropy, but also fluorescence quenching (total intensity decay). Both measures can in principle yield information about the protein-DNA interaction. For the interaction CooA-CO / DNA ATTO-390, we observed indeed that upon total protein binding fluorescence is quenched, by  $\sim 12\%$  (asymptotic value from the fit, Figure 2.6). Using the Langmuir equation, we obtain a dissociation constant of  $K_d = 13 \pm 5$  nM, which is in good agreement with the value obtained from the anisotropy measurement. The limited degree of quenching indicates that the distance between the fluorophore and the heme is larger than the Förster distance (ATTO-heme distance about  $1.4R_0$ ,  $R_0$  is estimated at  $\sim 50$  Å for our particular system; see section 2.1), as will be further discussed in section 2.3.

One can also notice that if, as discussed above, anisotropy is a measure of the ratio between the rotational diffusion of the fluorescent molecule and the lifetime of its excited state,  $\tau_{rot}/\tau_{fl}$ , then the change of anisotropy in the particular case of DNA-ATTO-390 / CooA-CO does not only depend on the rotational slowing down of the molecule (decrease of  $\tau_{rot}$ ) when a larger complex is formed due to protein binding to DNA, but it also depends on the fluorescence quenching due to energy transfer which reduces the effective fluorescence decay time,  $\tau_{fl}$  (see section 2.3). Both effects go in the same direction, further increasing the anisotropy values as the protein-DNA

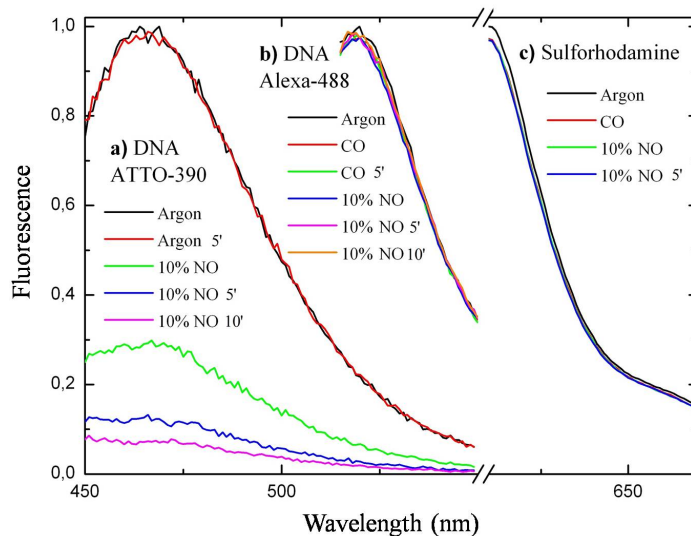


**Figure 2.7:** a) Effect of CO and NO on fluorescence intensity from DNA (DNR) ATTO-390. The intensity of the fluorescence decreases dramatically and in a time dependent manner when the DNA solution is equilibrated with 10% NO, whereas it stays constant for argon equilibration. b) Effect of CO and NO on DNA (DNR) Alexa-488. No degradation of the dye is observed for Alexa-488 when the solution is equilibrated with either CO or NO (even for long times after equilibration), suggesting that DNA Alexa-488 is a suitable label for anisotropy measurements. c) Effect of NO on sulforhodamine (of which Texas Red is a derivative). Intensity values do stay constant when the sulforhodamine solution is equilibrated with either CO or NO. All the measurements have been performed at *magic angle*.

complex forms.

We also studied binding of DNR to ATTO-390-labeled DNA. This transcription factor is able to bind the presumed *nor* promoter target DNA in the active, NO-bound form [75]. Experimentally, as explained in the Materials and Methods (section 6.13), the DNA solution must be equilibrated with 10% NO (in order to avoid DNR to partially denitrosylate when it is added to the DNA solution). We found that the addition of NO to the labeled DNA solution degrades the dye (see Figure 2.7a), resulting in a strong decrease of ATTO-390 fluorescence during the experiment. As this complicates reliable anisotropy measurements, reproducible titrations could not be performed.

As an alternative to ATTO-390, we labeled *nor* promoter target DNA with Alexa-488, which is a more photostable than ATTO-390 [67] (see figure 2.1). We have tested the reactivity of Alexa-488 with NO, observing no degradation of the dye upon NO exposure (Figure 2.7b).

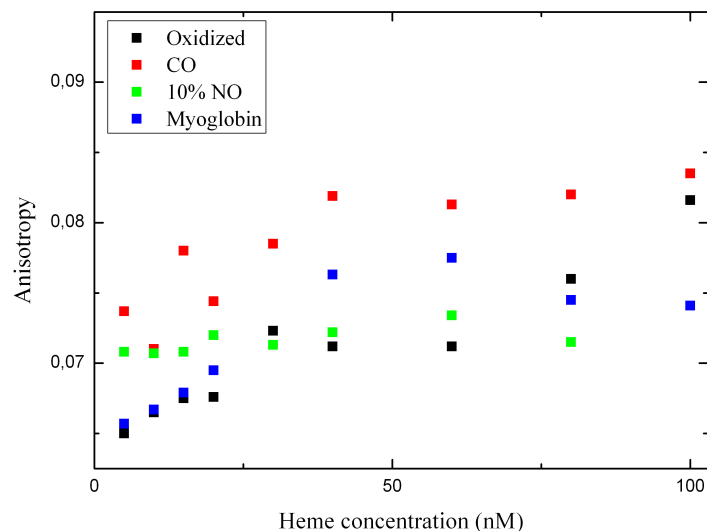


**Figure 2.8:** Anisotropy results for DNR-DNA Alexa-488. Anisotropy does not significantly increase with increasing heme concentration for any protein form. This suggests that the dye linked to the DNA has a flexible flag which allows Alexa-488 to rotate with a high rate independent of the DNA rotation. This may explain the small initial values for the anisotropy and also the incapability of the dye to detect the binding of the DNR to the DNA.

Figure 2.8 shows the anisotropy for DNA Alexa-488 and DNR in different forms. No differences can be observed between the non-active forms (oxidized, CO-form) and myoglobin, where binding is not supposed to occur, and the assumed active form (10% NO). The initial very low values, which remain roughly constant during protein addition to the DNA solution, suggest a high rotational flexibility of Alexa-488, independent of the rotation of the DNA itself. This finding may be related to the length of the commercial linker used for labeling, which can allow for significant segmental motion of the dye [76]. Altogether, the commercially available Alexa-488 labeled DNA is an inadequate probe for this particular protein-DNA binding.

Finally, we studied the activity of CooA and DNR by labeling their respective target DNAs with Texas Red, a derivative of sulforhodamine. Upon exposure to CO and NO, no degradation of the dye was observed, as shown in Figure 2.7c. Figures 2.9 and 2.10 show the anisotropy measurements. We observe that non-active forms of both proteins, reduced CooA and DNR and CO-bound DNR, exhibit constant values for the anisotropy consistent with the fact that no binding to DNA occurs. On the other hand, as expected for the active forms of the proteins, CO-bound CooA and NO-bound DNR, the anisotropy increases upon protein addition. Anisotropy

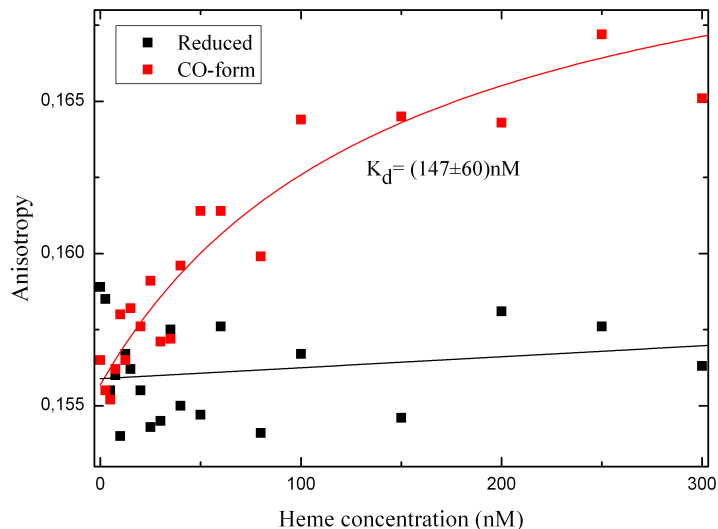


**Figure 2.9:** Anisotropy results for binding of CooA to Texas Red-labeled DNA. CooA in the reduced form (black squares) does not bind DNA and the anisotropy remains constant. Active CO-bound CooA (red squares) binds DNA, resulting in an increase in anisotropy as the complex CooA-DNA rotates more slowly.

data were fitted with the Langmuir equation for both CooA and DNR, resulting in  $K_d = 147 \pm 60$  nM for CooA, and  $K_d = 44 \pm 9$  nM for DNR. For CooA, the affinity is somewhat lower than what we found using ATTO-390 labeled DNA. This difference may arise from the fact that Texas Red is a larger fluorophore compared to ATTO-390 and may therefore interfere with protein-DNA interaction. The affinities are also lower than the affinity reported by Thorsteinsson *et al.* for active CooA-binding to Texas Red-labeled DNA [65] and could potentially originate from differences in the position of the fluorescent label (attached to the 5'-end in our case; information not provided in [65]) that may differently influence the interaction between the DNA double strand and the binding site on the protein.

Binding of DNR to the *nor* promoter DNA has been observed using radio-labeled DNA, but the binding affinity was not quantified and no NO-dependence had been observed [37]. Therefore, the present work provides the first evidence of NO-dependent DNA binding and the first determination of the binding constant.

In conclusion, our anisotropy measurements provide evidence for the binding of the active forms of CooA and DNR to the target DNA and demonstrate that activation is induced by specific diatomic ligands: CO for CooA and NO for DNR. We could not determine the dissociation constant for DNR-NO and DNA ATTO-390 due to

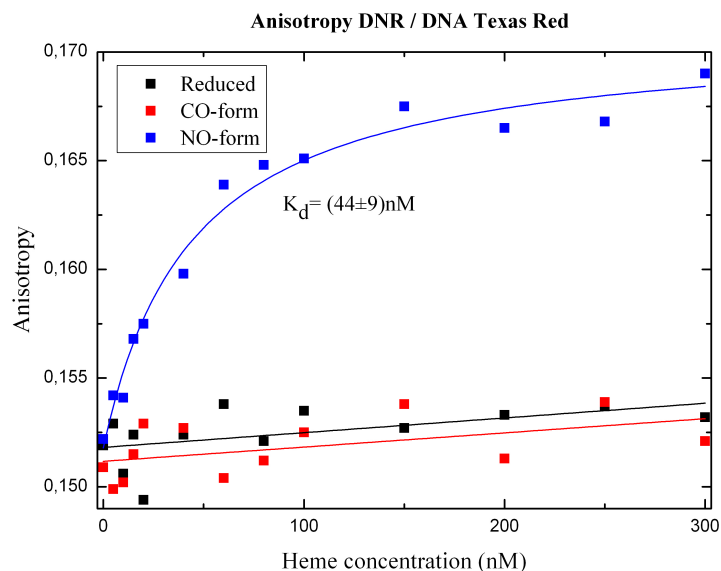


**Figure 2.10:** Anisotropy measurements for binding of DNR to Texas Red-labeled *nor* promoter DNA. Neither the reduced (black squares) nor the CO-bound form of DNR (red squares) are active, resulting in constant anisotropy values. In the NO-bound form (blue squares), DNR is active and binds to the promoter sequence, as demonstrated by the increase in anisotropy.

degradation of the dye in the presence of NO. As an alternative, DNA was labeled with Texas Red, showing binding values for CooA-CO and DNR-NO which are both in the same range, and in particular for CooA, are somewhat lower than published data and what we observed with ATTO-390. These differences may originate from differences in the particular labeling of DNA, resulting in interferences of the relatively large Texas Red chromophore with the protein-DNA interaction. Anisotropy measurements on CooA-CO and DNA ATTO-390 were performed, giving a dissociation constant very similar to published data. We also provide evidence for fluorescence quenching due to energy transfer from the dye to the heme in the protein, obtaining results in excellent agreement with anisotropy measurements.

In the following section, we will explore the origin of this quenching in time-resolved experiments.

## 2.3 FRET observed by time-resolved fluorescence spectroscopy

The binding of CooA to ATTO-390-labeled promoter DNA has also been studied by transient fluorescence spectroscopy, using the set-up described in section 6.15. In these experiments, we have measured the decay of the donor fluorescence both in absence and presence of CooA-CO, that is able to bind DNA. The experiments with the protein-DNA complex have been performed under conditions where all DNA is bound to CooA. This is important, since any unbound labeled DNA may lead to erroneous determination of the decay rate in the hypothetical bound-form.

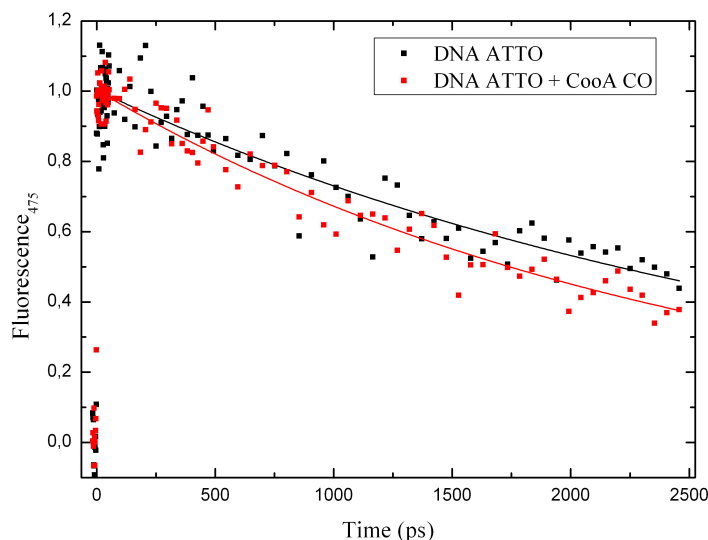


**Figure 2.11:** Fluorescence kinetics at 475 nm of ATTO-390 in the absence of CooA-CO (black squares) and in its presence (red squares). Formation of the protein-DNA complex leads to a  $\sim 20\%$  faster fluorescence decay as a consequence of the energy transfer from ATTO-390 (donor) to the heme of CooA (acceptor).  $25 \mu M$  CooA and  $20 \mu M$  DNA were used in the experiments.

Figure 2.11 shows the results obtained. The monoexponential fitting of DNA ATTO-390 gives a time decay of  $3160 \pm 160$  ps. This is somewhat shorter than the lifetime of the fluorophore alone (*i.e.* not bound to the DNA) of  $\sim 5$  ns [66]. This result indicates that DNA labeling with ATTO-390 has a quenching effect on the time decay of the fluorophore itself, a feature commonly observed in DNA-dye complexes [77]. On the other hand, the fitting for the complex CooA-DNA gives a decay time of  $2500 \pm 70$  ps,  $\sim 20\%$  faster than in the previous case. This experiment gives evidence

of energy transfer occurring between the donor placed in the DNA and the heme incorporated in the protein. Similar values for the FRET were obtained in section 2.2.3 with the steady state experiments, where a total fluorescence quenching of  $\sim 12\%$  was found. The time-resolved experiments assess that the observed steady-state quenching effect is due to an overall modest acceleration of the fluorescence decay by quenching and not by a strong quenching in a small population of the donor-acceptor pairs.

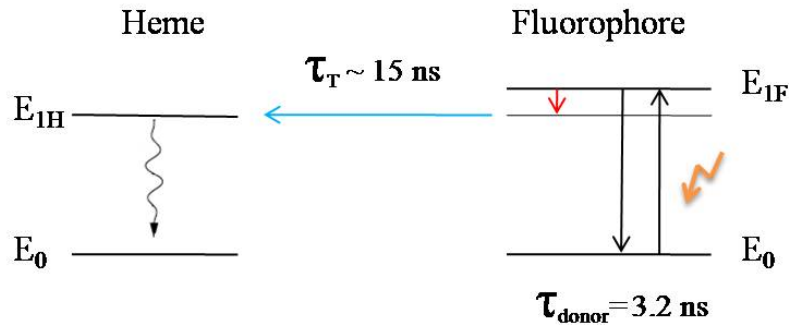


**Figure 2.12:** Diagram for decay of ATTO-390 in the presence of heme. The decay times are estimated from the time-resolved fluorescence experiments.

An estimation of the donor-to-acceptor distance can be done by making use of equation 1.1. As indicated in Figure 2.12, a decay 20% faster for the complex CooA-DNA (see Figure 2.11) than for DNA alone implies that energy transfer from the dye to the heme is  $\sim 5$  times slower than the decay time of the fluorophore in the absence of the acceptor. With these values, the donor-to-acceptor distance obtained is  $\sim 65 \text{ \AA}$ . Molecular modeling studies were performed by J.-C. Lambry in our department to investigate the donor-to-acceptor distance. In this model (structure shown in Figure 2.13), the label, modeled as a rigid linker-chromophore molecule, is linked to the forward 5' strand of the DNA. With this binding geometry, the calculated distance is  $\sim 62 \text{ \AA}$ , which is in very good agreement with the result estimated from the 20% faster decay of the fluorescence in the case of the CooA-DNA complex. Therefore, we can conclude that the use of FRET coupled to a transient fluorescence spectroscopy system proves to be suitable for the study of distances, even when these are slightly larger than the Förster distance of the corresponding system. We note that in our present study the donor-to-acceptor distance is substantially larger than the distance between the heme and the labeled nucleotide itself ( $\sim 40 \text{ \AA}$ ). In future studies, enhanced FRET effects may be expected if shorter linkers are used. Future studies may also allow following the dynamics of DNA binding and release by the use of fluorescence

quenching.

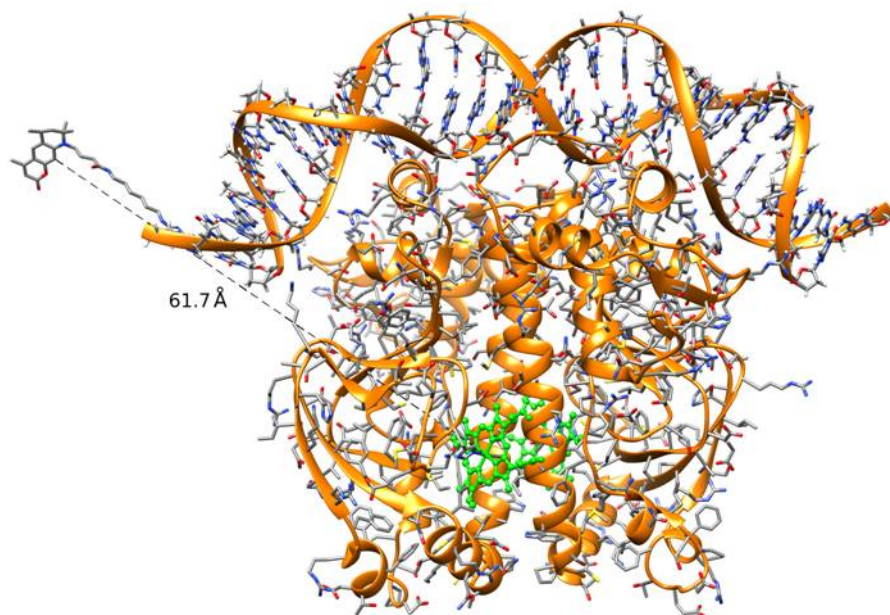


**Figure 2.13:** Molecular modeling of the CooA-DNA complex where the DNA is labeled with ATTO-390 at the position 5' (forward strand). This allows for the donor-to-acceptor distance estimation.

## 2.4 Circular dichroism measurements

Circular dichroism (CD) can be described as the differential absorption of right and left circularly polarized light [78, 68]. In order to have a CD signal, the sample must exhibit an optical activity, *i.e.* it must rotate the polarization of the incident light.

Chiral molecules are molecules with non-superposable mirror images [79]. Proteins are chiral macro-molecules and are therefore appropriate for CD studies. It is of note that the CD signals in biological samples are very small, with a difference in absorbance of the order of  $3 \times 10^{-4}$  [80]. Furthermore, considering the DNA double helix, the chiral arrangement of the nucleic acids makes these molecules optically active as well [81].

In order to obtain a CD signal from a protein, measurements must be performed at specific regions of the spectrum where the molecule absorbs. CD measurements provide different kinds of information depending on the spectral region [80]. In the far UV, below 240 nm, the absorption is mainly due to the peptide bonds, providing information about the secondary structure of the proteins. In principle, in this region,

a quantitative analysis of the data is possible, allowing determining the proportion of  $\alpha$ -helices,  $\beta$ -sheets and random coil that the sample contains. In the near UV region, between 260 and 320 nm, the CD signal arises from the aromatic amino acids. The shape and magnitude of the CD spectra depend on the relative position of these amino acids, the nature of their three-dimensional environment, their mobility and the proportion in which each amino acid is present. The complexity of the signal in this region makes the quantitative analysis very difficult to perform [80]. Nevertheless, the near UV CD spectrum provides a valuable fingerprint of the tertiary structure of the protein.

In this section we perform CD measurements of CooA, CooA-CO and the complex CooA-CO + DNA in order to *qualitatively* study the extent of the structural changes occurring when the protein-ligand complex is formed.

#### 2.4.1 Results of CD measurements

As a reference, we have first performed CD measurements of oxidized Mb and MbCO in the far UV region (200-240 nm) using the setup described in 6.16. Oxidized Mb has been prepared as explained in 6.16.1. We have subtracted the CD signal of the buffer in order to retain only the signal of the protein.

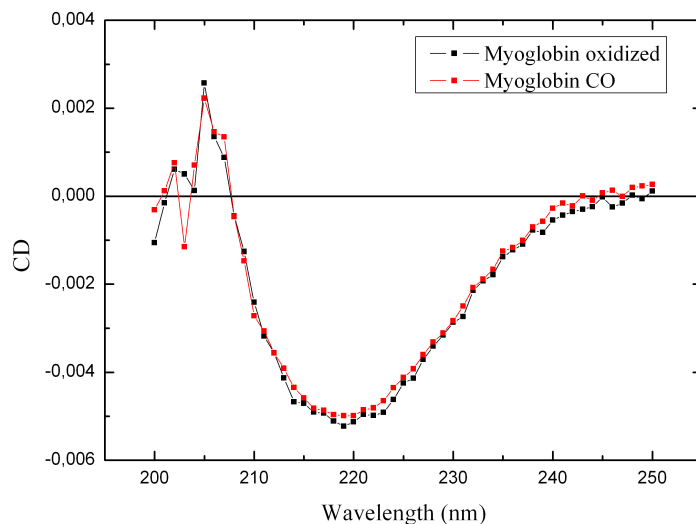


**Figure 2.14:** CD spectra of oxidized Mb and MbCO at pH 6.4.

Figure 2.14 reveals no significant difference for Mb and MbCO (small differences at  $\sim 200$  nm are due to saturation effects because of the extremely high absorption of

the protein in this region). This result is expected since the protein does not undergo significant structural changes at the level of the secondary and tertiary structures upon reduction and CO binding. The results are in agreement with those of [79].

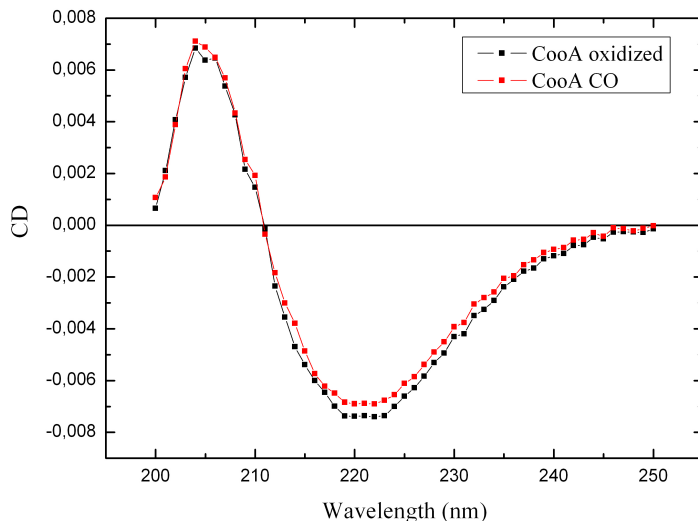


**Figure 2.15:** CD spectra of oxidized CooA and CooA-CO. The two states exhibit slightly different CD signals at  $\sim 220$  nm.

We performed the same experiments for CooA and CooA-CO. Figure 2.15 shows a small difference in the spectra at  $\sim 220$  nm. Changes in the spectra between the two states suggest that a conformational change in the protein occurs in CooA in the reduced and CO-bound form. This finding is in general agreement with the idea that a substantial de-localized movement takes place after binding of the effector gas molecule to the heme [33]. Although yet difficult to interpret quantitatively, these results are very promising in the sense that they provide a perspective of following the dynamics of switching between the active and inactive form of CooA, when connected to CO-photolysis or stopped-flow techniques.

As a next step, we investigated the effect of DNA binding to the CooA-CO complex. Here, not only the protein CD, but also the DNA CD may contribute to the spectra. Figure 2.16 compares the sum of the separate CD spectra of DNA and of CooA-CO with the CD spectrum for the DNA-CooA-CO complex. As before, we subtract the CD spectrum of the buffer (in this case Tris-HCl; see 6.13) and we normalize with respect to the concentrations of each sample. A spectral red shift is observed in the CD spectrum of the DNA-CooA-CO complex compared to the sum of the individual CD spectra of DNA and CooA-CO. In this region, signals from both DNA and protein

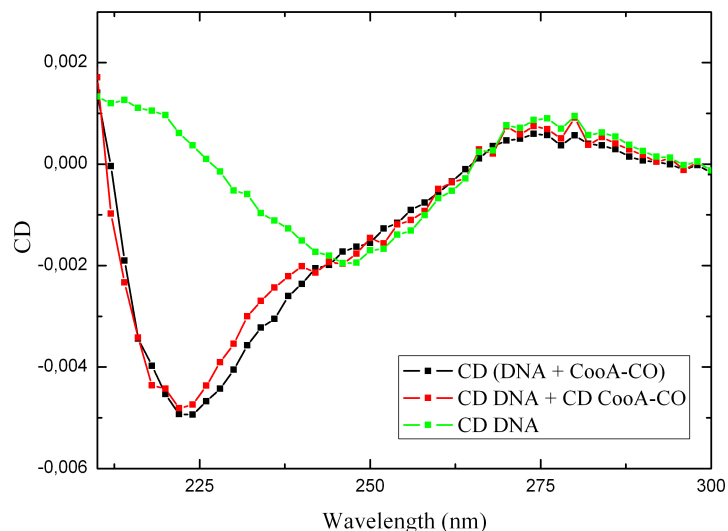


**Figure 2.16:** Global comparison between the CD spectra for CooA-CO and DNA when they are not bound (red) and when they form the complex DNA + CooA-CO (black). The CD spectrum of DNA only (green) shows no significant differences with the other two curves in the region 250 - 300 nm.

contribute to the signal. Two observations indicate that the change predominantly arises from the protein contribution:

1. In the range where only DNA contributes ( $>250$  nm), no significant change is observed.
2. The difference signal is characterized by a shift of the 220 nm minimum that originates from the protein backbone.

Thus, it appears that whereas CO binding to CooA changes the amplitude of the protein signal, DNA binding changes its position. Figure 2.17 highlights this effect, by subtracting the contribution of the DNA itself (under the assumption that it does not change itself).

We conclude this section by emphasizing that these experiments open new and interesting perspectives for future work. Indeed, the protein response to CO dissociation, by flash photolysis, may be investigated by CD experiments in the nanosecond to millisecond timescale. Reversely, the protein response to CO binding, and also DNA binding, may be studied, with millisecond resolution, by CD stopped flow experiments. Specifically, it has already been suggested that DNA binding reduces the structural

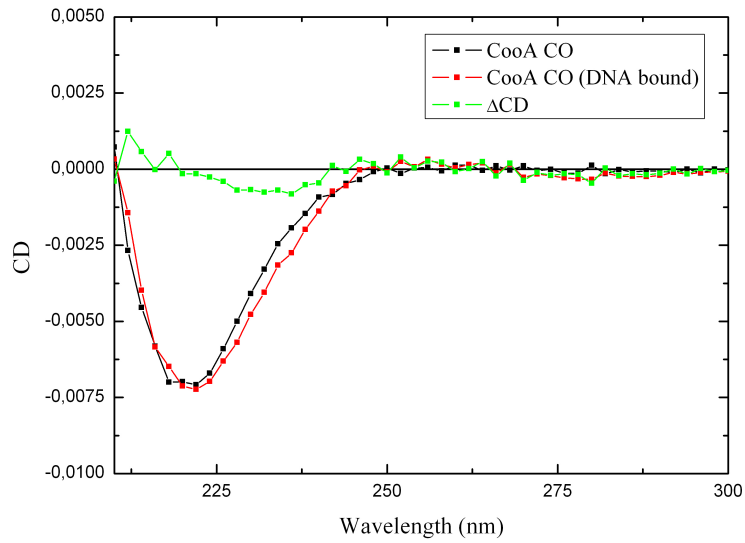


**Figure 2.17:** CD spectra of CooA-CO (black, from Fig. 2.15) and CooA-CO bound to the target DNA (red, obtained by subtracting the DNA-only signal from the signal of the protein-DNA complex in Fig. 2.16). A small shift of the signal is produced in the 220-240 nm region when the protein binds to the DNA, which is highlight by the difference of CD signals (green).

heterogeneity in the heme-binding domain [73, 80], and the DNA-induced CD change that we monitored (Fig. 2.17) may be the signature of this effect.

## Chapter 3

# Ultrafast ligand dynamics in CooA and DNR and comparison with other heme proteins

Heme-based sensor transcription factors act as bistable switches, where binding of a diatomic gas molecule to the heme (CO in the case of CooA and NO in the case of DNR) alters the DNA binding properties of the protein. Binding of the effector molecule brings about a change in protein configuration, allowing formation of the protein-DNA complex and the subsequent transcription of specific genes by RNA polymerase. Physiologically, heme-ligand bonds are disrupted thermally, in a purely stochastic manner. Experimentally, however, these processes can be synchronized using short photodissociation light pulses, and the early processes in the intra-protein signaling pathway can therefore be followed using ultrafast optical spectroscopic techniques [2]. In the study described below, we have performed ultrafast visible transient absorption spectroscopy using the setup described in section 6.11 to study the ligand dynamics in CooA and DNR.

Immediately after photodissociation, the dissociated ligand remains in the distal heme pocket. From there, it can either rebind to the heme or escape out of the heme pocket and migrate towards the solvent. Analysis of the dynamics of ligand binding and escape provides information about the mechanistic implication of these diatomic gases in early signaling events and provides insight in how the pathway of the dissociated ligand is controlled by the protein environment [34]. Thus, characterization of these primary processes, which usually occur on the picosecond time scale, is essential for the complete understanding of the switching mechanism of these proteins [2].

In the first section of this chapter we present a study of the rebinding of CO to WT CooA and mutants of the N-terminal proline residue. In the second section, the ligand-dynamics in DNR is presented, showing (in particular) for the first time the NO-recombination kinetics. Finally, in the third section, the activation barriers involved in CO rebinding to the heme and CO escape out of the heme pocket are investigated in several proteins by temperature and viscosity dependence measurements.

### 3.1 CO-rebinding in CooA wildtype and mutant proteins

DNA binding to CooA is triggered by the binding of CO to the Fe(II) in the heme [82], inducing the required conformational change of this transcription factor to its active form [82, 10]. Reversely, the dissociation of CO causes the switch from the active structure of CooA to the inactive one. Therefore, the study of the CO-CooA photodissociation and the geminate recombination process is important for the understanding of the protein function.

Figure 3.1 (top part) shows the transient spectra of the CO-recombination at different times after CO photodissociation. The spectra are characterized by a bleaching of the CO-bound form, centered at  $\sim 422$  nm, and an induced absorption, centered at  $\sim 436$  nm, attributed to the 5-c form. Apart from the first few ps (see below), the shape of the transient spectrum does not change within the time range investigated (4 ns). The full spectro-temporal data of the CO-recombination decay were globally fitted with Glotaran<sup>1</sup> (open-source software [83]) and the decay at a single wavelength (436 nm) is shown in the bottom part of Figure 3.1. The CO-recombination can be fitted well by a two exponential decay function with a fast component of  $\sim 75$  ps (58%), a slower component of  $\sim 670$  ps (33%) and a non-decaying component of  $\sim 9\%$  relative amplitude. The latter constant corresponds presumably to CO escape from the heme pocket. We also observed a minor, faster decay phase of  $\sim 5$  ps with a red-shifted decay-associated spectrum (DAS) that was attributed to relaxation of the excited heme [34]. These features are in agreement with previous studies on WT CooA [34, 84]. These fast heme-CO recombination phases evidently reflect geminate rebinding, as bimolecular rebinding occurs on a much longer timescale [85]. CO-recombination in CooA is very fast and highly efficient, with very little CO escape [16]). This is different from the situation in Mb, where the amplitude of CO geminate recombination is only 4% and it takes  $\sim 180$  ns and hemoglobin, where less than 1% CO recombines (T-state) [86, 82].

---

<sup>1</sup>We remark that from here on, all data were globally fitted with Glotaran.

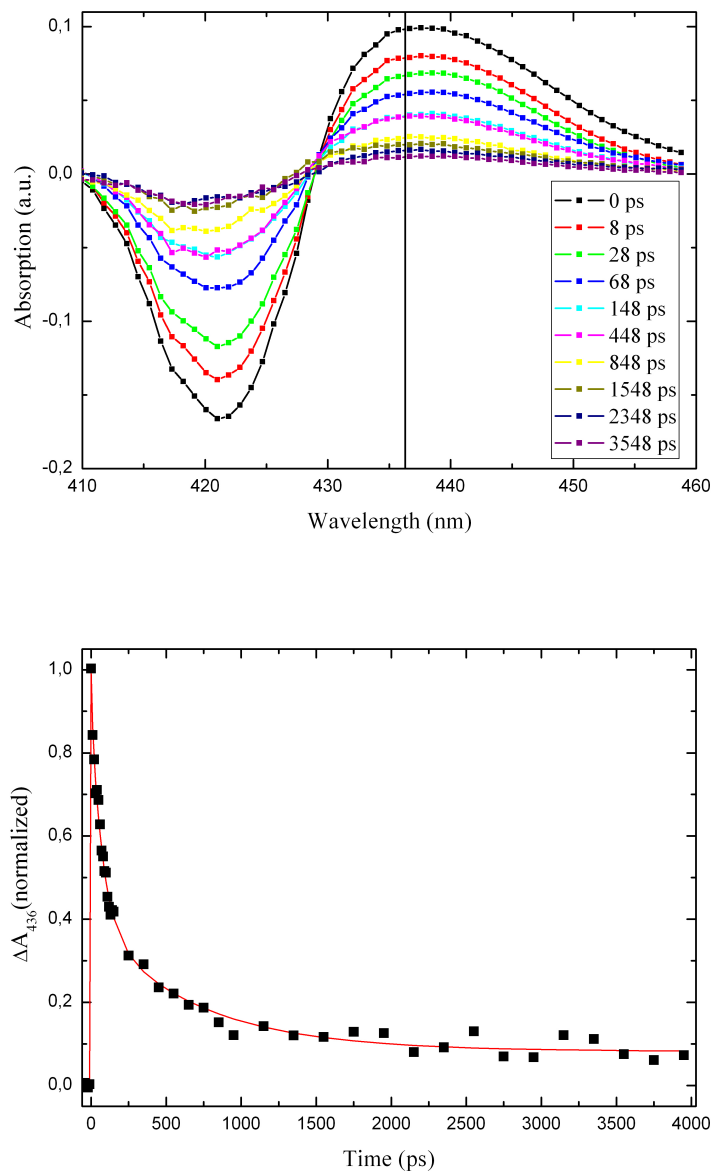


**Figure 3.1:** **Top part:** Transient spectra of the CO-recombination in WT CooA at different times after ligand dissociation. **Bottom part:** CO kinetics at 436 nm (close to the maximum peak of absorption, see vertical line in the top graph), which can be well fitted with a sum of two exponentials ( $\sim 75$  ps (58%) and  $\sim 670$  ps (33%)) and a non-decaying constant component (9%).

Interestingly, the CO geminate recombination kinetics in CooA resemble those of NO-recombination in Mb, although NO has a higher intrinsic reactivity with heme. This suggests that the heme pocket of CooA specifically favours very fast and efficient CO-recombination [34]. In CooA, localization of the heme close to the protein surface

[30] presumably allows relatively high orientational freedom of dissociated CO in the heme pocket and thus the accommodation of CO perpendicular to the heme, a propitious binding orientation. Altogether, functionally the heme pocket in CooA acts as trap for CO once it is bound to the heme iron. This avoids CO escape which would lead to the inactivation of the protein. A similar "trapping" behavior has been observed for other heme-based sensor proteins, specifically with respect to their physiologically sensed ligands [2].

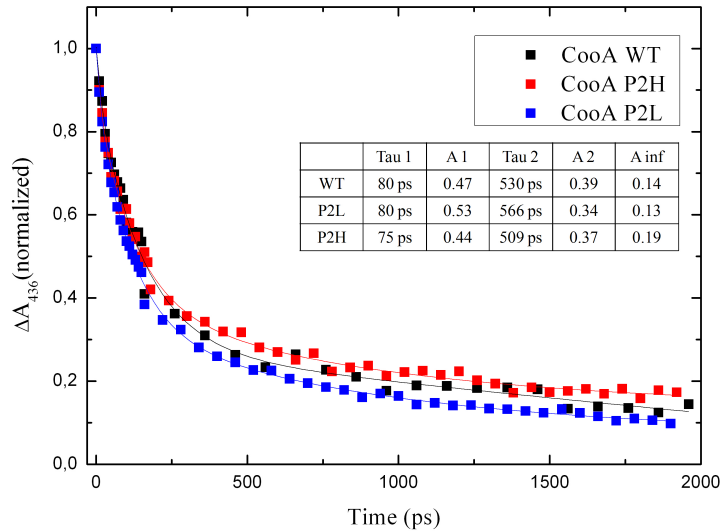


**Figure 3.2:** CO-rebinding in CooA WT (black), P2H (red) and P2L (blue). Solid lines are the fits of the multiexponential decays (time constants and corresponding amplitudes shown in the legend). The rebinding is very similar in all cases, in agreement with the suggested activation mechanism by which the N-terminal is displaced far away from the heme pocket upon CO binding [33].

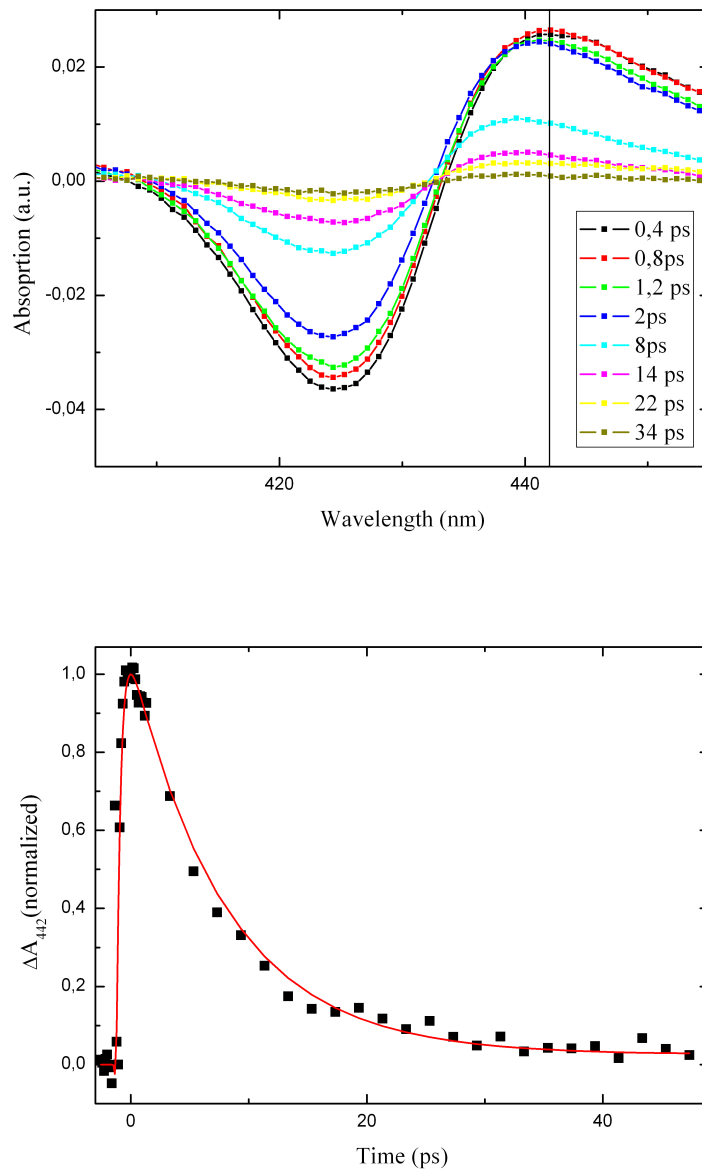
In CooA, the N-terminal proline residue (Pro2) has been identified as distal heme ligand in the inactive form in the absence of CO [30, 10]. De-ligation of Pro2 allows binding of CO to the heme and a subsequent conformational change of the protein to its active form [87, 88]. Models indicate a large change in the position of the distal heme residue upon CO binding to CooA [33]. In order to investigate its role in the kinetics of CO rebinding, we created two site-directed mutants of Pro2: P2H and P2L. In P2H, proline has been substituted by a histidine residue. Histidine has an imidazole functional group and is a ubiquitous heme ligand, where the  $\delta_1$  N can bind to the heme iron. In P2L, proline has been replaced by an aliphatic leucine residue, which can also bind to the heme via the N-terminus.

Figure 3.2 shows the CO-recombination kinetics for WT CooA and the two mutants P2H and P2L. In all cases, the recombination is very similar, suggesting that Pro2 does not directly interact with CO in the heme pocket. As explained above, modeling suggests a large conformational change of the protein backbone upon CO binding. In the presence of CO, Pro2 is thought to be expelled from the heme pocket and moved up to the hinge region, far away from the heme pocket. Our findings are therefore generally consistent with this model. The fact that there is, nevertheless, a small effect on the relative amplitude of the different phases, indicates an allosteric interaction of the heme domain and the DNA binding region.

### 3.2 Ligand-rebinding in DNR

In this section we report the first ultrafast ligand dynamics study of the transcription factor and sensor protein DNR. The 3D structure of the DNR apoprotein, without its heme cofactor, has been determined by X-ray diffraction [39]. It has been determined that heme is required for the NO-dependent DNR activity *in vivo*, in agreement with the property of DNR to bind heme *in vitro*. In the oxidized form, DNR has a 6-coordinate heme that is presumably liganded by two histidine residues [39]. In the fully reduced form, the heme is also in the 6-c form [37], presumably with the same axial ligands. Figure 3.3 (top part) shows the transient spectra upon excitation of reduced DNR. They have the shape expected for 5-c minus 6-c spectra and are assigned, in analogy to other 6-c heme proteins [35], to dissociation of an internal ligand. The rebinding kinetics of the internal ligand (globally fitted) is shown at 442 nm and occurs in  $\sim 8$  ps (bottom part of the Figure). A much faster decay phase of  $\sim 400$  fs with a slightly different spectrum is attributed to the photophysics of the heme right after excitation. The complete recombination of the internal ligand after photodissociated is not surprising, since it is part of the protein backbone, impeding escape. The timescale of recombination is very similar to what is observed for internal residues in other 6-c heme proteins [35]. For Fe(II)-CooA, we measured recombination of the internal ligand within  $\sim 6$  ps (data not shown), a value very similar to the one for DNR. To date however, the lack of structural information on the heme pocket in DNR prohibits further analysis or modelling of this process.

CO-rebinding to DNR has also been investigated. Figure 3.4 shows the recombination (at the 442-nm induced absorption maximum). CO-recombination occurs on the ps timescale and is highly multiphasic with exponential decays of  $\sim 90$  ps (27%), 840 ps (37%) and a non-decaying constant component of 36% relative amplitude.



**Figure 3.3:** **Top part:** Transient spectra of the internal ligand recombination in WT DNR at different times after ligand dissociation. **Bottom part:** Ligand recombination kinetics at 442 nm (close to the maximum of the induced absorption, see vertical line in the top graph), which takes place in  $\sim 8$  ps.

Altogether, CO-recombination in DNR occurs roughly on the same timescale as in CooA, but is markedly less efficient. As DNR, different from CooA, is not a CO-sensor, this finding supports the notion that the highly efficient CO-rebinding in CooA is functionally important for its role as a CO-sensor.

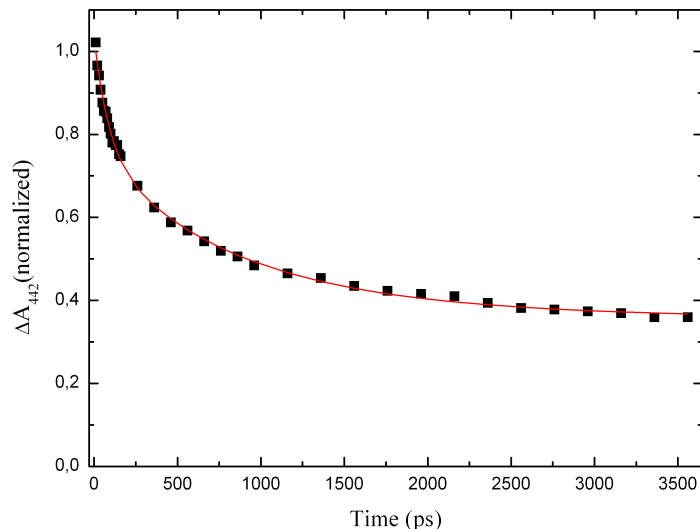


**Figure 3.4:** CO-recombination in DNR, which is multiexponential and has a lower CO-recombination yield than *CooA*.

As DNR activity has been found to be NO-dependent, we next studied the NO-recombination kinetics in this transcription factor. The results are shown in Figure 3.5. Recombination takes place mono-exponentially and very efficiently (more than 90%) with a time constant of  $\sim 10$  ps. (We emphasize that these experiments are challenging since exposure of isolated DNR to NO also leads to faster protein degradation). This process thus occurs on a similar timescale as that of the internal residue rebinding, suggesting that it reflects the intrinsic, barrierless bond formation between NO and heme. (cf. [89], where the fastest phase of NO rebinding to Mb was shown to be temperature-independent). The transient spectra associated with the decay is typical for 4-c *minus* 5-c NO different spectra [90], in agreement with the assesment that the NO-bound form is a 5-c species [37].

Heme-NO recombination generally has a fast phase of 5-10 ps [16], but for most naturally ligand-binding proteins, other phases and sizeable escape yields have been observed. A notable exception is the mammalian NO receptor soluble guanylate cyclase (sGC), in which monophasic near unity QY recombination occurs [90]. The fact that these two NO-sensors have similar behaviour supports the idea that fast NO recombination is a common feature in NO-sensors.

In conclusion, in this section we have reported the first ligand dynamics studies in the transcription factor and NO sensor protein DNR. Recombination of the internal

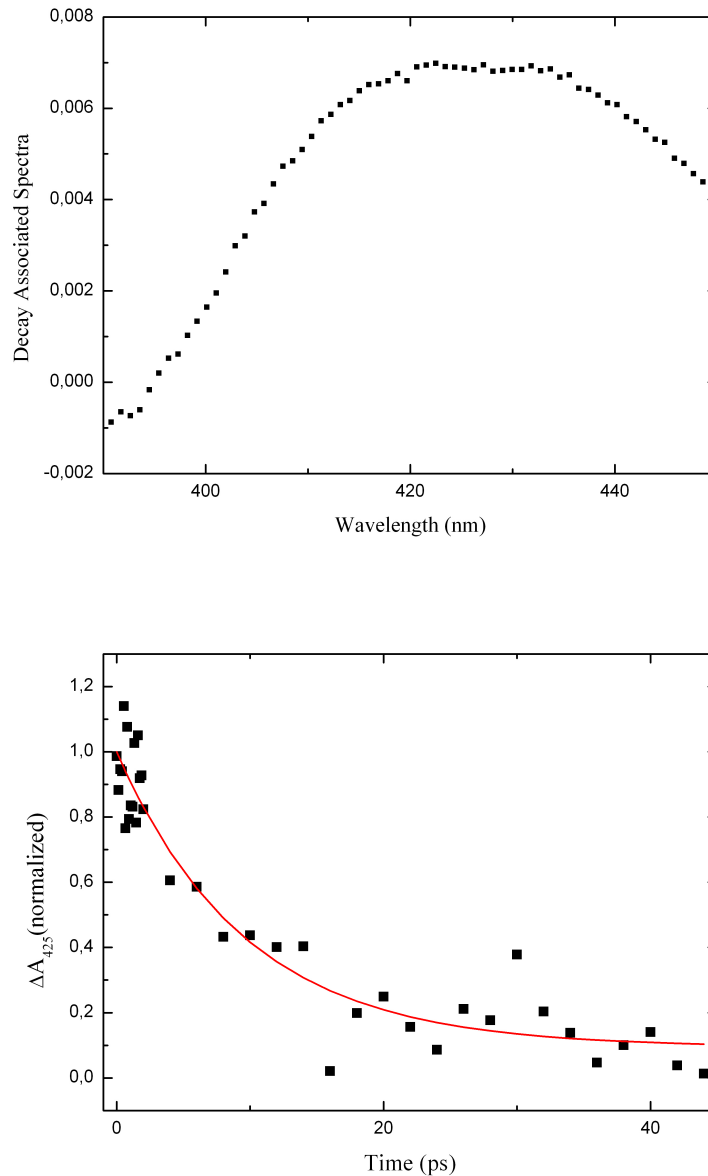


**Figure 3.5:** **Top:** Decay Associated Spectra of the NO recombination phase to DNR. This spectrum is typical for the 4-c *minus* 5-c NO different spectra. **Bottom:** NO-recombination in DNR, which takes place in  $\sim 10$  ps. The red solid line is a fit to a single exponential.

amino acid residue is very fast and efficient, similarly to CooA and other 6-c heme-based proteins. CO recombination in DNR is multiexponential and has similar kinetics as the homologous CO sensor CooA. NO recombination is also very fast and efficient (near complete rebinding with less than 10% NO-escape), supporting the idea that DNR is indeed an NO-sensor.

### 3.3 Temperature dependence study: activation barriers of ligand dynamics

In this section, we report transient absorption measurements performed with the aim to study the barriers involved in CO-rebinding to the heme and escape out of the heme pocket. Studies on the heme-based  $O_2$  sensor Dos from *Escherichia coli* (*EcDos*) (also proposed to be a redox sensor by Shimizu’s group [20]) showed rather unusual CO rebinding kinetics with  $\sim 60\%$  of dissociated CO rebound to the heme in the nanosecond timescale [48, 36]. The fact that rebinding and escape occur with similar rates made *EcDos* a suitable model for studying the activation barriers involved in these processes, using temperature dependence measurements. The results revealed that CO-rebinding is essentially barrierless, while CO-escape is thermally activated [36].

Here we investigate if the picture of barrierless ligand binding and activated escape is a general feature that also applies to other heme proteins. As in [36], we have performed temperature and viscosity dependence measurements of CO dynamics in several heme proteins.

#### 3.3.1 Energy barriers in 6-c heme proteins: CooA and DNR

As seen in section 3.1, CooA exhibits a very high CO geminate recombination yield, larger than in any other heme proteins. Thus, in principle, CooA represents an interesting model for studying barriers involved in ligand rebinding. Regarding the enthalpy of CO-recombination in CooA, a study was performed by Champion *et al.* [84]. Here, recombination of CO to the heme as a function of temperature was analyzed in terms of the "distributed coupling" model. In this model, the temperature dependence only arises from a temperature-dependent, quasi-static distribution of heme geometries that slowly evolves with respect to the timescale of CO-recombination<sup>1</sup> [84]. The recombination itself was found to be essentially barrierless in this model. However, potential energy barriers in the ligand escape were not considered.

In view of the mechanism that was established for *EcDos* [36], we set out to investigate the possibility that ligand escape energetics also contribute to the rebinding characteristics in CooA. In addition to temperature, protein dynamics can also be influenced by the viscosity of the solvent. Therefore, we performed glycerol-dependent

---

<sup>1</sup>In the "distributed coupling" model, the fundamental parameters which describe the heme conformational distribution in terms of out-of-plane positioning are calculated from the fitting parameters of the data. The model was first described in detail by Srajer *et al.* [91].

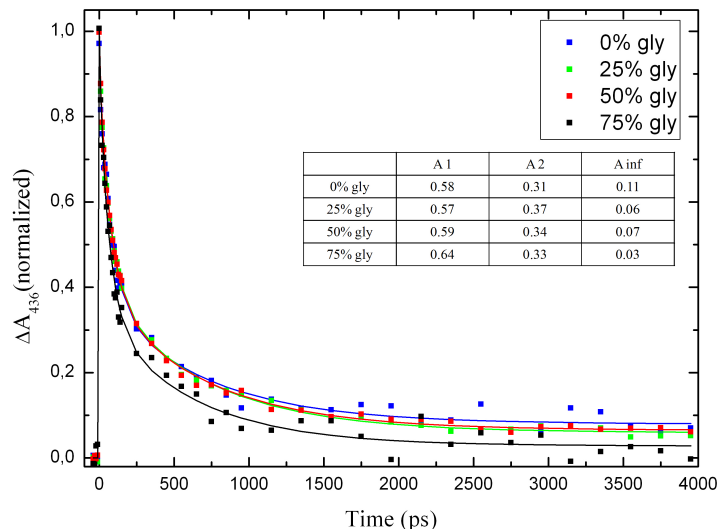


**Figure 3.6:** Glycerol dependence of CO-recombination in CooA at  $T=16^{\circ}\text{C}$  and 436 nm (maximum of induced absorption). CO kinetics can be well fitted with a sum of two exponentials ( $\sim 75$  ps (A1) and  $\sim 675$  ps (A2)) and a non-decaying constant component (Ainf). Amplitudes are shown in the legend.

experiments of CO-recombination to CooA at constant temperature ( $16^{\circ}\text{C}$ ) (Figure 3.6). It is observed that increasing concentrations of glycerol yield more efficient CO-recombination. In particular, this effect is quite substantial for 75% glycerol.

Qualitatively, this finding indicates that the CO rebinding kinetics are not influenced by the protein dynamics, but that the competing ligand escape reaction is. By contrast, the change of viscosity is not expected to change the steady-state thermal distribution of heme configurations. Altogether, these results indicate that ligand escape barriers should be taken into account in CooA.

Figure 3.7 shows the temperature-dependence kinetics of CO-rebinding at 436 nm. The data show a higher escape yield at higher temperatures. This is qualitatively similar to the results of Benabbas *et al.* for CooA from *Carboxydotherrmus hydrogenoformans* [84] and follows the same trend as reported for CO-recombination in *EcDos* [36]. However, due to the small CO escape yield in CooA, the absolute temperature effect within the accessible range is small and a quantitative analysis of the energetic barriers for this protein is therefore difficult. As an alternative, we investigated another system where the energetic barriers can be quantitatively determined. As shown in section 3.2, DNR is a suitable model since the percentages of CO-recombination and CO-escape out of the heme pocket at 4 ns are similar (at  $20^{\circ}\text{C}$ , 36% CO-escape is observed).

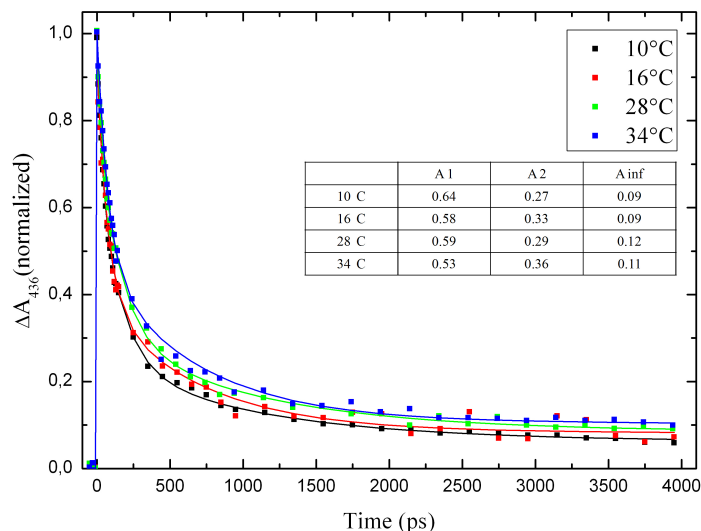


**Figure 3.7:** Temperature dependence of CO-recombination to CoxA. Higher temperatures result in less heme-CO recombination in the ps-ns timescale. CO kinetics can be well fitted with a sum of two exponentials ( $\sim 75$  ps (A1) and  $\sim 675$  ps (A2)) and a non-decaying constant component (Ainf). Amplitudes are shown in the legend.

Therefore, changes in the CO escape rate are expected to more strongly influence the overall kinetics.

Results of DNR-CO recombination measurements at various glycerol concentrations are shown in Figure 3.8. A large effect on the CO-escape yield is observed. For all glycerol concentrations, the kinetics could be fitted with a biexponential decay and a constant, with similar time constants  $\tau_1 \sim 100$  ps and  $\tau_2 \sim 1$  ns. In particular, the amplitude of the asymptotic (non-rebinding) phase decreases more than 3-fold upon addition of 75% glycerol. Again, this result is qualitatively similar as in CoxA (Figure 3.6), but there the absolute change is much smaller due to the lower overall escape yield. These results strongly support the idea of energetic barriers involved in the CO kinetics in DNR. As viscosity dependent measurements are difficult to directly interpret in terms of energetic barriers, for the purpose of a quantitative analysis, the temperature dependence of the CO-recombination to DNR has been studied.

Figure 3.10 shows the CO kinetics in DNR as a function of temperature. The upper limit of the investigated range was limited by protein precipitation above  $32^\circ\text{C}$ . The data were globally fitted with Glotaran software. The kinetics is shown at 442 nm, corresponding to the maximum of the  $\Delta A$  spectrum. We observe  $\sim 15\%$  change in the CO-escape for a temperature range of  $24^\circ\text{C}$ ; this is a larger temperature effect

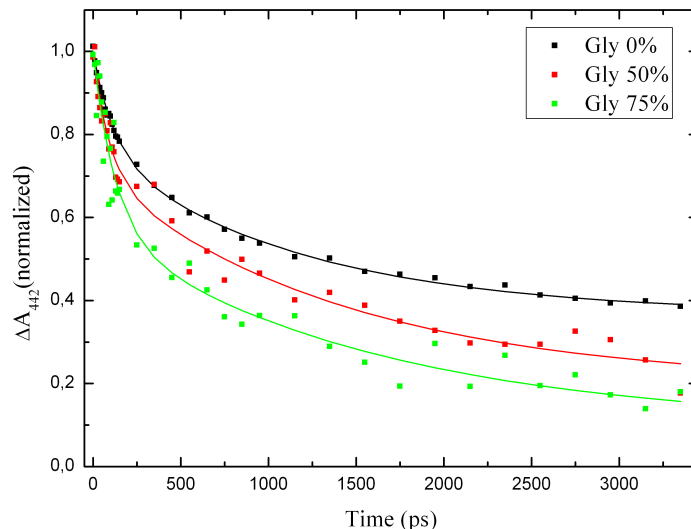


**Figure 3.8:** Glycerol dependence of CO-recombination in DNR. As in CooA, increasing concentrations of glycerol also result in larger CO recombination yields. However, the effect of glycerol concentrations on CO-escape is larger for DNR than for CooA. CO kinetics were well fitted with a sum of two exponentials ( $\sim 100$  ps and  $\sim 1$  ns) and a non-decaying constant component. Amplitudes as a function of glycerol concentration are plotted in Figure 3.9.

than what has been observed for CooA. This result is consistent with the suggestion that a barrier in the ligand escape pathway plays an important role in the temperature dependence.

All data can be fitted with curves of the following form:  $A_1 e^{-k_1 t} + A_2 e^{-k_2 t} + A_{inf}$ . Figure 3.11 shows the fit parameters  $k_1$ ,  $k_2$ , and  $A_{inf}$  as a function of the temperature. The relative amplitude  $A_1$  ( $\sim 30\%$ , not shown) and the rate  $k_1$  are virtually T-independent. We assign the rate  $k_1$  to a subpopulation ( $\alpha$  in Figure 3.12) in which efficient and barrierless CO-recombination occurs. For the remaining fraction  $\beta$  ( $\sim 70\%$ ), the normalized kinetics of the total dissociated state are expressed as:  $A e^{-k t} + (1 - A)$ , where  $A$  and  $k$  are the experimentally measured T-dependent relative amplitudes and rates, respectively. This fraction is analyzed in terms of the microscopic reaction model outlined at the bottom part of Figure 3.12. Here  $k_I$  represents the CO rebinding from the subpopulation  $\beta$  and  $k_{II}$  represents the rate of CO escaping the heme pocket (also from the subpopulation  $\beta$ ). In this model, the observables  $k$  and  $A$  relate to the microscopic rate constants  $k_I$  and  $k_{II}$  as  $k = k_I + k_{II}$  and  $A = k_I/k$ . Thus  $k_I$  and  $k_{II}$  can be retrieved as:

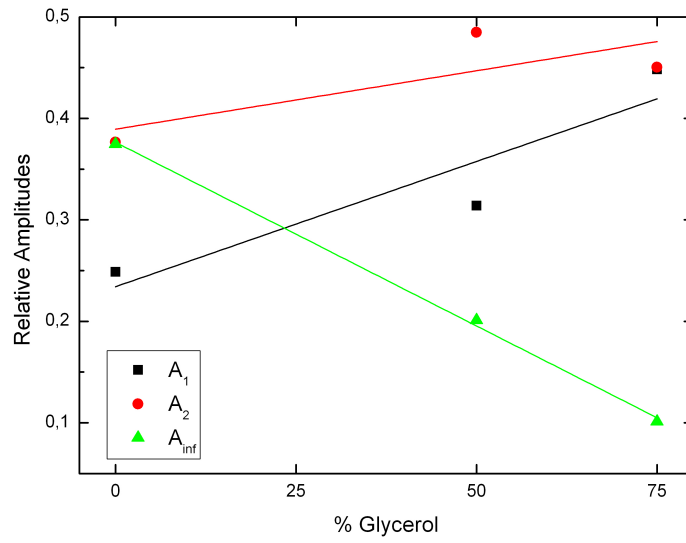


**Figure 3.9:** Relative amplitudes of CO recombination in DNR fitted to  $A_1e^{-k_1t} + A_2e^{-k_2t} + A_{inf}$  as a function of glycerol concentrations. The time constants are constant within experimental error. The lines are guides for the eye.

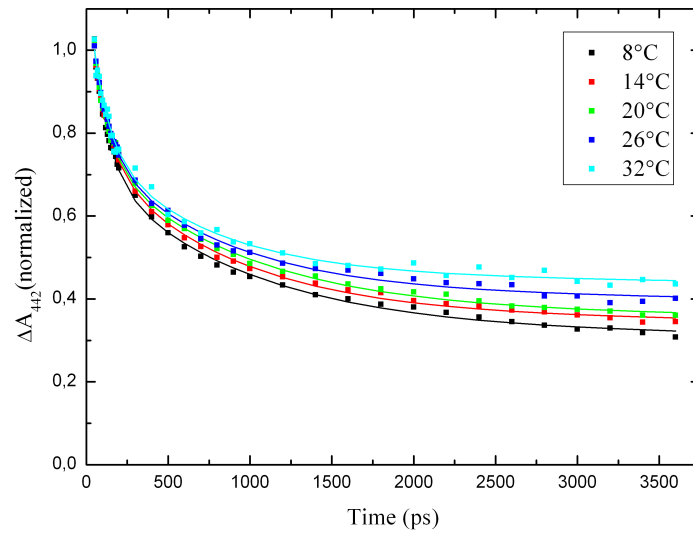


**Figure 3.10:** Temperature dependence for CO-DNR recombination. Increasing temperatures result in less CO-recombination to the heme. Solid lines are fits to a biexponential decay and a constant (rates and amplitudes shown in Figure 3.11).

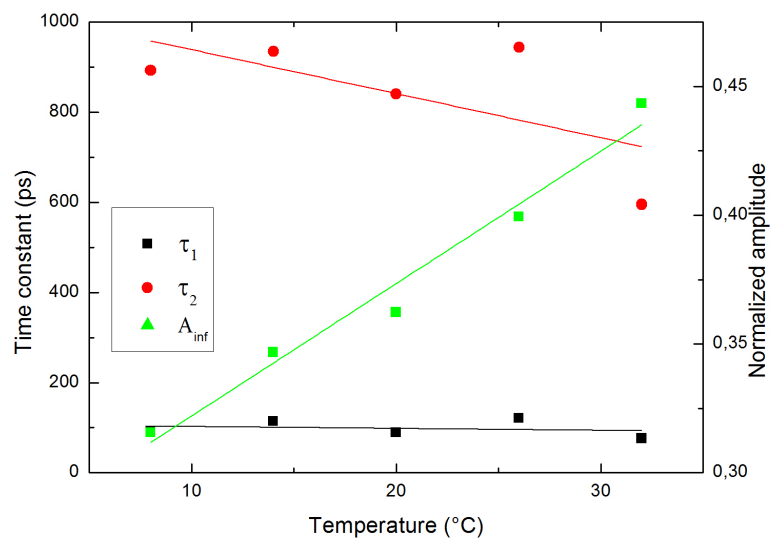


**Figure 3.11:** Time constants for CO-recombination (black and red) and normalized amplitude for CO escape (green) as a function of temperature for DNR.

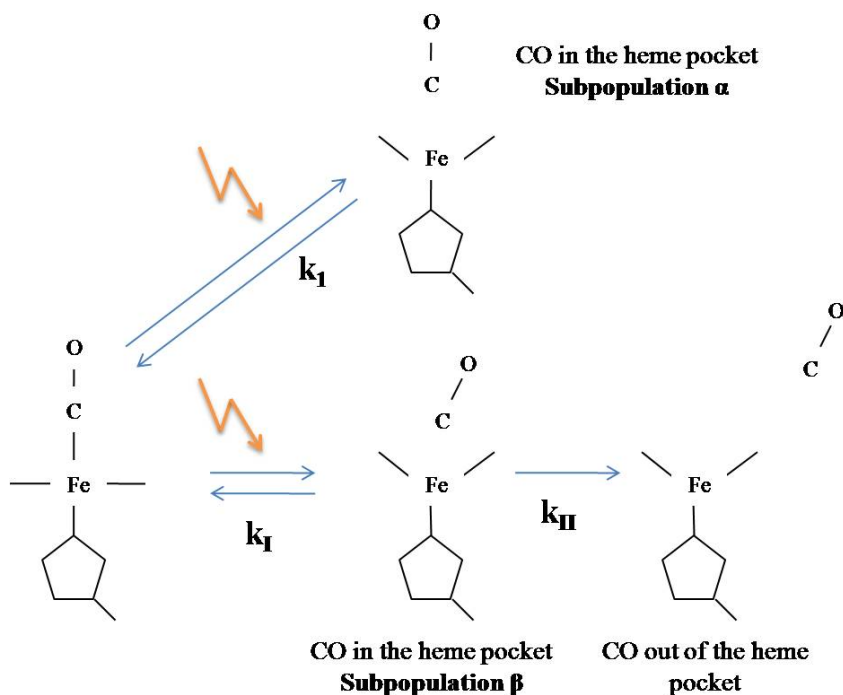


**Figure 3.12:** Scheme for the analysis of the T-dependent fraction of CO-recombination to DNR. In this model, two subpopulations with the CO close to the heme are considered, being populated (with different amplitudes) immediately upon CO dissociation. From the fitting of the data,  $k_1$  is found to be independent of temperature.

$$\begin{aligned}k_I &= Ak \\k_{II} &= (1 - A)k.\end{aligned}\tag{3.1}$$

The rates  $k_I$  and  $k_{II}$  were thus obtained for each temperature and plotted as a function of  $1/K_B T$  to determine the intrinsic activation barriers,  $E_{aI}$  and  $E_{aII}$ , using the Arrhenius equation:

$$\log\left(\frac{k_I}{k_0}\right) = -\frac{E_{aI}}{K_B T},\tag{3.2}$$

where  $E_{aI}$  is the activation energy for  $k_I$ ,  $K_B$  is the Boltzmann constant,  $T$  is the temperature and  $k_0$  is the intrinsic barrierless rate ( $E_{aII}$  is found with the analogous Arrhenius equation, for  $k_{II}$ ). Figure 3.13 shows that the barrier for CO recombination to the heme is 0 within experimental error ( $1 \pm 7$  meV). The enthalpy barrier for CO migration out of the heme pocket was found at  $71 \pm 15$  meV. These results for DNR are remarkably comparable with those of *EcDos* [36], where a barrierless CO-rebinding and a barrier for CO-escape ( $45 \pm 10$  meV) were found. The escape rate and the rebinding rate in both systems are of the same order of magnitude ( $\sim 1$  ns<sup>-1</sup>). In addition, in DNR there is a fraction ( $\alpha$ ) of extremely fast rebinding. In view of the escape rate deduced for the slower subpopulation  $\beta$ , this fast rebinding phase ( $k_1$ ) would compete very efficiently with CO-escape ( $k_{II}$ ).

Furthermore, these results strongly suggest that a similar mechanism occurs in *CooA*. Only, as explained above, the faster and overall rebinding in *CooA* yields a strongly reduced escape fraction and therefore a much lower absolute temperature effect.

Altogether, these studies show that in the proteins *EcDos*, *CooA* and DNR, CO-rebinding is essentially barrierless and that a barrier exists for CO-escape. Figure 3.14 represents a simple, one-dimensional reaction coordinate diagram, which highlights an activation barrier for the CO migration out of the heme pocket. As these three proteins are all 6-c heme-based gas sensor proteins, our observation raises the question whether these properties are a general feature for heme proteins or are specific for this class of 6-c proteins. For instance, do they also apply to 5-c ligand-binding heme proteins and to proteins that do not intrinsically bind external ligands? In the next two sections, we investigate these issues.

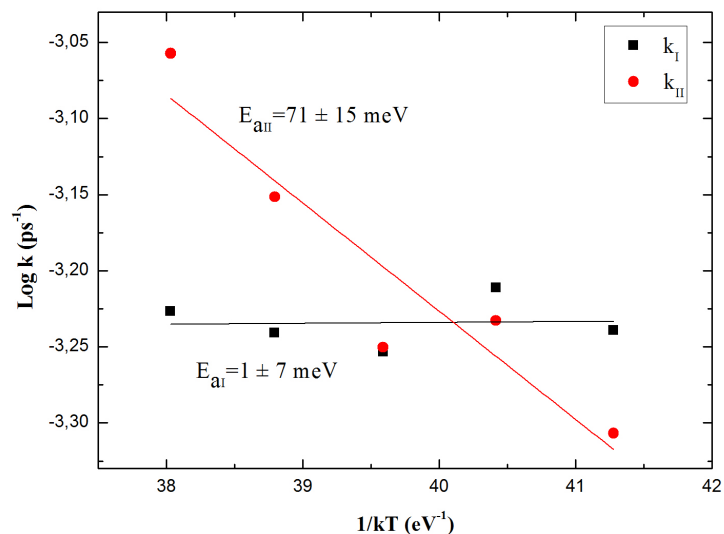


**Figure 3.13:** Arrhenius plot for DNR. The analysis of the temperature dependent data based upon the scheme in Figure 3.12 yields a barrierless (within the error) CO-recombination to the heme and a barrier of  $(71 \pm 15)$  meV for the CO-escape from the heme pocket.

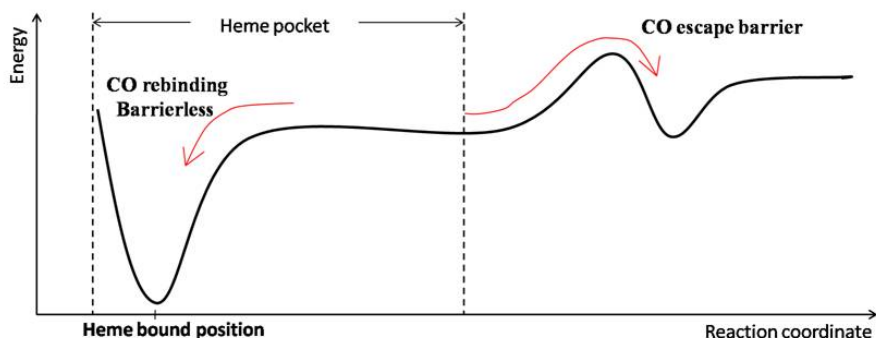


**Figure 3.14:** Simplified reaction coordinate diagram showing the extra-input of energy (in this case, thermal energy) required for the CO-escape from the heme pocket and migration towards the solvent.

### 3.3.2 5-c heme sensor proteins: small temperature dependence for DosT and Dos T Y169F

DosT from *Mycobacterium tuberculosis* is a heme-based sensor protein that is 5-coordinate in the absence of external ligands. It is one of the two signaling histidine kinases essential for the function of the transcriptional regulon DosR, which is chiefly responsible for encoding dormancy-related functions of *M. tuberculosis* [92, 93]. DosT contains a C-terminal enzymatic domain and two GAF domains, one of them containing

the heme cofactor and acting as sensor domain. In the ferrous ( $Fe^{2+}$ ), unliganded state, the heme in DosT is 5-coordinate like in Mb and FixL, but different from the 6-coordinate heme sensors CooA, DNR and *Ec*Dos. DosT can bind external ligands such as  $O_2$ , NO and CO and is active in the ferrous oxy form and inactive in all other forms. As a model for 5-c sensor proteins, here we study the isolated GAF A heme domain of DosT, referred to as DosT in the remainder of this section.

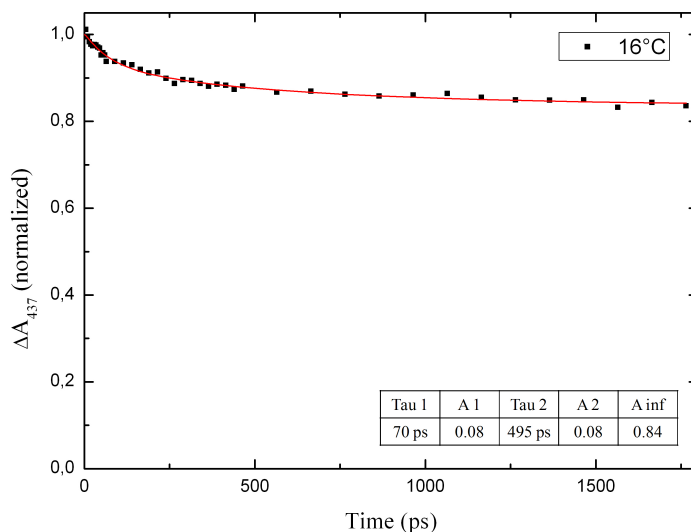


**Figure 3.15:** CO-recombination in WT DosT at  $16^\circ C$ . Data were well fitted with a sum of two exponentials and a non-decaying constant component. Rates and amplitudes are shown in the legend.

The recombination of CO to WT DosT is shown in Figure 3.15. CO rebinds on the ps to early ns timescale and in a highly multiexponential way [23]. This includes a very slow rebinding phase ( $> 4$  ns) that may reflect rebinding from a position away from the distal heme pocket. We have performed T-dependent measurements in the range  $12 - 28^\circ C$  and found the effect on the CO-kinetics to be very small (data not shown). This weak dependence on T, together with the fact that CO-escape from the heme pocket appears far more efficient than CO rebinding, makes this protein not favourable for a quantitative study of the potential activation barriers involved in the CO kinetics. On the other hand, the protein variant Y169F presents less polyphasic kinetics and  $\sim 50\%$  CO-escape at 2 ns ([23]; see Figure 3.16), making it a better suited model.

Figure 3.16 shows the CO recombination kinetics for Y169F DosT at 8 and  $28^\circ C$ .

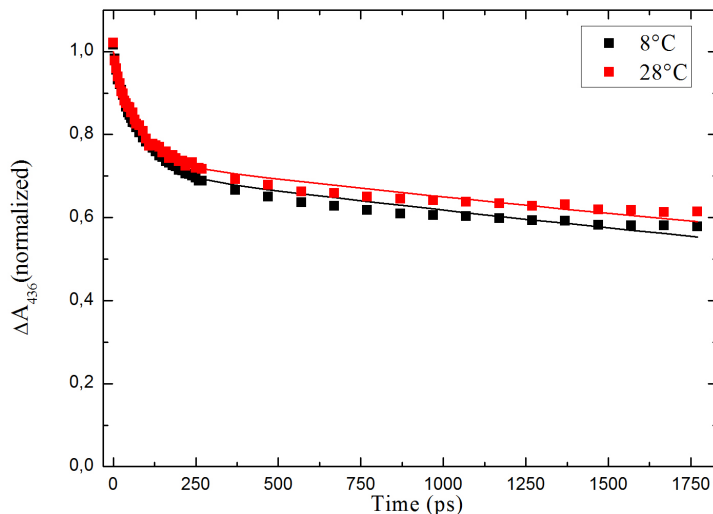


**Figure 3.16:** CO recombination for Y169F DosT at 8°C and 28°C. Solid lines are fits to the multiexponential decay (rates and amplitudes are described in the text and in Figure 3.17).

The temperature dependence of the CO kinetics appears small. This finding contrasts with results obtained for DNR and CooA (figures 3.7 and 3.10) and suggests that any energetic barriers for CO escape are lower in DosT Y169F. To quantify these results, the data were analyzed as follows. The data was globally fitted multiexponentially. Apart from a phase of  $< 5$  ps that was, again, attributed to heme photophysics and not considered further, two more decay phases were required, one with a time constants of  $\sim 70$  ps and a very slow ( $> 4$  ns) decay phase<sup>1</sup> (cf. Ref. [23]). Figure 3.17 shows the relative amplitudes for the two phases as well as the rate for the fastest phase as a function of temperature. These parameters are almost temperature independent.

To quantitatively estimate limits for the activation barriers, we analyzed these results in terms of the formalism of Eqn. 3.1, corresponding to the scheme of direct competition between ligand escape ( $k_{II}$ ) and ligand rebinding ( $k_I$ ) (Figure 3.12, bottom part). Here, we assume that the amplitude of the slow ( $> 4$  ns) phase corresponds to CO that has escaped from the heme pocket. Figure 3.18 shows the Arrhenius plots for Y169F DosT. Both ligand escape ( $E_{aII}$ ) and ligand rebinding ( $E_{aI}$ ) appear almost barrierless. In particular, we note that the escape barrier was found to be much smaller

<sup>1</sup>Because of the limited time window in our experiments, a precise time constant for this phase could not be determined. The amplitude of this phase corresponds to all decay phases with time constants  $> 4$  ns.

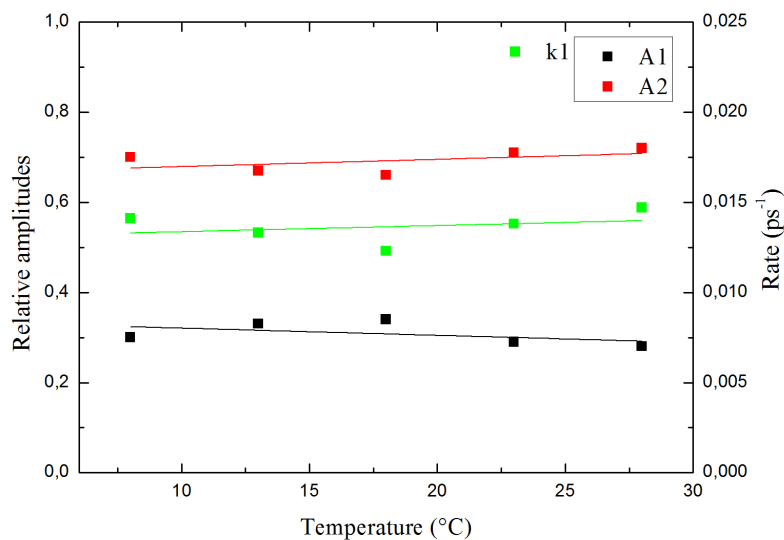


**Figure 3.17:** Normalized amplitudes for the two decay phases and the rate  $k_1$  of the CO recombination to Y169F DosT as a function of the temperature.

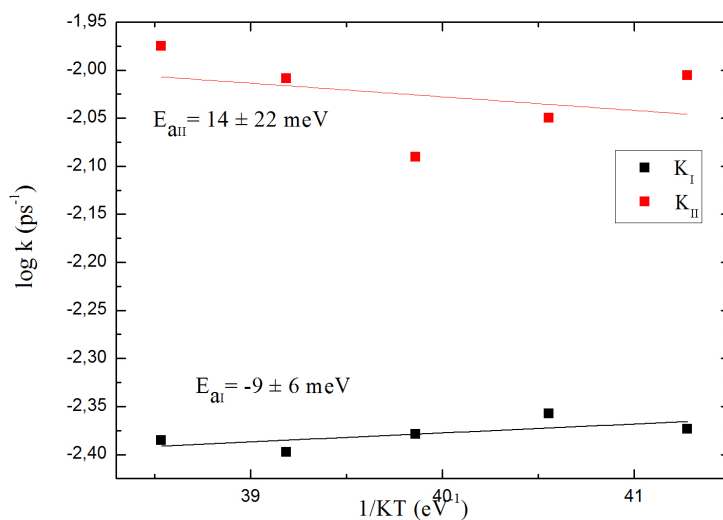


**Figure 3.18:** Arrhenius plots of Y169F DosT.

(< 35 meV) than in the 6-coordinate sensor protein DNR ( $71 \pm 15$  meV). As will be discussed in the final paragraph of this chapter, this difference may be related to the fact that in 5-c heme proteins the external ligand does not need to replace an internal

ligand.

### 3.3.3 Temperature dependence of CO-rebinding in cytochrome *c* variants

In this section, we report our study of the temperature effect of CO-rebinding in modified forms of cytochrome *c* (cyt *c*). Cyt *c* is a 6-coordinate electron transfer protein that is relatively rigid and stable. In native cyt *c*, the heme is coordinated by two internal residues, His-18 and Met-80, and cannot readily bind external ligands [94, 95]. However, substitution or chemical modification of the heme coordination residue Met-80 alters the protein so that it is able to bind CO [95, 96]. In this study, we focus on the cytochrome *c* mutants M80D and M80D/F82G and on carboxy-methylated cytochrome *c* from yeast. In M80D, CO recombination is *qualitatively* similar to CooA with more than 90% of dissociated CO rebinding to the heme within 4 ns, in a multiphasic way (see Figure 3.19). In the M80D/F82G mutant, the CO-escape yield is slightly larger than in M80D.

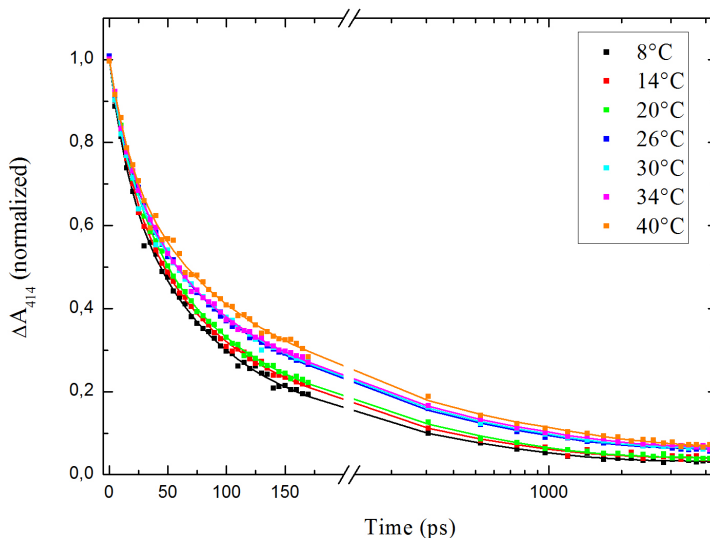


**Figure 3.19:** Temperature dependence of the CO recombination for the cyt *c* mutant M80D. Solid lines are fits to a three-exponential decay and a constant (rates remain virtually constant for all the temperatures and amplitudes are shown in Figure 3.20).

Figure 3.19 shows a weak temperature dependence of the CO recombination for M80D. The decay is highly multiexponential (at 20°C there are components of  $\sim 15$  ps ( $\sim 30\%$ ),  $\sim 100$  ps ( $\sim 50\%$ ) and  $\sim 550$  ps ( $\sim 15\%$ ), and a non-decaying phase of  $\sim$

5%), suggesting that the mechanism for CO-rebinding in M80D cyt *c* is more complex than in 6-coordinate proteins. Figure 3.20 shows the relative amplitudes of the phases as a function of temperature; the rates remain virtually constant (not shown). We observe that, qualitatively, the temperature dependence predominantly resides in the amplitude of the second phase ( $\sim 100$  ps) and in the non-decaying phase (that varies  $\sim 3$ -fold over the investigated temperature range). One possible interpretation is that three different configurations of dissociated CO are initially populated to equal extent at all temperatures, from which barrierless rebinding occurs in all cases, and that the population associated with the  $\sim 100$  ps phase allows CO-escape. However, this would imply that ligand escape competes more efficiently with the middle ( $\sim 100$  ps) phase of rebinding than with the slower ( $\sim 550$  ps) phase. Although it cannot be excluded, this seems unlikely. An alternative possibility would be a temperature-dependent population of the different CO-dissociated configurations.

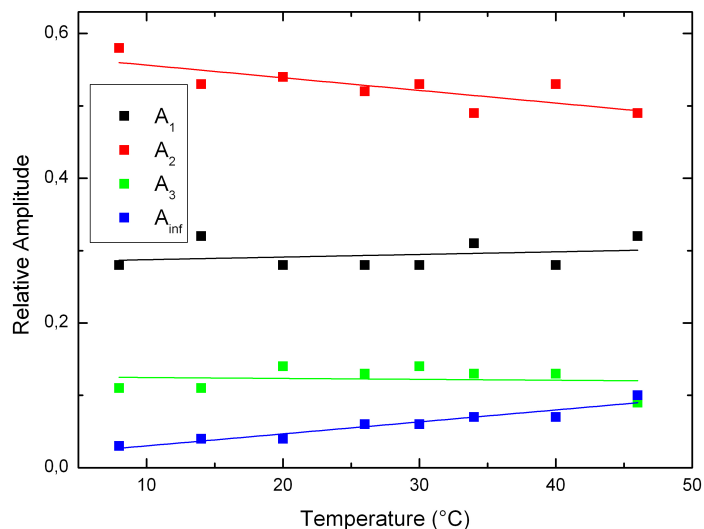


**Figure 3.20:** Relative amplitudes of CO-recombination to cyt *c* M80D as a function of temperature.

In the double mutant M80D/F82G, where presumably a large heme pocket is created, and where the yield of CO escape is higher [96], the T effect on CO-recombination is not substantially stronger than in M80D. We note that the pattern found in M80D of larger T effect at  $\sim 150$  ps than at 4 ns is also present in M80D/F82G, but even more accentuated (see Figure 3.21). Data was fitted with a sum of three exponentials (at  $20^\circ\text{C}$ ,  $\tau_1 \sim 15$  ps ( $\sim 25\%$ ),  $\tau_2 \sim 120$  ps ( $\sim 30\%$ ),  $\tau_3 \sim 850$  ps ( $\sim 30\%$ )) and a

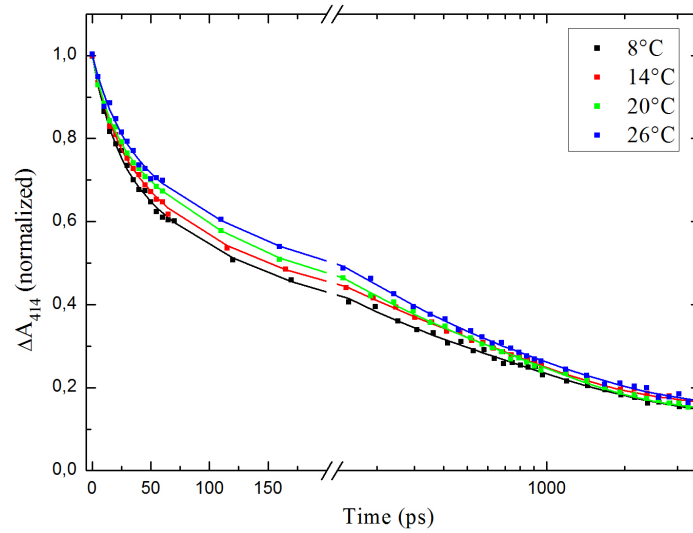


**Figure 3.21:** Temperature dependence of the CO recombination for the *cyt c* mutant M80D/F82G. Solid lines are fits of the multiexponential decay (as for M80D, rates remain virtually constant for all the temperatures while the amplitudes are shown in Figure 3.22).

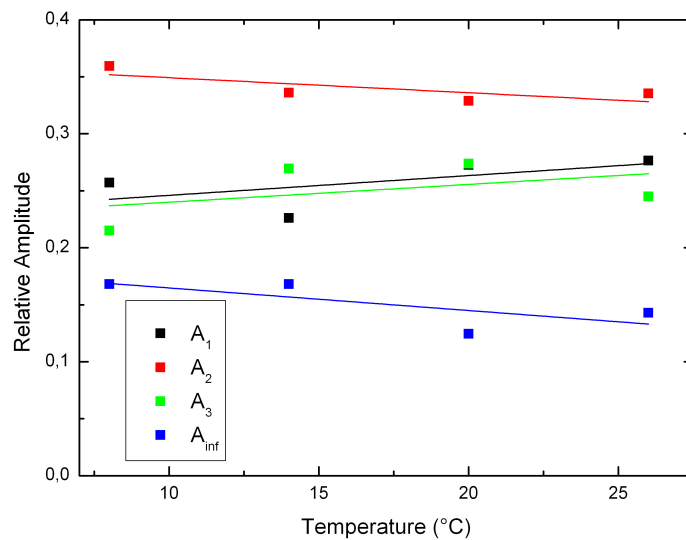


**Figure 3.22:** Relative amplitudes of CO-recombination to *cyt c* M80D/F82G.

non-decaying phase ( $\sim 15\%$ ). Figure 3.22 shows the relative amplitudes of the three phases and the non-decaying phase as a function of the temperature (the rates, as for M80D, also remain virtually constant -not shown).

Altogether, for both studied mutants, the combination of both weak and complex temperature dependence complicates a reliable analysis of the temperature effect. In the following, we will investigate a cytochrome *c* variant that is stable over a large temperature range.

Relatively high CO escape yields occur in carboxymethylated cytochrome *c* (CM-cyt *c*) [97]. Here, chemical modification leads to rupture of the Met-80-heme bond and further opens the protein [96], allowing CO binding to the heme iron. We observe that this complex is also stable within a remarkably large temperature range. CO-rebinding in CM-cyt *c* is strongly dependent on temperature in the range 10 – 75°C, as shown in Figure 3.23. At all temperatures, the data could be fitted with a sum of three exponentials (at 18°C,  $\tau_1 \sim 10$  ps ( $\sim 18\%$ ),  $\tau_2 \sim 90$  ps ( $\sim 45\%$ ),  $\tau_3 \sim 560$  ps ( $\sim 24\%$ )) and a non-decaying phase ( $\sim 13\%$ ). Figure 3.24 shows the relative amplitudes of each phase as a function of temperature, where three out of the four amplitudes substantially change with temperature (in particular  $A_{inf}$ , corresponding to the CO-escape, which changes  $\sim 3$ -fold between 10 and 75°, and  $A_2$ ), whereas the rates change little (not shown). Assuming that the fastest phase ( $\sim 10$  ps) corresponds to a distinct population that corresponds to direct barrierless recombination to the heme, the remaining four-parameter decay (comprising two exponential decay times and two independent amplitudes) was analysed in terms of the simple four rate-constant model represented in Figure 3.25.

In this model, after photodissociation of CO, two different configurational states are directly populated,  $Fe...CO^I$  and  $Fe...CO^{II}$ . In these states, CO stays within the heme pocket. From here, CO can rebind to the heme, with rates  $k_1$  and  $k_2$  from the states  $Fe...CO^I$  and  $Fe...CO^{II}$ , respectively. From the state  $Fe...CO^{II}$ , CO can also migrate to another intermediate state,  $Fe...CO^{III}$  with a rate  $k_3$ . CO molecules in the state  $Fe...CO^{III}$  can go back to the state  $Fe...CO^{II}$  with a rate  $k_4$  or can finally escape the heme vicinity and leave the protein (state  $Fe.....CO$ ). Eventually, on a time scale beyond our experiments, CO rebinds to the protein (bimolecular rebinding, not indicated in Figure 3.25).

The kinetic model represented in Figure 3.25, assuming similar heme extinction for all CO-dissociated states, allows fitting the data in terms of the rates  $k_1$  to  $k_5$  for each temperature. Then the Arrhenius plot yields the activation energy barriers corresponding to each rate (see Figure 3.26). Only the forward migration reactions ( $k_3$  and  $k_5$ ) are associated with significant positive activation barriers. The back reactions do not significantly depend on temperature ( $k_1$  and  $k_4$ ) or even display a small negative barrier ( $k_2$ ). The latter feature probably is not real and may reflect the fact that the

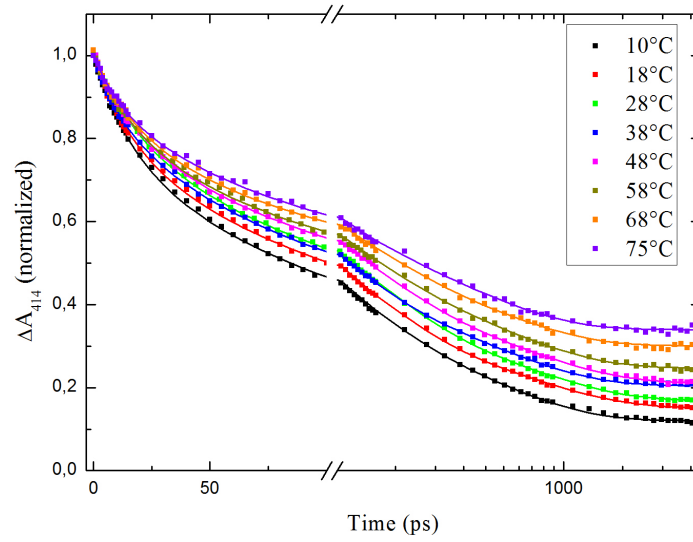


**Figure 3.23:** Temperature dependence of CO-recombination to carboxymethylated cytochrome *c*. Solid lines are fits to the three-exponential decay (see text and amplitudes shown in Figure 3.24).

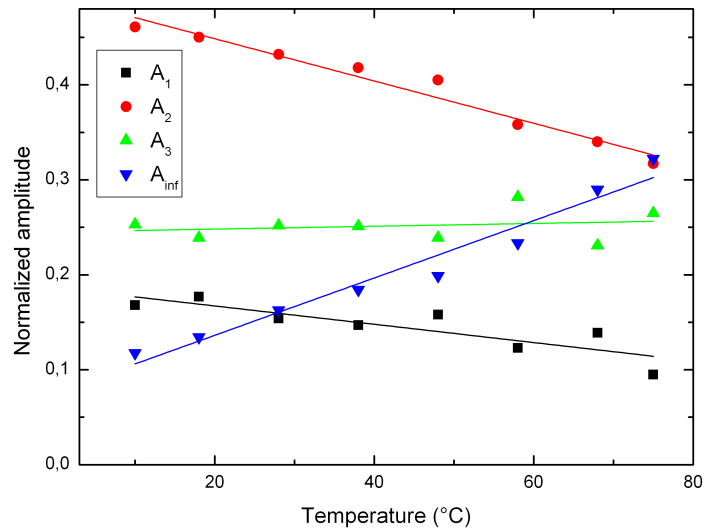


**Figure 3.24:** Relative amplitudes of the three-exponential fits of CO rebinding kinetics of Figure 3.23.

model is an oversimplification and that additional states (either directly populated dissociated states or intermediate migration states) also play a role. Thus, although

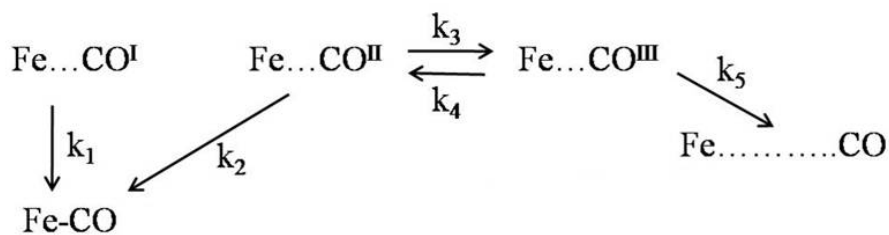


**Figure 3.25:** Suggested model for analysis of CO-rebinding temperature dependence in CM-cyt *c*. See text for details.

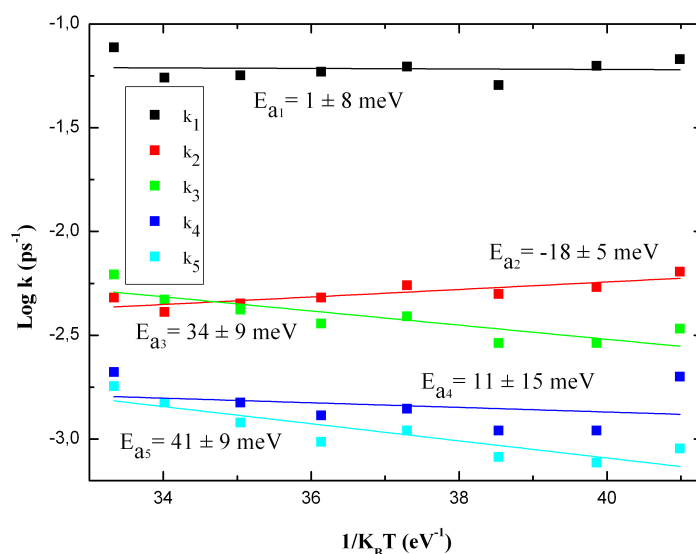


**Figure 3.26:** Arrhenius plot for CM-cyt *c* where  $k_3$  and  $k_5$  appear thermally activated after applying the model shown in Figure 3.25.

the CO kinetics is not governed by the same mechanism as in 6-c heme-based sensor proteins, the overall trend in this protein is the same: specifically the CO migration towards the exterior of the protein requires thermally activated protein motions. This finding is generally consistent with the fact that cyt *c* is a relatively rigid protein [98, 99], in agreement with its electron transfer function, and does not dispose of a natural ligand exchange channel.

In conclusion, in this chapter we have studied the CO rebinding kinetics in different heme proteins. We observed that a general mechanism applies to 6-c sensor proteins, where CO rebinding to the heme is barrierless and CO escape from the heme pocket is thermally activated. In the 5-c sensor protein DosT, the activation energies appear negligible, both for CO rebinding and for ligand escape. This indicates that ligand

migration through this protein requires less extensive motions of the protein backbone. Thus it appears that, for 6-c sensor proteins, the ligand replacement mechanism correlates with substantial ligand escape activation barriers. This observation leads us to suggest that the displaced residue directly or indirectly closes the heme pocket. Finally, whereas a more complex mechanism was needed to describe the CO dynamics in ligand-binding variants of the electron transfer protein cytochrome *c*, the general trend of thermally activated CO-escape is also observed, presumably reflecting the rigidity of the backbone.

## Chapter 4

# Ligand dynamics in the heme-domain of the *Ec*YddV sensor protein

Adaptation to environmental  $O_2$  availability is crucial for many organisms including mammals, where many processes are under  $O_2$  control [100]. YddV from *Escherichia coli* is a recently discovered globin-coupled heme-based oxygen sensor protein where binding of  $O_2$  to the reduced iron of the heme enhances diguanylate cyclase activity [101, 21]. Diguanylate cyclases are key second messenger signalling proteins in Gram-negative bacteria. In particular, YddV works in tandem with the well-studied heme sensor protein *Ec*Dos. The activity of YddV concerns the production of the signalling compound cyclic diguanylic acid (*c*-di-GMP), while *Ec*Dos degrades this compound [28, 102]. The complementary functions of these two enzymes are essential for maintenance of bacterial homeostasis, and have been related to bacterial cell-surface adhesiveness and biofilm formation [100, 103].

To date, many proteins have been identified that belong to the globin family. Among them are the oxygen-transport protein hemoglobin, the oxygen-storage protein myoglobin, neuroglobin, a high-affinity oxygen-transport protein, and cytoglobin, which transfers oxygen from arterial blood to the brain [104]. Globins are a well studied protein family of which many crystal structures have been determined, allowing insight into structure-function relationships [104]. Comparison of the amino acid sequences of different N-terminal globin sensor domains revealed in particular a 47% sequence similarity and 18% sequence identity with the globin-coupled aerotaxis transducer HemAT from *Bacillus subtilis* [21]. Differently from hemoglobin, neuroglobin, cytoglobin and

myoglobin, sensory globins are not thought to have a role in oxygen transport or storage.

Oxygen sensors typically contain a heme-binding sensor domain at the N-terminus of the protein and a C-terminal effector or catalytic domain [28]. Figure 4.1 shows the structure of the heme region of the globin sensor HemAT and the proposed heme environment of YddV based upon the structure of HemAT [101]. In the ferrous unliganded form, the heme is 5-coordinate. His98 corresponds to the heme axial ligand at the proximal side, Tyr43 is thought to play an important role in  $O_2$  recognition and the stability of the  $O_2$ -bound form, whereas Leu65 appears important for restricting water entry into the heme pocket, thus avoiding fast auto-oxidation of the protein [101].

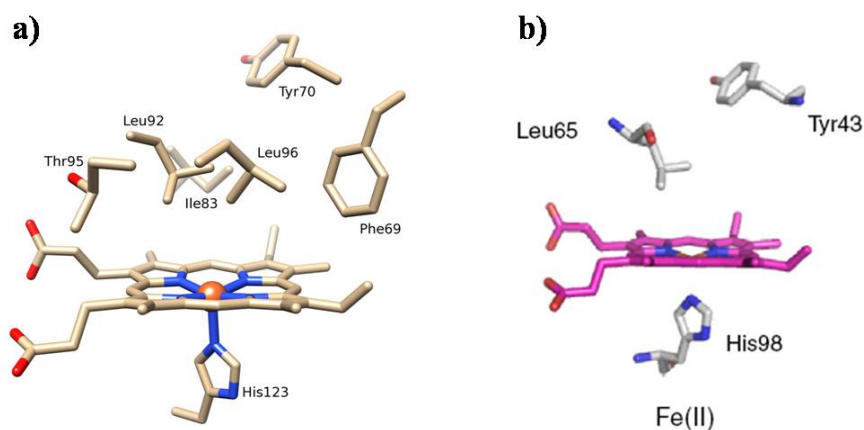


**Figure 4.1:** a) Heme environment of unliganded HemAT and b) Proposed heme environment of YddV based upon the structure of HemAT. His98 and Tyr43 residues have been suggested to play an important role, respectively, in the anchoring of the iron heme complex and binding of the  $O_2$  molecule at the heme distal binding site (figure taken from [101]).

We aim at getting insight into the role of specific residues in the heme distal pocket, as well as into the functional ligand interaction properties of the sensor. Therefore, ligand dynamics studies in the heme environment of WT YddV and mutant proteins of Leu65 and Tyr43 have been performed and the results are presented in this chapter. Isolated YddV heme sensor domains were provided through a collaboration with T. Shimizu's group (Tohoku University, Japan) and M. Martinkova (Charles University, Prague).

The steady state absorption spectra of the WT and mutant heme domains in different ligation states are shown in Figure 4.2. We observe a 6-coordinate heme in the forms Fe(II)-NO (c in the Figure 4.2), Fe(III)-NO (d) and Fe(II)-CO (e). A 5-coordinate heme was obtained for the Fe(II) complexes (a) (a mixture of 5-coordinate

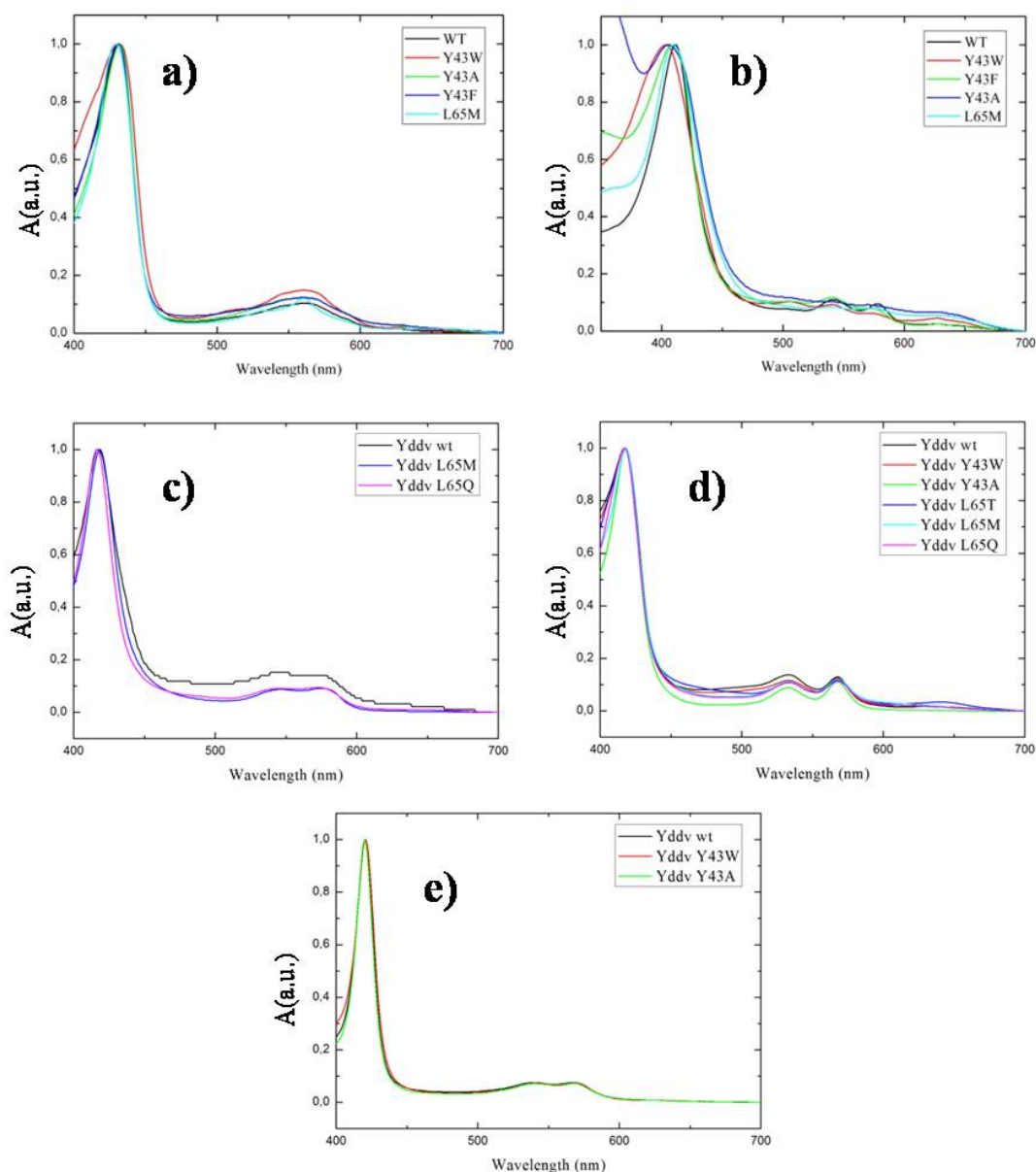


**Figure 4.2:** Steady state absorption spectra of YddV in the following forms: **a)** Fe(II), **b)** Fe(II)-O<sub>2</sub>, **c)** Fe(II)-NO, **d)** Fe(III)-NO and **e)** Fe(II)-CO.

and 6-coordinate heme was found for L65M, in agreement with [101]). Only WT YddV was obtained completely in the Fe(II)-O<sub>2</sub> form (**b**). In the Y43F mutant, a mixture between the Fe(II)-O<sub>2</sub> (~ 40%) and the oxidized (~ 60%) forms was obtained. The percentage of Fe(II)-O<sub>2</sub> was estimated by comparison of the spectrum of Y43F with the fully Fe(II)-O<sub>2</sub> spectrum of WT. For the mutants Y43W, Y43A and L65M, the Fe(II)-O<sub>2</sub> forms were obtained to some extent, but samples in this form underwent a degradation which impeded their use in our experiments.

We performed femtosecond visible transient absorption spectroscopy on heme domains of WT and mutant YddV in the  $O_2$ , NO (ferric and ferrous) and CO bound forms. In these experiments, the ligand is photodissociated and the spectral properties, the quantum yield (for  $O_2$ ) and the geminate rebinding kinetics (NO and CO) of the dissociated ligand are investigated.

## 4.1 Quantum Yield determination of $O_2$ dissociation

In other heme-based PAS and GAF domain-containing oxygen sensor proteins, the effective quantum yield (QY) of photodissociation of  $O_2$  from the heme was found to be very low [36, 23]. This feature has been assigned to partial, very fast ( $\sim 100$  fs) reformation of the heme- $O_2$  bond due to strain induced by the distal heme environment. Here we investigate if these properties also apply to the globin domain-containing  $O_2$  sensor protein YddV.

In these experiments we photodissociate the  $O_2$ -heme bond and determine the QY of the external ligand at  $\sim 10$  ps. At this timescale, it was found that the dissociation yield is very low in other heme-based sensor proteins such as FixL ( $\sim 5\%$ ), *EcDos* and DosT [46, 105], presumably due to the very fast ( $\sim 100$  fs) rebinding occurring even prior to doming of the heme [46], a process involving strain exerted by distal heme pocket residues [106]. We determined the effective yield at 10 ps because at this time, vibrational relaxation is nearly completed [107].

The quantum yield for WT YddV was estimated with MbCO as a reference (since the QY of MbCO photodissociation is 100%). The method described in [43] was applied, comparing the steady state difference spectra in the induced absorption band with the absorption-corrected transient spectra. Variation in the absorption of the MbCO and YddV samples at 560 nm, which is the center wavelength of the pump pulse, was also taken into account.

The QY is  $\sim 5\%$  for WT YddV (see Figure 4.3). This low QY implies that  $O_2$  is effectively trapped once it is bound to the heme. This finding is similar to that in various other sensor proteins (FixL, *EcDos*, DosT from *Mycobacterium tuberculosis* [23, 2]), indicating that it could be a general feature of heme-based sensor proteins.

The QY of the Y43F YddV mutant (see Figure 4.4) was determined taking into account that only 40% of the protein solution is in the  $O_2$ -form<sup>1</sup>. We estimate an  $O_2$  dissociation yield of  $40 \pm 10\%$  at 10 ps. This value is similar, within experimental error,

---

<sup>1</sup>To do this, we calculate the difference spectrum between the reduced form of Y43F (40%) and the  $O_2$ -form of WT (40%).

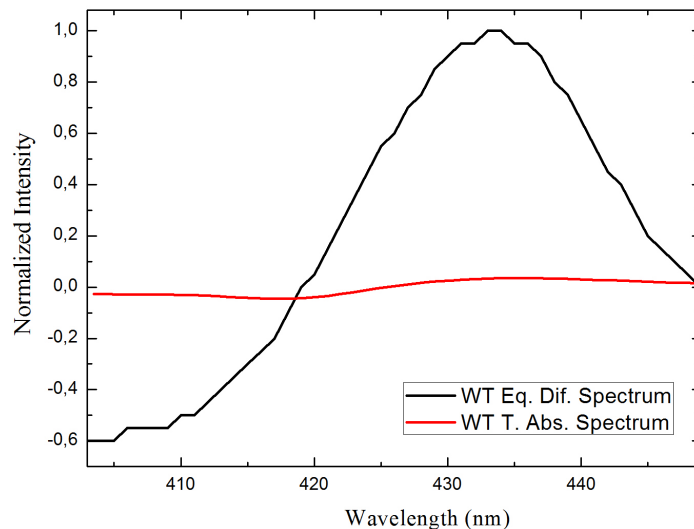


**Figure 4.3:** QY determination of  $O_2$  dissociation for WT YddV. The low yield of  $O_2$  dissociation at  $t = 10$  ps ( $\sim 5\%$ ), is similar to other  $O_2$  sensor proteins and may be due to the fast recombination of  $O_2$  within  $\sim 100$  fs.

to the  $\sim 30\%$  dissociation yield found in Mb- $O_2$  [43]. However, Y43F presents a much higher  $O_2$  dissociation yield in comparison to WT. It has been strongly suggested that a hydrogen bond between Tyr43 and the distal  $O_2$  is present, although no firm evidence exists [28]. As Phe is sterically similar to Tyr, but lacks the H-bonding possibility, our finding of a much larger QY of  $O_2$  dissociation in Y43F with respect to wild type supports this suggestion, as a hydrogen bond between Tyr43 and  $O_2$  may keep the  $O_2$  molecule in place once dissociated, impeding its escape out of the heme pocket.

The result that substitution of Tyr43 by Phe leads to much higher  $O_2$  escape may also explain the observed higher  $O_2$  off rate ( $k_{off}$ ) of the Y43F mutant [28]. Indeed, the change in  $k_{off}$  is in the same order of magnitude as the observed change in QY. Thus, a simple model in which the  $k_{off}$  is the product of the rate of thermal dissociation of the heme- $O_2$  bond and the probability of escape out of the heme pocket in the first few picoseconds may be sufficient to explain the mutation effect of the QY of  $O_2$  dissociation on the  $k_{off}$ .

Interestingly, the  $O_2$  association rate constant ( $k_{on}$ ) also increased in the Y43F mutant by about the same factor as  $k_{off}$  [28]. This indicates that Y43 also acts as a gate for  $O_2$  entry into the heme pocket. Altogether, in spite of the low  $O_2$  affinity of

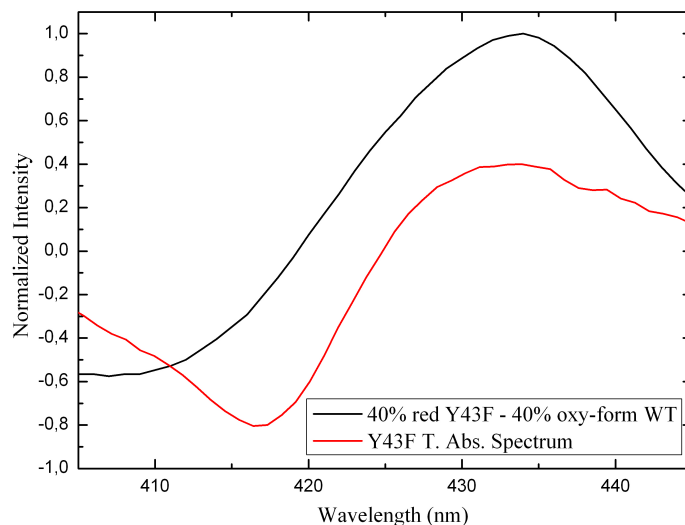


**Figure 4.4:** QY determination of  $O_2$  dissociation for Y43F.

WT YddV, its heme pocket acts as an efficient  $O_2$  trap, with Y43 largely responsible for this feature. By comparison, in FixL the residue Arg220, which makes an H-bond with the  $O_2$  molecule, has been suggested to play a similar role [46].

## 4.2 Fe(II)-NO, Fe(III)-NO and Fe(II)-CO forms of YddV

Nitric oxide (NO) is a poisonous gas which, at low concentrations, acts as signal transduction agent, for instance in the regulation of blood pressure [108] and in neurotransmission [109]. As many of these functions require the interaction of NO with heme proteins, understanding of the mechanism of NO binding to heme is crucial [110]. Furthermore, the dynamics of NO rebinding to the heme are often used as sensitive probe for the heme environment. Contrarily to CO, NO binds under an angle with the heme normal in the reduced form [111] and hence can adopt multiple configurations for heme binding and is very reactive to heme [112, 113]. NO binding kinetics potentially are sensitive to the competition between reactivity towards the heme and motions in the heme environment, especially on the sub-nanosecond timescale.

The most commonly investigated form is the Fe(II)-NO form. In YddV, this form could only be generated for the WT heme-domain and the L65M and L65Q mutants (see Figure 4.2 c). The observation that the Fe(II)-NO form could not be

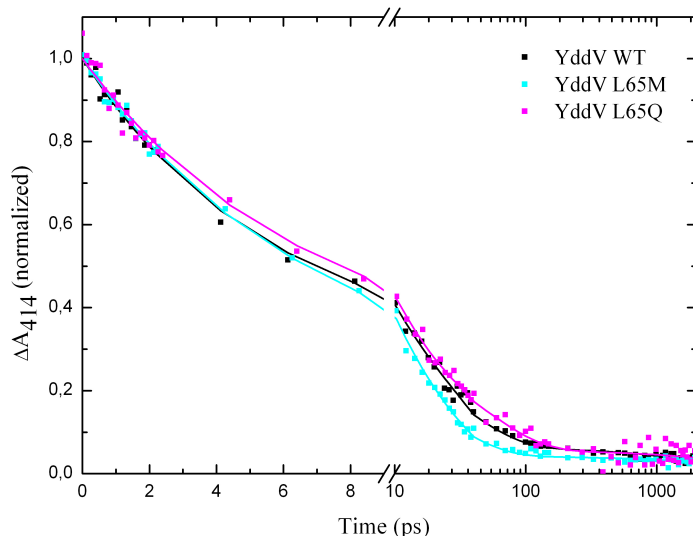


**Figure 4.5:** NO-recombination for YddV Fe(II)-NO: WT (black), L65M (blue) and L65Q (pink). Solid lines are fits to a biexponential decay (rates and amplitudes in the text).

obtained for substitutions of Y43 suggests that either the distal heme structure or the electrostatic environment implicating Y43 is important for NO binding to Fe(II), directly or indirectly.

In WT, NO rebinds almost completely in a biphasic manner, with time constants of  $\sim 5$  and  $\sim 30$  ps (remark the linear-logarithmic dual time base in Figure 4.5). The  $\sim 5$  ps phase is observed in many heme proteins and corresponds to barrierless ligand rebinding [16]. The presence of a second phase ( $\sim 40\%$  in WT) indicates that, to a limited extent, NO can move away from the heme. Figure 4.5 also shows a roughly similar NO recombination for WT and the mutants L65M and L65Q. The recombination for L65M is somewhat faster than for the other forms. This could be due to the fact that methionine (Met) is more flexible than leucine (Leu), allowing for NO to more rapidly sample conformations in the heme pocket and accommodate a configuration favoring NO recombination.

The NO oxidized form (Fe(III)-NO) has been successfully obtained for WT and several mutants under conditions where oxygen was carefully removed, as explained in section 6.9. The NO recombination in these complexes is slower and less efficient than for Fe(II)-NO [110]. This feature may be related to the fact that NO binds along to heme normal in the Fe(III)-NO form, whereas it binds under an angle with the heme normal in the Fe(II)-NO form [114]. Thus in the Fe(II)-NO form, in principle a cone

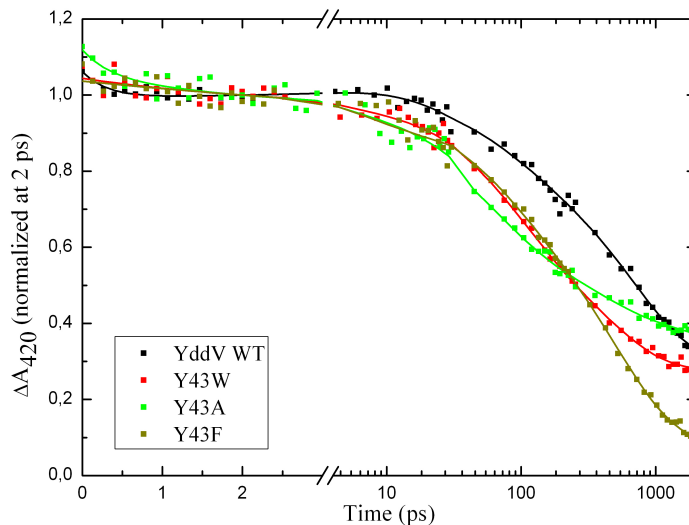


**Figure 4.6:** YddV Fe(III)-NO. NO-recombination for WT (black) and Y43 mutants: Y43W (red), Y43A (green) and Y43F (olive). WT presents the slowest recombination, suggesting that Tyr43 may strongly interact with the dissociated NO. Solid lines are fits to a biexponential decay and a constant (values shown in Table 4.1).

of favourable binding configurations exists, possible allowing for enhanced binding efficiency.

Figures 4.6 and 4.7 (note the linear-logarithmic double time scale) show the kinetics of the bleaching at 420 nm. Table 4.1 shows the results of fits in terms of exponential time decays and amplitudes for the NO recombination. The kinetics in the first picosecond presumably reflects heme photophysics.

The overall kinetics are generally in agreement with Fe(III)-NO recombination observed in many other heme proteins such as the ferric cytochrome *c*/cardiolipin complex [115] and ferric myoglobin [110], where NO is known to rebind to the ferric heme on the picosecond timescale and in a multiphasic way, allowing for a specific NO fraction to escape from the ferric heme. We can observe, in fact, that the escape yield of NO in Fe(III)-NO complexes is overall larger than in Fe(II)-NO complexes. The explanation for this observation may be that, since NO recombination is slower in Fe(III) than in Fe(II), in the former case the escape of NO competes more efficiently with NO rebinding [115].

Figure 4.6 shows that the Y43 mutants display faster NO recombination to the ferric iron in comparison to WT, indicating that the Tyr43 may strongly interact with the dissociated NO. A possible explanation for the slower recombination in WT

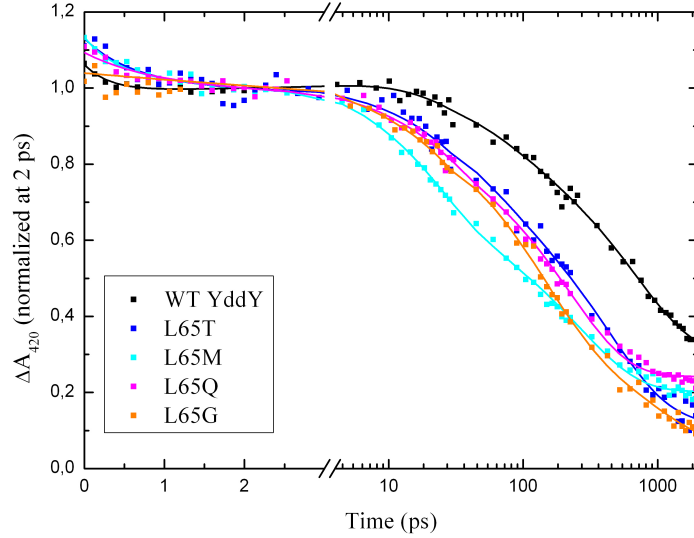


**Figure 4.7:** YddV Fe(III)-NO. NO-recombination for WT (black) and L65 mutants: L65T (dark blue), L65M (cyan), L65Q (magenta) and L65G (orange). WT presents the slowest recombination, suggesting that the physiological residu Leu65 may be required for Tyr43 to H-bond the NO. Solid lines are fits to a biexponential decay and a constant (values shown in Table 4.1).

Mutant	$\tau_1$ (ps)	$A_1$	$\tau_2$ (ps)	$A_2$	$A_\infty$
WT	68	0.2	680	0.5	0.3
Y43W	80	0.1	420	0.6	0.3
Y43A	60	0.3	500	0.3	0.4
Y43F	65	0.2	520	0.7	0.1
L65T	50	0.3	430	0.6	0.1
L65M	20	0.3	270	0.5	0.2
L65Q	20	0.2	220	0.5	0.2
L65G	130	0.6	860	0.3	0.1

**Table 4.1:** Fit results of NO recombination time constants and normalized amplitudes for Fe(III)-NO WT and mutants.

is that NO is H-bonded to the OH-group of this tyrosine residue and remains so after dissociation of the heme-NO bond. If heme-NO dissociation leads to significant displacement of NO, an H-bond would limit conformational freedom of NO and lead to less efficient positioning for recombination, especially in comparison with Y43F (Phe is sterically similar as Tyr, but cannot form an H-bond). For the Y43A mutant, the heme pocket is presumably less crowded due to the smaller size of the alanine residue. This would allow more conformational freedom for NO, which then could

more easily recombine and also escape the heme pocket, hence resulting in a more efficient rebinding, but less complete. All substitutions of L65 tested show faster and more efficient recombination than WT, with L65M presenting the fastest one (as for the Fe(II)-NO form). This suggests that leucine at position 65 might play a role in the formation of the H-bond of Y43 to NO.

Finally, we have studied the CO-recombination in WT and the two mutants Y43W and Y43A. The latter substitutions were chosen to alter possible steric constraints, as tryptophane (W) and alanine (A) are larger and smaller than tyrosine, respectively. No geminate recombination (up to 2 ns) of the CO is observed for the WT or the mutants (data not shown), indicating that the escape of the CO is complete and independent of the heme environment. These results are similar to many other 5-c heme proteins, where also virtually no CO-recombination yield is observed in the early picoseconds after photodissociation (*e.g.* FixL [116], myoglobin [105], soluble guanylate cyclase [90]).

In conclusion, in this chapter we have performed femtosecond transient absorption spectroscopy on WT YddV and W43 and L65 mutant proteins with the aim to obtain insight into the role of these two residues within the heme pocket and their importance in the ligand dynamics of the protein. In particular, determination of the  $O_2$  dissociation in WT and Y43F reveals the importance of the tyrosine residue at this position in stabilizing the Fe(II)- $O_2$  complex, since Y43F exhibits  $\sim 8$  times larger  $O_2$  dissociation than WT at 10 ps. No  $O_2$  recombination at long timescales (up to 2 ns) was observed, suggesting that once the switching mechanism is activated by  $O_2$  escape from the heme pocket, no recombination further occurs. As in FixL, the YddV heme pocket appears to act as efficient trap for  $O_2$ .

Fe(II)-NO complexes were observed in WT and the mutants L65M and L65Q. NO recombination takes place multiexponentially, with two time constants ( $\sim 5$  and  $\sim 30$  ps for WT). The faster NO recombination found for L65M compared to WT may reflect the property of methionine being more flexible than leucine, which would therefore allow NO to sample conformations where binding occurs easily. The Fe(III)-NO complex was obtained for WT and several Tyr43 and Leu65 mutants, showing in all cases a slower and less efficient NO recombination than in Fe(II)-NO. The recombination takes place on the picosecond timescale and is also multiexponential. All Y43 mutants exhibit a faster recombination than WT, suggesting an interaction of Y43 with the dissociated NO. In particular, the OH-group of the tyrosine residue may create an H-bond with NO, which would then impede NO to find a more efficient position to bind to the heme.

Overall, Tyr43 appears to have an opposing effect on the efficiency of  $O_2$  and NO escape from the heme pocket. This discrimination effect is supposedly related to the different timescale of recombination: for  $O_2$  this is thought to be on the  $\sim 100$  fs timescale, when  $O_2$  and heme have not yet been able to strongly change their configuration; for NO this is on the picosecond timescale, when NO has been able to move away. Thus, Tyr43 may help to avoid formation of the inactive NO-complex [28].

## Chapter 5

# Conclusions and Perspectives

In this work, we focused on two heme-based transcription factors and gas sensor proteins: CooA, a CO sensor, and DNR, which is activated by NO. For this study, we use biochemical methods and several advanced optical spectroscopic techniques with the aim to understand, on a molecular level, the functioning of the switching mechanism required for the activity of these proteins. More precisely, we wanted to get insight into the way how binding or dissociation of a small diatomic gas molecule to a heme sensor domain modifies the function of a distant DNA binding domain. This activation necessarily implies a rearrangement of the protein backbone occurring as a consequence of changes in heme coordination or its structural environment.

Protein binding to DNA was studied by steady-state fluorescence anisotropy and ultrafast fluorescence spectroscopy. These techniques allowed us to observe the specificity of the protein-DNA binding for CO activation and to determine the binding affinity. Our first characterizations of ligand-sensitivity of protein-DNA binding in the recently discovered sensor protein DNR are entirely in agreement with its proposed function as NO sensor. We performed FRET studies on CooA-CO-DNA. Here the target DNA was labeled with an appropriate fluorophore and acted as donor, with the heme acting as acceptor. Significant fluorescence quenching was observed in steady-state experiments. Time-resolved experiments showed that this was due to an overall acceleration of the fluorescence decay by protein binding. The determined rate of energy transfer allowed us to estimate the donor (DNA)-to-acceptor (heme) distance. This distance is in good agreement with values obtained from molecular modeling studies recently performed in our department.

We also used Circular Dichroism in order to qualitatively study the conformational changes occurring in CooA after binding of CO and after formation of the CooA-DNA

complex. We found that whereas CO binding to CooA changes the amplitude of the protein signal, DNA binding shifts its spectral position. Generally, the latter result is consistent with the idea that DNA binding reduces the structural heterogeneity in the heme-binding domain. These results open perspectives for time-resolved studies of the protein response to CO and DNA binding and release.

The conformational changes required for the activation of the protein are mainly triggered by changes in the coordination of the heme. Binding and/or dissociation of gas ligands eventually lead to activation or inactivation of an effector domain. Therefore, ligand dynamics was studied in the sensor domains of CooA and DNR using visible femtosecond spectroscopy, with the principal goal to obtain insight into primary processes of deactivation of these sensors. CO geminate recombination kinetics in CooA are very fast and efficient, indicating that the heme pocket of CooA acts as CO "trap". A similar mechanism has been observed for other heme-based sensor proteins, specifically with respect to their physiologically sensed ligand. Spectroscopic analysis of mutants of the distal, internal, heme residue proline (P2) revealed very similar CO-recombination kinetics, suggesting that P2 does not directly interact with CO. These findings are in agreement with the hypothesis that binding of CO to the heme in CooA induces a delocalized motion which displaces the proline residue far away from the heme pocket, thus serving as a bridge which stabilizes the protein in the active form.

Regarding DNR, the ligand dynamics in this protein have been studied in this work for the first time. Fast and efficient NO-recombination to the heme is observed. Studies on other NO-sensor proteins suggest that this is a general feature for this class of proteins. Interestingly, geminate recombination of CO occurs to  $\sim 60\%$ . This particular feature makes DNR highly suitable for investigating potential activation barriers involved in CO rebinding to the heme pocket and migration out of the heme pocket by determining the temperature dependence of the CO kinetics within this 6-coordinated heme-based sensor protein. From analysis of the data in terms of a microscopic reaction model at each temperature, we conclude that rebinding is barrierless and CO-escape thermally activated. Qualitatively, a similar pattern is detected for CooA. Along with previous observations for *EcDos*, these results suggest that this mechanism is a general feature governing the CO-ligand pathway in 6-coordinate heme-based sensor proteins.

Similar studies were performed on variants of the 5-coordinated heme-based sensor protein DosT, revealing much smaller barriers for ligand escape. This result indicates that the activation barriers in the 6-coordinate sensor proteins result from motions

coupled to the displaced internal residue.

For reasons of comparison, mutant and chemically modified ligand-binding forms of the electron transfer heme protein cytochrome *c* were used for the investigation of the barriers involved in the CO kinetics. These proteins present a very rigid backbone in agreement with their physiological activity. While more complex mechanisms were found to regulate the CO pathway, the overall pattern was found to be the same: CO recombination is barrierless, while CO escape requires thermal motions of the protein.

We also studied the globin-coupled oxygen-sensor YddV from *Escherichia coli*. In particular, the functional roles of the residues tyrosine 43 (Y43) and leucine 65 (L65) were investigated using site-specific mutant proteins. Transient absorption spectroscopy revealed that heme acts as trap for oxygen, consistent with the fact that YddV is an oxygen-sensor. We observed that the distal residue Y43 plays an important dynamic role in stabilizing bound oxygen and in discriminating between  $O_2$  and NO in order to avoid formation of the inactive YddV-NO-complex.

Our results open interesting and very varied perspectives for future studies. Different techniques for labeling of CooA with a fluorescent dye will be tested in order to be able to measure *intra-protein* FRET. Here the dye attached to the protein will act as FRET donor and the heme as acceptor. Such a system will hopefully allow to *quantitatively* characterize the conformational changes taking place upon CooA activation. Complimentary approaches include time-resolved circular dichroism spectroscopy.

Finally, concerning DNR, a study is currently being performed in our laboratory with the aim to determine the physiological residues that bind the heme cofactor in this sensor protein. Mutation of selected target amino acids, chosen based upon molecular modeling studies, may lead to the determination of the binding residues in the oxidized form.

In conclusion, in this work we have investigated and characterized the ligand dynamics in the heme-based sensor proteins CooA and DNR using biochemical approaches and advanced optical spectroscopy techniques. Our results represent important new insight into the switching mechanism which occurs in bacterial 6-c heme-based sensor proteins and which is essential for the adaptation and the survival of these organisms in rapidly changing environments.

# Chapter 6

## Materials and Methods

### 6.1 Bacterial strains

In this work, we have used the following bacterial strains from *Escherichia coli* (growth at 37°C/150 rpm in LB medium):

- XL1-Blue competent cells were used for transformation of the site-directed mutagenesis products. The genotype is the following: F' TN10 pro+B *lacI<sup>s</sup>*  $\Delta$  (*lasZ*) M15/*recA1 endA1 gyrA96(NaI<sup>r</sup>) thi hsdR17 (r<sub>k</sub> - m<sub>k</sub>) supE44 relA11a* [117].
- BL21(DE3) strains allow efficient expression of genes that are under control of a T7 promoter and lack both the *Ion* protease and the *ompT* outer membrane protease, which can degrade the protein during purification. This strain has the advantage of allowing for a high-level of expression and a straight forward induction. Target proteins are induced using isopropyl-1-thio- $\beta$ -D-galactopyranoside (IPTG). The genotype is the following: *E. coli* B *F<sup>-</sup> dcm ompT hsdS (r<sub>B</sub><sup>-</sup> - r<sub>B</sub><sup>-</sup>) gal  $\lambda$ (DE3)* [118].

### 6.2 Growth medium and antibiotics

*E. coli* strains were grown in LB medium (Luria Bertani: tryptone 10%, yeast extract 5%, NaCl 10%, pH 7.0)[119]. The medium was sterilized in an autoclave for 30 min at 120°C under 1 atm pressure. After cooling, specific antibiotics (previously sterilized by filtration on a 0.22  $\mu$ m membrane) were added. The plasmid containing the *coaA* gene presents resistance to ampicillin (final concentration of 100  $\mu$ g/ml), while the

*dnr*-containing vector is resistant to kanamycin (final concentration of 50  $\mu\text{g}/\text{ml}$ ). The stock solutions of these antibiotics are kept at  $-20^\circ\text{C}$  at stock concentrations of 100 mg/ml ampicillin and 50 mg/ml kanamycin.

## 6.3 Plasmids

### 6.3.1 *cooA* gene

The *cooA* gene has been cloned into the pQE 60 plasmid (Qiagen). In this plasmid, the 6x polyhistidine sequence is encoded at the C-terminal. pQE 60 also codes for the LacI protein and a beta lactamase gene that confers resistance to ampicillin. Figure 6.1 shows the map of this plasmid.

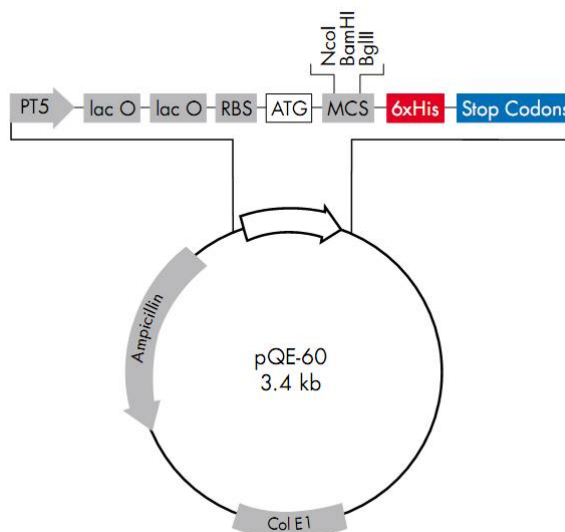


**Figure 6.1:** Map of the pQE 60 vector with the multi-cloning site, the restriction sites and the ampicillin resistance gene (Qiagen).

In order to perform the labelling of *CooA*, a co-transformation of BL21DE3 with pQE 60 and pEVOL (provided by The Scripps Research Institute, CA, USA [120]) is needed in order to express *CooA* (in pQE 60) and the transfer RNA (tRNA) of the non-natural *p*-azido-L-phenylalanine amino acid (in pEVOL). The pEVOL vector is resistant to chloramphenicol. Figure 6.2 shows the map of this plasmid.

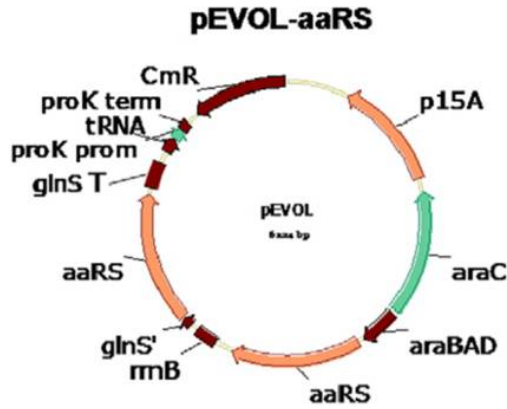


**Figure 6.2:** Map of the pEVOL vector with the the chloramphenicol resistance gene.

### 6.3.2 *dnr* gene

The pET-28a(+) vector (Novagen, see figure 6.3) has been used to clone the *dnr* gene. This vector codes for a 6x polyhistidine sequence (6x His-Tag) at the N-terminal, and contains a gene coding for the LacI protein (which regulates the lactose operon, allowing to use IPTG for the induction) and a gene which confers kanamycin resistance.

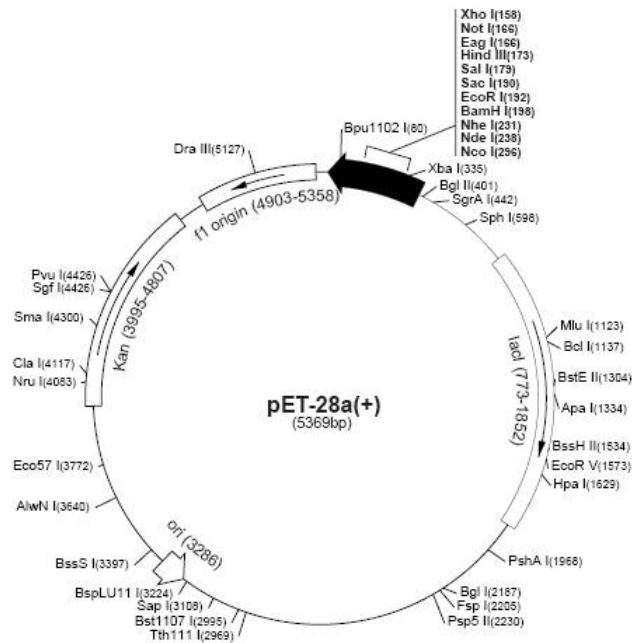


**Figure 6.3:** Map of the pET-28a(+) vector with the multi-cloning site, the restriction sites and the kanamycine resistance gene (Novagen).

### 6.3.3 *dosT* gene

The *dosT* gene has been cloned into pQE 80L (Qiagen, see figure 6.4). The 6x polyhistidine sequence is coded at the N-terminal. The beta lactamase gene confers resistance to ampicillin.

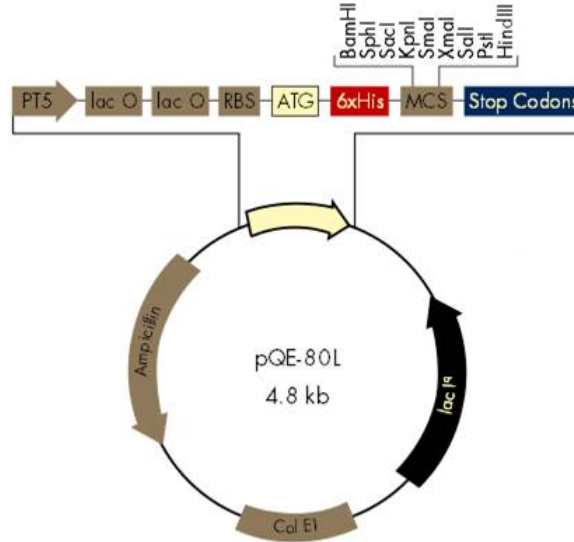


**Figure 6.4:** Map of the pQE 80L vector with the multi-cloning site, the restriction sites and the ampicillin resistance gene (Qiagen).

Tables 6.1 and 6.2 respectively show the informations for the plasmids used in this work and the oligonucleotide sequences used for site-directed mutagenesis.

**Table 6.1:** Plasmids and genes used in this project

Plasmid	Vector size	Gene name	Bacterial organism
pET-28a(+)	5369bp	<i>dnr</i>	<i>Pseudomonas aeruginosa</i>
pQE 60	3400bp	<i>coaA</i>	<i>Rhodospirillum rubrum</i>
pQE 80L	4800bp	<i>dosT</i>	<i>Mycobacterium tuberculosis</i>

Gene size	His-Tag position	Resistance marker
684bp	N-terminal	kanamycin
222bp	C-terminal	ampicillin
444bp	N-terminal	ampicillin

**Table 6.2:** Oligonucleotide sequences used for the site-directed mutagenesis

Name	Sequence	Size	$T_m$
CooA-P2H	5'-gga gaa att aac cat ggg tca tcc gcg ttt caa cat tgc taa-3'	42bp	62°C
CooA-P2H Reverse	5'-tta gca atg ttg aaa cgc gga tga ccc atg gtt aat ttc tcc-3'	42bp	62°C
CooA-P2L	5'-gaa ttc att aaa gag gag aaa tta acc atg ggt ata ccg cgt ttc aac attg-3'	52bp	61.9°C
CooA-P2L Reverse	5'-caa tgt tga aac gcg gta tac cca tgg tta att tct cct ctt taa tga aatc-3'	42bp	61.9°C
DNR-H139A	5'-ctg agc acc cgt ctg gct cag cgt atc gac ga-3'	32bp	64.4°C
DNR-H139A Reverse	5'-tcg tcg ata cgc tga gcc aga cgg gtg ctc ag-3'	342bp	64.4°C
DNR-H187A	5'-aca gct ggt tgc ggg tgc cct gtc tat cca gc-3'	32bp	78.5°C
DNR-H187A Reverse	5'-gct gga tag aca ggg cac ccg caa cca gct gt-3'	32bp	78.5°C
DNR-M88I	5'-acc ttc gca gag gct ata atg ttc atg gat acc c-3'	34bp	78°C
DNR-M88I Reverse	5'-ggg tat cca tga aca tta tag cct ctg cga agg t-3'	34bp	78°C
DNR-M89I	5'-aca cct tcg cag agg cta tga tat tca tgg ata cc-3'	35bp	78.1°C
DNR-M89I Reverse	5'-ggg atc cat gaa tat cat agc ctc tgc gaa ggt gt-3'	35bp	78.1°C
DNR-M91I	5'-gag gct atg atg ttc ata gat acc ccg aac tac gt-3'	35bp	78.1°C
DNR-M91I Reverse	5'-acg tag ttc ggg gta tct atg aac atc ata gcc tc-3'	35bp	78.1°C
DosTH-Y169F	5'-gtg ttt ggc aac cgt ttt ctg-3'	21bp	62°C
DosTH-Y169F Reverse	5'-gtg ttt ggc aac cgt ttt ctg-3'	21bp	62°C

### 6.3.4 Plasmid DNA purification

Bacterial cells containing the plasmid of interest were grown in LB medium (overnight at 37°C and with 150 rpm shaking) under the appropriate antibiotics selection. Typically, the culture volume used for plasmid purification was ~ 5 ml.

The gene coding for the protein of interest (CooA or DNR) served as template for site-directed mutagenesis. For the purification of the plasmid DNA, the NucleoSpin Plasmid commercial kit (Macherey-Nagel) was used. In this method, the pelleted

bacteria were resuspended in buffer A1 and the plasmid DNA was liberated from the *E. coli* host cells by alkaline lysis. Subsequently, the resulting lysate was neutralized allowing the DNA plasmid to renature and bind to a silica membrane. Non-desirable proteins, genomic DNA and cell debris were removed by several washing steps. Pure plasmid DNA was eluted by adding about 50  $\mu\text{l}$  of distilled  $H_2O$ . The purification process was performed by following the specifications of the kit manual [121] and the concentration of the pure plasmid was measured with a commercial spectrometer (Thermo Scientific *NanoDrop*\* 2000), typically giving values around 100-150 ng/ $\mu\text{l}$ .

## 6.4 DNA Gel electrophoresis

Agarose gel electrophoresis is a standard method used to separate and evaluate purified DNA fragments.

For 1.2% agarose gels, the agarose was melted in Tris-acetate-EDTA (TAE) buffer (1.2 g in 100 ml of TAE buffer) until a clear, transparent solution was achieved. After cooling to  $\sim 60^\circ\text{C}$ , ethidium bromide, a fluorescent dye that intercalates between bases of nucleic acids, was added to the gel (at a final concentration of 0.5  $\mu\text{g}/\text{ml}$ ) to allow visualization of DNA after UV excitation after electrophoresis. The melted solution was then poured into a casting tray where it solidified (30-45 min at room temperature). Typically, we use 1.2% agarose gels which have an efficient separation range of linear DNA molecules ranging from 0.4 to 6 kb [122], which is appropriate in our case.

DNA-sample was loaded onto the gel (usually about 10  $\mu\text{l}$ ) and a voltage of  $\leq 5$  V/cm was applied, in order to obtain good resolution. The DNA, which is negatively charged at neutral pH, migrated towards the anode of the system. Larger molecules migrate more slowly because they cannot pass through the pores of the gel as efficiently as smaller molecules. Therefore, superhelical circular, nicked circular and linear DNAs of the same molecular weight migrated at different rates through the gel. As a consequence, DNA that was not linearized with restriction enzymes, presented three different bands in the gel.

The size of linearized DNA molecules was compared to a standardized molecular marker of linear DNA fragments (1 kb DNA ladder, Fermentas).

## 6.5 Site-directed mutagenesis, *Dpn* I digestion and transformation

Site-directed mutagenesis was performed directly on the vector containing the target gene. The gene sequence was altered at a specific site, *e.g.* to modify a codon for an amino acid or to introduce a restriction site (as required for CooA labelling). Site-directed mutagenesis was performed using the QuickChange II Site-Directed Mutagenesis Kit from Stratagene (Agilent Technologies Division) that allows to obtain mutants with more than 80% efficiency in a single reaction with only a three-step procedure (one-day procedure). Figure 6.5 shows the mutagenesis procedure.

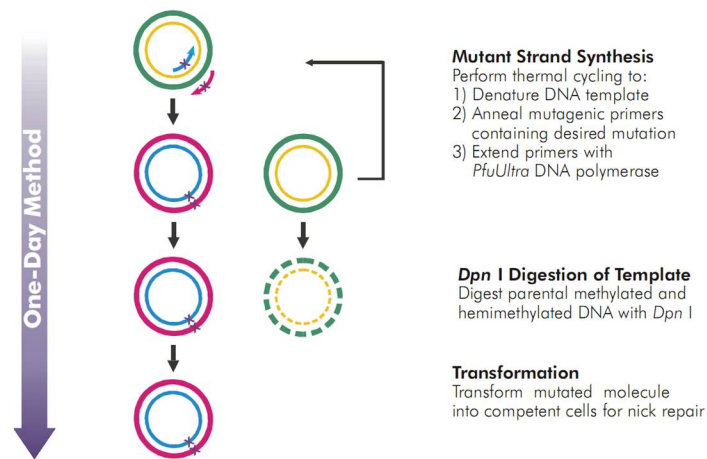


**Figure 6.5:** Overview of the QuickChange II Site-Directed Mutagenesis method, which consists of three steps: synthesis of complementary DNA strands containing the desired mutation, digestion of the parental DNA template and transformation [123].

The reaction was set up in a final volume of 50  $\mu$ l reaction buffer (10 mM KCl, 10 mM  $(NH_4)_2SO_4$ , 20 mM Tris-HCl, pH 8.0, 2mM  $MgSO_4$ , 0.1% Triton X-100 (volume/volume), 0.1% BS) which contained 50 ng of circular plasmid DNA, 1  $\mu$ l of dNTP mix, 125 ng of each primer (#1 and #2) and 1  $\mu$ l of *Pfu Ultra* high fidelity DNA polymerase) [6].

18 cycles of Polymerase Chain reactions (PCR) were performed:

- First cycle: Denaturation at 95°C during 30 seconds.
- Cycles 2-18: At each cycle, these three steps are repeated: Denaturation at 95°C during 30 seconds + hybridization at 55°C during 30 seconds + elongation at 68°C during 10 minutes.

Subsequently, the PCR product was treated with *Dpn* I endonuclease; a restriction enzyme specific for methylated and hemimethylated DNA. It is used to digest the parental, non-mutated DNA template. 1  $\mu$ l *Dpn* I was added directly to the amplification reaction, which was then incubated at 37°C for 1 hour. A DNA gel electrophoresis was performed to control the quality of the mutagenesis product. If acceptable results were obtained, the nicked vector DNA containing the desired mutation was then transformed into *E. coli* XL1-Blue competent cells.

For the transformation, 1  $\mu$ l of the *Dpn* I-treated DNA was added to 50  $\mu$ l aliquots of XL1-Blue competent cells and then incubated on ice for 30 min. A thermal shock (45 seconds at 42°C followed by a 2 min. incubation on ice) was performed to facilitate the entry of the plasmid DNA into the cell. After purification of the plasmid, it was sent to sequencing (Beckman Coulter Genomics) for verification of the introduced mutation before transformation into *E. coli* BL21(DE3) cells and expression of the mutated protein.

## 6.6 Protein expression and extraction

For the expression of CooA and DNR, an isolated bacterial colony was used as inoculum in 10 ml of LB, containing either 100  $\mu$ g/ml of ampicillin (in the case of CooA) or 50  $\mu$ g/ml of kanamycin (in the case of DNR) and incubated overnight at 37°C at 150 rpm agitation. This pre-culture was used as inoculum for the cell culture in 1.5 l of LB medium. Cultures were grown at 37°C and 150 rpm until they reached the exponential growth phase which corresponds to an optical density of  $OD_{600} = 0.5 - 0.7$ . At this point, the induction was performed by addition of IPTG (final concentration of 1 mM). The culture was grown in the incubator overnight at the same conditions as before, and the next day, the cells were recovered by centrifugation at 5000 rpm (rotor JLA-9.1000, Beckman) during 20 minutes at 4°C.

For protein extraction, the cell pellet was resuspended in lysis buffer (300 mM NaCl, 50 mM  $NaH_2PO_4$ , pH 8.0, DNase 5  $\mu$ g/ml, lysozyme 1 mg/ml). The cell lysate was sonicated 3 times during 45 seconds at a power of 70%, with a pause of about 15 seconds after each cycle (the lysate has to be kept in ice throughout the sonication to avoid overheating of the solution and denaturation). After sonication, the lysate was centrifuged at 10000 rpm (rotor JA-17, Beckman) for 1 hour at 4°C to separate the soluble fraction, containing our protein of interest, from the membrane fraction.

## 6.7 Purification of proteins

Protein purification was performed using immobilized metal ion affinity chromatography (IMAC), with a dry silica-based resin precharged with  $Ni^{2+}$  ions. Binding of the protein to the column is based on the interaction between the 6x polyhistidine tag of the protein and the immobilized ions [124].

Figure 6.6 illustrates the mechanism of binding of the protein to the column. The  $Ni^{2+}$  molecule has 6 coordination sites, 5 of them being occupied by the metal chelator tris-carboxymethyl ethylene diamine (TED). The sixth coordination site is available for protein binding. Compared to other chelating groups with less bonds to the  $Ni^{2+}$  ion, TED minimizes metal loss during the purification and also increases the specificity of the binding, resulting in very pure protein samples upon elution.

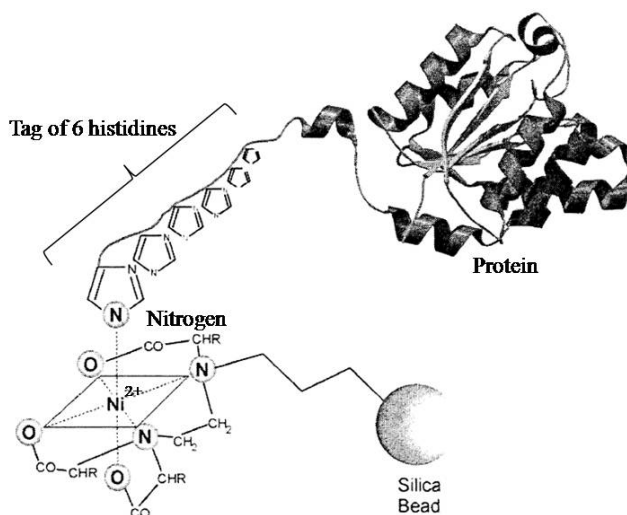


**Figure 6.6:** Schematic illustration of the binding of the 6x polyhistidine-tagged protein to the Protino Ni-TED column (Macherey-Nagel). One histidine residue of the 6x His-tagged protein binds to the resin [124].

In this purification method, the column was first equilibrated with Native Binding Buffer (NBB)(50 mM  $NaH_2PO_4$ , 300 mM NaCl, pH 8.0). Then the supernatant was loaded and the 6x His-tagged protein bound to the column. Since both CoxA and DNR contain a colored heme group, the resin became reddish when it was saturated with the protein. Virtually no contaminating proteins can bind and, therefore, stringent washing procedures are generally not necessary. However, before elution of the desired protein, the column was washed with NBB+20 mM imidazol to elute other molecules which may have been bound to  $Ni^{2+}$ . The Native Elution Buffer (NEB) contained 250 mM imidazol (50 mM  $NaH_2PO_4$ , 300 mM NaCl, 250mM imidazol, pH 8.0) in

order to recover even the most strongly bound proteins. Imidazol was then removed by passing the eluted protein through a Sephadex G-25 gel filtration column (Bio-Rad). This last step is crucial, since even the presence of small quantities of imidazol in solution may have an effect on ligand binding to the heme (imidazol can bind to the heme, therefore preventing external ligands to bind).

## 6.8 Protein gel electrophoresis (SDS-PAGE)

One-dimensional SDS gel electrophoresis of proteins was performed in order to verify the purification quality. In denaturing polyacrylamide gel electrophoresis (SDS-PAGE), separation of proteins is obtained according to their molecular mass. Proteins move through the gel matrix towards the anode in response to an electric field [125]. Sodium dodecyl sulfate (SDS) is an anionic detergent, which binds proportionally to the proteins, providing them with a negative electric charge, largely superior to the one intrinsic to the protein. Furthermore, SDS reduces the protein disulphide bonds, thus denaturing the proteins and preventing their refolding. This assures that proteins migrate only as a function of their molecular mass.

For SDS-PAGE, a Mini-Protean electrophoresis system (Bio-Rad) was used. We used a 10% polyacrylamide gel in agreement with the molecular mass of CoxA (about 24 kDa par monomer) and DNR (about 25.8 kDa par monomer) [126]. The samples were charged in a loading buffer containing 4% SDS, 20% glycerol, 125 mM Tris-HCl, pH 6.8 and 0.004% Bromphenol Blue. 2%  $\beta$ -mercaptoethanol was added extemporaneously. The denaturation of the proteins was completed by heating the sample at 100°C during 3 min.

After migration, Coomassie Brilliant Blue was used to stain the proteins in the polyacrylamide gel. The gel was stained during 1 hour (under agitation) in 10% acetic acid, 50% ethanol and 0.025% Coomassie Brilliant Blue and destained (1 hour, under agitation) in 5% acetic acid and 30% ethanol in order to visualize the protein bands.

## 6.9 Steady-state absorption and protein concentration

Steady-state spectra were recorded using a Shimadzu UV-Visible 1601 spectrophotometer. Figures 6.7 and 6.8 respectively show the steady-state absorption for CoxA and DNR in different states. Two main regions are apparent: the Soret region with a main peak and the  $\alpha$ -region with two smaller peaks. The  $\alpha$ -region is very sensitive to

the structure of the heme and is often used as a marker of the heme's oxidation and coordination state. In particular, the two peaks in the  $\alpha$ -band region become sharper in the reduced form when compared to the oxidized form (see Figure 6.7). In the Soret region, one main peak is present at  $\sim 424$  nm for the oxidized form. In the reduced and CO-form, the absorption becomes higher (for the same concentration) and slightly shifts to the red. Figures 6.7 and 6.8 also show absorption peaks for the oxidized form at 280 nm, which predominantly correspond to the absorption of aromatic residues (mostly tryptophans and tyrosines) in the protein backbones. The 280 nm peak cannot be observed in the reduced forms (including reduced ligand-bound forms) because of absorption of the excess dithionite (max.  $\sim 310$  nm) reductant used.

The Beer-Lambert Law relates the optical density ( $OD_\lambda$ ) to the concentration as [127]:

$$OD_\lambda = \varepsilon_\lambda l C, \quad (6.1)$$

where the optical density is a dimensionless quantity, the concentration  $C$  is given in units of molarity and  $l$  is the optical path length (thickness of the cell), in our case 0.1 cm.  $\varepsilon_\lambda$  is the molar extinction coefficient at a particular wavelength [ $M^{-1}cm^{-1}$ ].

Therefore, from the spectra, the CooA heme concentration (using the Soret peak in the oxidized form of the protein;  $\varepsilon_{424} = 105 \text{ mM}^{-1}cm^{-1}$  [128]) and the DNR protein concentration in the apo-form<sup>1</sup> (using the peak absorption at 280 nm;  $\varepsilon_{280}=10 \text{ mM}^{-1}cm^{-1}$  [126]) could be calculated using equation 6.1.

The DNR protein concentration was also measured with the Thermo Scientific *NanoDrop*\* 2000. The NanoDrop spectrophotometer needs only 2  $\mu l$  of purified protein (in contrast to the Shimadzu spectrometer, where a minimum sample volume of  $\sim 120 \mu l$  is required) to provide a reliable measure. Values from the NanoDrop have been corroborated by the bicinchoninic acid (BCA) protein assay, obtaining very similar values in the two cases.

The BCA method [129] is based on the chelation of copper with proteins in an alkaline environment (pH higher than 7.0) which results in the reduction of  $Cu^{2+}$  to  $Cu^{1+}$ . BCA reacts with the reduced copper cation (2 molecules of BCA bind to 1 copper cation), giving the BCA/copper complex an intense purple color which exhibits a strong absorbance at 570 nm that is linearly proportional to the protein concentration (absorption of the heme at this wavelength can be neglected in this

---

<sup>1</sup>No heme is present after purification of the DNR. Hemin (heme B), was added to the protein as explained in section 6.10.

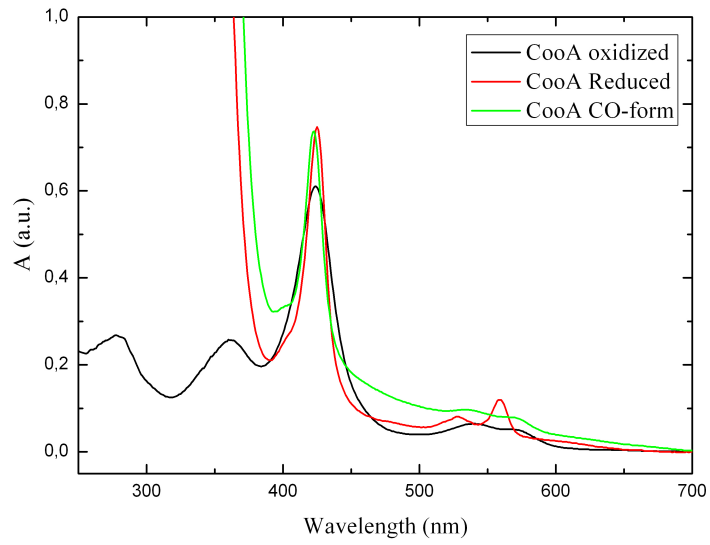


**Figure 6.7:** Steady-state absorption for the three forms of CooA: oxidized, reduced and CO-form.

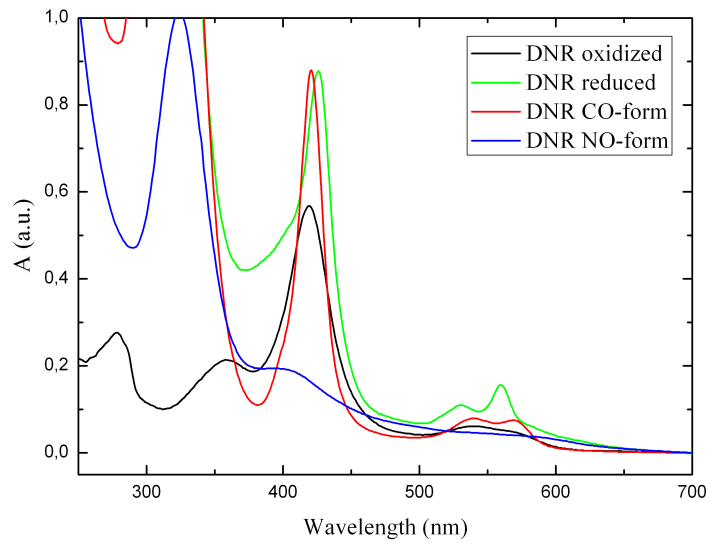


**Figure 6.8:** Steady-state absorption for the three non-active forms of DNR: oxidized, reduced and CO-form and for the active NO-form.

experiment due to the large excess of BCA).

For a standard curve, a range of dilutions of Bovine serum albumin ( $C_{stock} = 1$

mg/ml) were made and the absorbance for each known dilution was measured. The absorbance of the protein of interest was also measured under the same experimental conditions. Therefore, the concentration of unknown samples could be determined by interpolation from the standard curve. Figure 6.9 shows the standard curve obtained in our laboratory (using a microplate reader from Bio-Rad). Table 6.3 exhibits comparable values for the protein concentration (CooA WT and mutant; ThyX WT from the micro-organism *Thermotoga maritima*) using both methods, indicating that the NanoDrop gives an accurate lecture.

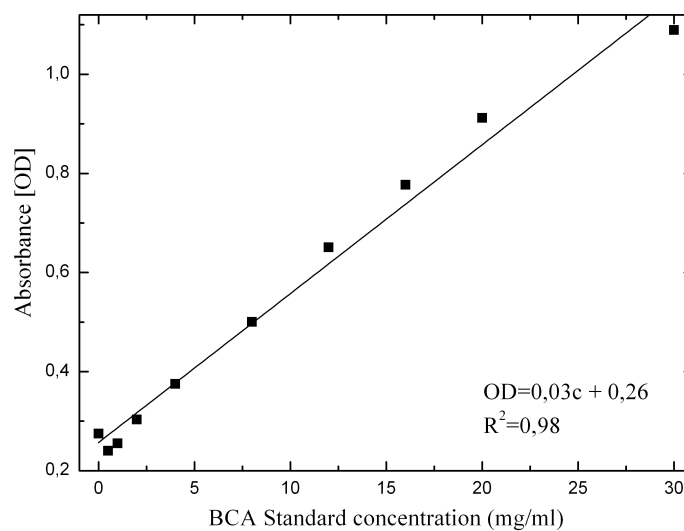


**Figure 6.9:** Standard curve of the BCA protein assay.

**Table 6.3:** Protein concentration on typical samples from NanoDrop and BCA protein assay

Protein	NanoDrop (mg/ml)	BCA protein assay (mg/ml)
<b>CooA WT</b>	10.3	9.0
<b>CooA T189 codon stop</b>	4.8	3.1
<b>ThyX WT</b>	12.9	12.6

## 6.10 Heme binding on DNR

DNR is expressed in the apo-form (with no heme present). Thus heme binding was performed *in vitro* [37]. The apo-protein concentration was determined by use of

the Beer-Lambert Law (as explained in section 6.9) and the sample was incubated (2 hours at room temperature under agitation) with a freshly prepared solution of hemin (Sigma) (50 mM Tris-HCl, pH 7.5, 10 mM NaOH, 0.5 mM hemin) in  $\sim 1:1.5$  stoichiometric excess of hemin. After incubation, the excess of hemin was removed by gel filtration on a Sephadex G-25 (Bio-Rad) and the protein was concentrated to the desired concentration.

Spectra of the heme-reconstituted DNR are shown in Figure 6.8.

## 6.11 Time-resolved visible absorption spectroscopy

The studies in the picosecond and early nanosecond time scale of the geminate recombination of ligands to CooA and DNR were performed by pump-probe experiments, where the pump pulse is used to induce the ligand dissociation. A probe pulse encompassing an appropriate spectral range monitors the pump-induced changes in the absorbance of the sample. The kinetic can be resolved by varying the delay of the pump pulse with respect to the probe pulse.

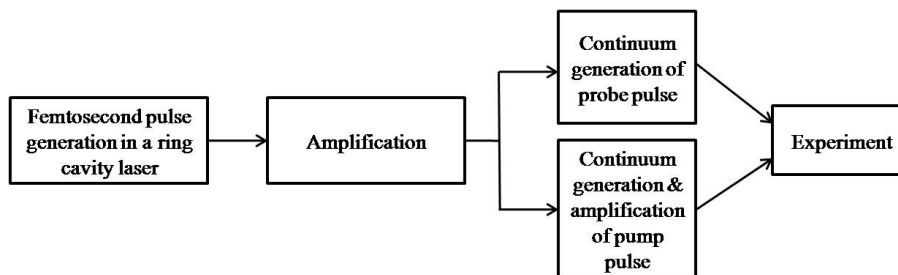


**Figure 6.10:** General scheme of femtosecond pump and probe pulses generation [42].

Figure 6.10 shows the general scheme of the experimental set-up employed. The detailed functioning of the system is explained in [42]. In brief, in a home-built bidirectional ring cavity dye laser, high repetition rate pulses (100 MHz) at 620 nm are generated with a duration of  $\sim 50$  fs and energies in the picojoule range. The rhodamine gain medium (in an ethylene glycol jet) is optically pumped by a continuous-wave (cw), all-solid-state green laser (Verdi G-Series; Coherent, Palo Alto, CA). The output light is then amplified by over six orders of magnitude, obtaining pulses of  $\sim 500 \mu\text{J}$  at a repetition rate of 30 Hz. An injection seeded Nd:YAG (neodymium:yttrium-aluminium-garnet) laser (Quanta Ray, model GCR-4; Spectra Physics) generates pulses of  $\sim 350$  mJ at 532 nm with 7 ns full width at half-maximum which pump the amplifier (in four stages) of the fundamental 620 nm pulses, and

also the pump pulse amplification (two more stages). The Q-switch of the pump laser is triggered by a femtosecond pulse from the oscillator detected by a fast diode (model 4207; Hewlett-Packard, Cupertino, CA) in order to synchronize the peak of the nanosecond YAG pulse with an incoming femtosecond pulse from the ring cavity laser.

After amplification of the pulse, it is compressed by means of a two-prism configuration [130, 131] and the output light is split into two different beams. Both are focused into two independent 8 mm water cells in order to generate white light continua. The intensity of the fundamental beam is adjusted with a variable neutral density filter and a pinhole so as to obtain the most stable continuum in the required spectral range. The pump beam with the spectral properties adapted to excitation in the heme  $\alpha$ -bands is obtained after amplification of a spectral range of  $\sim 10$  nm centered at 560 nm. Selection of the spectral range is done with a filter which removes the fundamental beam centered at 620 nm from the continuum and choice of dye and solvent for amplification.

Figure 6.11 shows the scheme used for relative timing of the pump and probe pulses. The delay between the pump pulse and the probe pulse is varied by means of an optical delay line composed of a retroreflector mounted on a computed-controlled stepper motor (model UT 100.100 PP; Microcontrol, Evry, France) with a step size of 1  $\mu\text{m}$  (1 ps corresponds to a path length of 300  $\mu\text{m}$  or a displacement of the mirrors of 150  $\mu\text{m}$ ) and a total time delay up to 4 ns. The intensity of the pump pulse can be adjusted by neutral-density films so as to stay in the linear photoexcitation regime.

The probe pulse is split in two beams which strictly follow parallel pathways until the entrance in a monochromator (model H 25; Jobin Yvon, Longjumeau, France): the reference and the test beam (not shown in the figure). This feature allows for a significant noise reduction by normalization on a shot-by-shot basis. The test beam is focused into  $\sim 60$   $\mu\text{m}$  of the cell sample while the reference beam does not cross the sample cell.

The pump pulse and the test probe pulse are both focused into the same spot of the cell sample. The overlap is maximized by monitoring the signal in real time. The cell is moved laterally perpendicular to the optical axis of the setup to avoid contributions of long-lived signals and photodamage of the sample. In order to monitor ligand recombination only, the spectral range of the probe pulse must be properly chosen. In our case, the largest spectral changes take place in the Soret region.

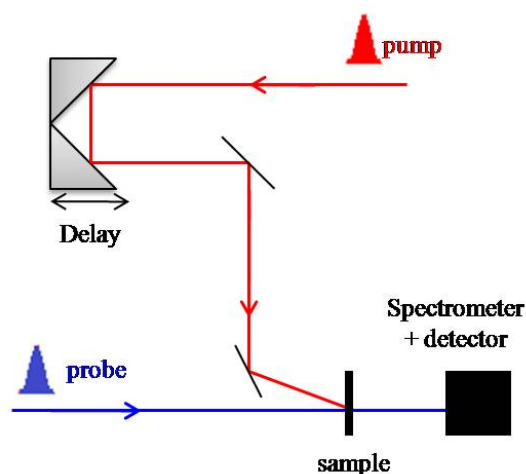


**Figure 6.11:** Scheme for the femtosecond visible absorption setup. This technique allows to monitor dynamics of heme-ligand interactions and also binding kinetics. The pump and the probe pulses are both focused in the cuvette containing the sample. The pump pulse excites the sample, triggering the effect under study. The probe pulse is used to detect the pump-induced absorption changes. The spectrally resolved intensity of the femtosecond probe pulse is recorded as a function of the delay time of the pump pulse, yielding time-resolved spectra after photoexcitation.

## 6.12 Labelling of CooA

In order to label CooA with ATTO-390, with the aim to perform FRET measurements, the Click-iT protein reaction Buffer Kit [132, 133] was used. This click chemistry method consists of a two-step reaction. In the first step, an azide molecule is attached to the protein. The second step uses the chemoselective ligation ("click reaction") between the azido group of the modified protein and the alkyne group of the fluorophore. Figure 6.12 shows this procedure.

Regarding the azide-labelling of the protein, it was demonstrated [134] that a non-natural amino acid can be site-specifically incorporated with good yield and high translational fidelity into proteins by the addition of new orthogonal pairs of t-RNAs and aminoacyl-t-RNA synthetases to the machinery of *E. coli* [120]. In our case, the non-natural amino acid *p*-azido-L-phenylalanine was incorporated in response to the amber codon, TAG. This codon was introduced by site-directed mutagenesis (using the site-directed mutagenesis kit from Agilent) into the pQE60 vector coding for the CooA protein at the following sites: Lys189, Thr149, Leu172 and Asp163. These amino acids were chosen based upon molecular modelling calculations because they were in the C-terminal of the protein and exposed to the surface, in principle facilitating the labelling.

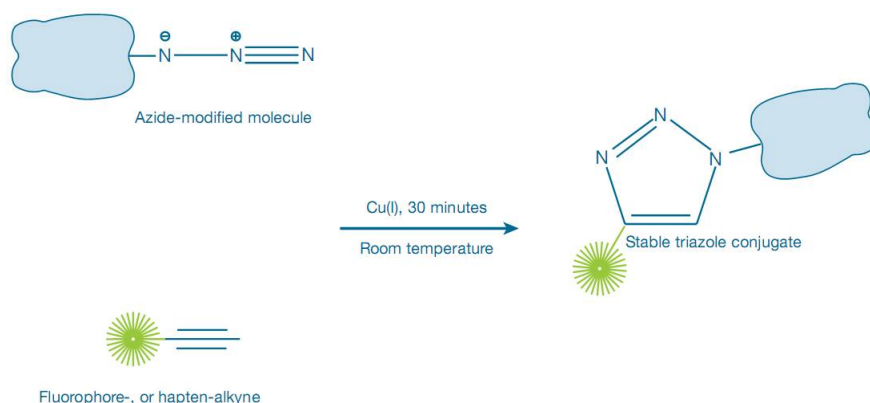


**Figure 6.12:** Click azide/alkyne reaction for protein labelling [133]. The protein is modified so as to incorporate an azide group which will be recognized by the alkyne group of the fluorophore, therefore producing the "click" reaction needed to label the protein. Figure taken from [133].

After verification of the mutation by sequencing, the pQE60-CooA-aa/amber was transformed into BL21(DE3) cells; a co-transformation performed with the pEVOL plasmid which allowed for the integration of the *p*-azido-L-phenylalanine. For the transformation, 50 ng of pQE60-CooA plasmid, 50 ng of pEVOL plasmid and 50  $\mu$ l of BL21(DE3) cells were mixed in a microtube and a thermal shock was performed as explained in section 6.5. Two specific antibiotics were needed in this case: ampicillin (pQE60) at 100  $\mu$ g/ml (final concentration) and chloramphenicol (pEVOL) at 20  $\mu$ g/ml (final concentration).

The expression of the proteins was performed as explained in section 6.6. In this case, due to the co-transformation with pQE60 and pEVOL vectors, induction was performed at  $OD_{600}=0.6$  by addition of IPTG (required for pQE60) and arabinose 0.2% (stock solution at 20%) (required for pEVOL). 1 mM azido-phenyl (stock solution at 10 mM) was also added. The azido-phenyl was prepared in advance by dissolving the powder in distilled water and by slowly adding fresh NaOH until a pH of 7-8. The solution was filtered before use (0.2  $\mu$ m filter).

Once the azido-labelled protein was obtained, we proceeded to the ATTO-labelling by following the Click-iT kit protocol. We first added up to 200  $\mu$ g of the azide-labelled protein in a maximum volume of 50  $\mu$ l of Tris-HCl, pH 8.0. We then added the alkyne-containing detection reagent, which in our case was ATTO-390, at a final concentration of 40  $\mu$ M in a total volume of 160  $\mu$ l (if necessary, we completed to this volume with ultrapure water). The tube was vortexed to obtain a homogeneous solution. We added 10  $\mu$ l of  $CuSO_4$  at an initial concentration of 40 mM and vortexed again. The

cupric sulfate acted as a catalyzer, increasing the yield of the chemical reaction. Next, compounds C and D from the kit (reaction buffer additives) were added at a volume of 10  $\mu\text{l}$  (initial concentration of 80  $\mu\text{g}/\mu\text{l}$ ) and 20  $\mu\text{l}$  (initial concentration of 50  $\mu\text{g}/\mu\text{l}$ ), respectively. After addition of the last compound, the solution turned bright orange. The solution was vortexed and left in a rotator during  $\sim 20$  min (protected from light to avoid dye degradation).

### 6.13 Anisotropy measurements

DNA primers used for these measurements were labelled by EUROGENTEC, and correspond to specific sequence parts for both CooA and DNR. Double stranded DNA was obtained by mixing equimolar amounts of the two complementary oligonucleotides (one strand labelled and the other non-labelled) and heating them above the DNA melting temperature for 3 minutes (in our case, 80°C allows for the complete melting of the DNA). It was then allowed to anneal by slowly cooling down to room temperature.

The forward oligonucleotide specific for CooA corresponds to the 26-base pair 5'-ATAACTGTCATCTGGCCGACAGACGG-3' [65], with the 5' end labelled with either Texas Red or ATTO-390. For purposes of comparison, the reverse strand was also labelled at the 3' end and annealed with the forward non-labelled strand, but this combination yielded less marked anisotropy values.

The binding assays were performed in Tris-HCl, pH 7.6 (50 mM), NaCl (100 mM) buffer. The DNA concentration was 6.4 nM, in principle allowing a binding affinity of  $\sim 15$  nM to be easily resolved (same initial DNA conditions as in [65]). CooA was degased and reduced with 0.5 mM dithionite (final concentration) (Sigma). Gaseous CO was added in order to obtain the CooA-CO complex. DNA was also degased in a gas tight nial and the gas phase filled with CO in order to maintain CO pressure throughout the experiment. The initial solution contained the DNA ligand only, and CooA-CO (final concentration in solution,  $C_f$ ) was added by regular stages from  $C_f = 0\text{nM}$  up to  $C_f = 300\text{nM}$ . The protein stock solution was prepared at  $C_i = 5\mu\text{M}$ , and was injected into the DNA solution using a gas-tight Hamilton syringe. Anisotropy values were determined at each single step (Eq 2.5). The DNA-protein mixing was performed in a 1x1 cm optical path length cuvette fitted in a commercial fluorescence spectrophotometer (Cary Eclipse equipped with a manual polarization device). We respectively used 590nm and 390nm excitation light for Texas Red and ATTO-390, and we measured the fluorescence emission in a wavelength range of  $\sim 50$  nm centered at 615 nm and 480 nm respectively.

For the study of the DNR-DNA affinity, we proceeded in an analogous way. In this case, the specific DNA sequence is the 26-base pair 5'-GGAATCTTGATTGCCATCAAGCGGGT-3' [37], where also the 5' end was labelled. DNR is active in the NO-form, and therefore the protein was equilibrated with 10% NO in the gas phase. At this concentration, the NO-form was fully formed, avoiding degradation of the protein which can occur when higher concentrations of NO are used.

## 6.14 YddV Fe(II)- $O_2$ complex formation

In order to determine the  $O_2$  dissociation at 10 ps in YddV WT and Y43F, the Fe(II)- $O_2$  complex was formed. In this case, to reduce the iron in the heme, we could not use dithionite (since it is an  $O_2$  scavenger). Ascorbate (in a  $C_f \sim 100 \mu M$  in solution) and the mediator ruthenium hexamine ( $\sim 10$  times more diluted than ascorbate) were used to reduce the heme. The cell containing the sample was left opened so that  $O_2$  present in the air ( $\sim 21\%$  [135]) could bind to the heme. The  $\sim 21\%$  of  $O_2$  in the atmosphere corresponds to  $\sim 250 \mu M$  in solution (100% atmospheric oxygen corresponds to 1.2 mM in solution [136]). Therefore, taking into account the  $O_2$   $k_d$  for WT YddV, which is  $16 \mu M$  [28], we can conclude that our sample was fully in the  $O_2$ -form. This was also the case of the mutant Y43F, whose  $k_d$  is  $12 \mu M$ . However, the non-fully  $O_2$ -form obtained in this mutant may be consequence of its high autooxidation rate ( $k_{ox}=0.069 \text{ min}^{-1}$ , being  $\sim 10$  higher than the  $k_{ox}$  of WT YddV) [28].

## 6.15 Time-resolved fluorescence spectroscopy

For the time-resolved fluorescence spectroscopy, we used a setup allowing for the simultaneous measurement of the complete time- and spectrally-resolved fluorescence matrix on a time-scale from  $\sim 100$  fs to few nanoseconds [62].

The optical Kerr effect is due to light-induced anisotropy changes in a non-linear medium (called Kerr medium). Eq. 6.2 gives the change of anisotropy induced by the light pulse; the change in the refractive index in the direction  $\parallel$  and  $\perp$  to the excitation beam being proportional to the light intensity,  $I$ , at the medium [54]:

$$\Delta n = \gamma I, \tag{6.2}$$

where  $\gamma$  refers to the non-linear refractive index.

In Kerr-based fluorescence gating setups, the fluorescence light pathway includes two crossed polarizers between which an isotropic Kerr medium is placed. In the closed state of the setup, light is blocked by the second polarizer. The shutter is opened when a strong, linearly polarized gate pulse excites the Kerr medium, inducing a birefringence and producing therefore a transient rotation of the polarization of fluorescence light which will enable a fraction of the fluorescence to pass through the second polarizer.

Carbon disulfide ( $CS_2$ ) (Sigma-Aldrich) was used as the Kerr medium in this work since it presents a high efficiency in the rotation of fluorescence polarization, allowing for larger signals when compared to other Kerr mediums. The time-resolution (gate opening time) is  $\sim 1$  ps [137, 138], which is larger than the gate pulse duration, because the origin of the Kerr effect is molecular. However, we were interested in studying processes occurring on larger timescales, making therefore this material most suitable for our purpose.

Figure 6.13 shows a schematic representation of the experimental setup. Short light pulses of  $\sim 100$  fs and centered at 800 nm are generated with a Ti:Sapphire femtosecond laser amplification system (Integra-C, Quantronix, Excel Technology). This system provides pulses with an energy of  $\sim 1$  mJ at a repetition rate of 1 kHz. The output of the amplifier is split in two different fractions. One of them is directed into the optical delay line (which will be used as the gate pulse) and the other is used for the generation of the pump pulse after crossing a  $\beta$ -barium borate crystal (BBO) which doubles the frequency, giving pulses centered at 400nm (in resonance with the main absorption band of ATTO-390). In order to avoid anisotropy effects, we set the polarization of the pump pulse at the *magic angle* ( $54.7^\circ$ ) with respect to the position of the first polarizer,  $P_1$ , using a half-wave plate. The pump is directed to the sample by a  $90^\circ$  dichroic mirror, D (which reflects at the excitation wavelength and transmits at the emission spectral range of the sample) and focused by a lens,  $L_1$ , of 5 cm focal length. The sample, S, is contained in a 1 mm quartz cuvette which moves circularly in the plane perpendicular to the optical axis to avoid photodamage of the sample by prolonged illumination of the same spot.

Upon excitation, the fluorescence is emitted in all directions (we assume an isotropic sample). Fluorescence going in the backward direction passes through the dichroic mirror and is collected by a fiber-optic spectrometer,  $SP_2$  (Ocean Optics USB2000+VIS-NIR). Simultaneous collection of the fluorescence at  $SP_2$  with the detection at  $SP_1$  allows for the normalization of total fluorescence fluctuations. Fluorescence emitted

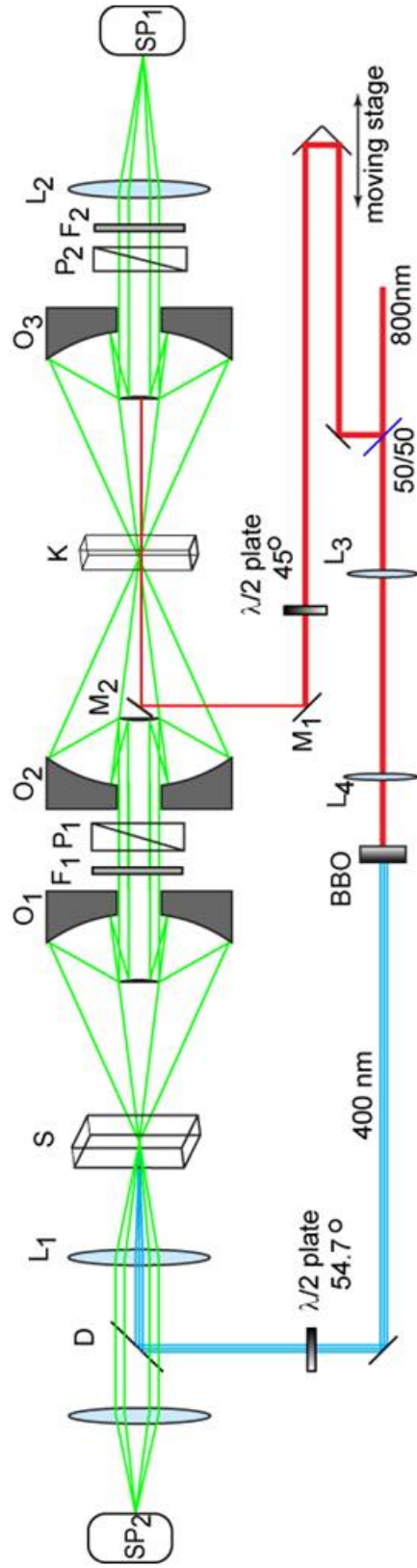


**Figure 6.13:** Schematic representation of the experimental setup. S refers to the sample; K refers to the Kerr cell placed between two crossed polarizers,  $P_1$  and  $P_2$ ;  $O_1, O_2$  and  $O_3$  are the reflective objectives directing the fluorescence; BBO refers to the  $\beta$ -barium borate crystal which generates the double frequency;  $M_1$  and  $M_2$  are mirrors directing the gate pulse respectively;  $F_1$  and  $F_2$  are filters which block the pump beam and the gate pulse respectively;  $SP_1$  indicates the spectrometer connected to a cooled CCD for gated fluorescence detection and  $SP_2$  is a reference spectrometer so as to be able to normalize with respect to the total fluorescence.

in the forward direction is collected by a Cassegrain-type reflective objective,  $O_1$  (Newport 50105-02, effective focal length 13 mm, working distance 24 mm). Reflective optics are used to avoid deterioration of the time-resolution by dispersive optics. Parabolic mirrors are avoided since they introduce depolarization effects which would decrease the signal to noise ratio. After  $O_1$ , the collimated light passes through the vertically-oriented polarizer  $P_1$  (Moxtek PFU04C, thickness 0.7 mm). Linearly polarized light is then collected by the second reflective objective,  $O_2$ , and focused into the Kerr medium, where it is overlapped with the gate beam. The fluorescence that arrives in the Kerr cell simultaneous with (or shortly after, depending on the medium) the gate beam is rotated and the shutter opened. Subsequently, the beam is collimated by a third reflective objective,  $O_3$ . The second polarizer,  $P_2$ , is placed perpendicular to  $P_1$  so that in principle no light can reach the detector unless the system is "gated". Finally, a lens,  $L_2$ , focuses the fluorescence into the entrance slit of the detector spectrograph (Acton, SP2150) and into a nitrogen-cooled CCD (Princeton Instruments, SPEC-10) configured as an array-detector.

## 6.16 Circular dichroism

In order to perform the circular dichroism (CD) measurements, we use a hand-made CD spectrophotometer of local design constructed by L. Mendonça and F. Hache in the LOB.

In this set-up, the light source is a Deuterium lamp which emits a broad spectrum. The desired wavelength is obtained by selection with a UV-Vis monochromator. For the generation of circularly polarized light, alternately at right-hand and left-hand with a frequency of 50 kHz, a linear polarizing filter, placed at  $45^\circ$ , and a photoelastic modulator (PEM) are used [78].

Circularly polarized light crosses the sample and the transmitted light is then detected by a photomultiplier (PM). The PM signal is then sent to a Lock-in amplifier in order to detect the signal at 50 kHz. The Lock-in signal (LI) is proportional to the difference of intensity between the right and the left circularly polarized light, and therefore, the CD can be calculated as [78]:

$$CD = \sqrt{2} \frac{LI}{PM_{av}}, \quad (6.3)$$

where the  $\sqrt{2}$  arises from conversion of the RMS Lock-in amplifier output value (instead of the peak-to-peak), and  $PM_{av}$  refers to the average signal of the PM.

### 6.16.1 Preparation of proteins for the CD measurements

In order to measure the CD spectrum of Mb in the same conditions as CooA and be therefore able to compare both spectra, Mb was solved in MOPS buffer (200 mM MOPS (Sigma-Aldrich), pH 6.5, 80 mM Sodium Acetate and 10 mM EDTA). At pH 6.4, the protein is fully 6-coordinate, with a  $H_2O$  molecule in the distal site (no mixture of 5-c and 6-c heme as at higher pH) [139].

For the reduction of CooA and Mb prior to CO binding, a minimum amount of dithionite has been used, in order to avoid any absorption of the dithionite in the near UV spectrum. The proteins concentration was 40  $\mu M$  in CooA and 25  $\mu M$  in Mb.

# Bibliography

- [1] M. Kajimura, R. Fukuda, R. M. Bateman, T. Yamamoto, and M. Suematsu. Interactions of multiple gas-transducing systems: hallmarks and uncertainties of CO, NO, and  $H_2S$  gas biology. *Antioxid. Redox Signaling*, 13(2):157–92, 2010.
- [2] U. Liebl, J.-C. Lambry, and M. H. Vos. Primary processes in heme-based sensor proteins. *Biochim. Biophys. Acta*, in press.
- [3] M. A. Gilles-Gonzalez and G. Gonzalez. Heme-based sensors: defining characteristics, recent developments, and regulatory hypotheses. *J. Inorg. Biochem.*, 99(1):1–22, 2005.
- [4] The chemistry of hemoglobin and myoglobin. From Purdue University, College of Sciences. <http://chemed.chem.purdue.edu/genchem/topicreview/bp/1biochem/blood3.html>.
- [5] A. Farhana, V. Saini, A. Kumar, J. R. J. Lancaster, and A. J. C. Steyn. Environmental heme-based sensor proteins: implications for understanding bacterial pathogenesis. *Antioxid. Redox Signaling*, 17:1232–45, 2012.
- [6] L. Bouzhir. *Etude des hémoprotéines senseurs à oxygène bactériens FixL et Dos*. PhD thesis, Ecole Polytechnique, Laboratoire d’Optique et Biosciences, INSERM U696, CNRS UMR 7645, ENSTA, 2006.
- [7] S. Aono. Novel Bacterial gas Sensor Proteins with Transition Metal-Containing Prosthetic Groups as Active Sites. *Antioxid. Redox Signaling*, 16(7):678–86, 2012.
- [8] W. Gong, B. Hao, S. S. Mansy, G. Gonzalez, M. A. Gilles-Gonzalez, and M. K. Chan. Structure of a biological oxygen sensor: A new mechanism for heme-driven signal transduction. *Proc. Natl. Acad. Sci.*, 95(26):15177–15182, 1998.

- [9] L. M. Podust, A. Ioanoviciu, and P. R. Ortiz de Montellano. 2.3 x-ray structure of the heme-bound gaf domain of sensory histidine kinase dost of *Mycobacterium tuberculosis*. *Biochem.*, 47(47):12523–12531, 2008.
- [10] W. N. Lanzilotta, D. J. Schuller, M. V. Thorsteinsson, R. L. Kerby, G. P. Roberts, and T. L. Poulos. Structure of the CO sensing transcription activator CooA. *Nat. Struct. Biol.*, 7(10), 2000.
- [11] W. Zhang and G. N. Phillips. Structure of the Oxygen Sensor in *Bacillus subtilis*: Signal Transduction of Chemotaxis by Control of Symmetry. *Structure*, 11(9):1097–1110, September 2003.
- [12] T. H. Tahirov, S. Misaki, T. E. Meyer, M. A. Cusanovich, Y. Higuchi, and N. Yasuoka. High-resolution crystal structures of two polymorphs of cytochrome *c'* from the purple phototrophic bacterium *Rhodobacter capsulatus*. *J. Mol. Biol.*, 259(3):467–479, 1996.
- [13] J. R. Nambu, J. O. Lewis, K. A. Wharton, and S. T. Crews. The drosophila single-minded gene encodes a helix-loop-helix protein that acts as a master regulator of cns midline development. *Cell*, 67(6):1157–1167, 1991.
- [14] E. K. Monson, G. S. Ditta, and D. R. Helinski. The oxygen sensor protein, FixL, of *Rhizobium meliloti*. role of histidine residues in heme binding, phosphorylation, and signal transduction. *J. Biol. Chem.*, 270(10):5243–5250, 1995.
- [15] M. A. Gilles-Gonzalez, G. Gonzalez, M.F. Perutz, L. Kiger, M. C. Marden, and C. Poyart. Heme-based sensors, exemplified by the kinase FixL, are a new class of heme protein with distinctive ligand binding and autoxidation. *Biochem.*, 33(26):8067–73, 1994.
- [16] M. H. Vos. Ultrafast dynamics of ligands within heme proteins. *Biochim. Biophys. Acta*, 1777(1):15–31, 2008.
- [17] W. Gong, B. Hao, and M. K. Chan. New mechanistic insights from structural studies of the oxygen-sensing domain of *Bradyrhizobium japonicum* FixL. *Biochem.*, 39(14):3955–3962, 2000.
- [18] H. Miyatake, M. Mukai, S. Y. Park, S. I. Adachi, K. Tamura, H. Nakamura, K. Nakamura, T. Tsuchiya, T. Iizuka, and Y. Shiro. Sensory mechanism of oxygen sensor FixL from *Rhizobium meliloti*: crystallographic, mutagenesis and resonance raman spectroscopic studies. *J. Mol. Biol.*, 301(2):415–431, 2000.

- [19] V. M. Delgado-Nixon, G. Gonzalez, and M. A. Gilles-Gonzalez. Dos, a heme-binding pas protein from *Escherichia coli*, is a direct oxygen sensor. *Biochem.*, 39(10):2685–2691, 2000.
- [20] Y. Sasakura, S. Hirata, S. Sugiyama, S. Suzuki, S. Taguchi, M. Watanabe, T. Matsui, I. Sagami, and T. Shimizu. Characterization of a direct oxygen sensor heme protein from *Escherichia coli*: Effects of the heme redox states and mutations at the heme-binding site on catalysis and structure. *J. Biol. Chem.*, 277(26):23821–23827, 2002.
- [21] J. R. Tuckerman, G. Gonzalez, E. Sousa, X. Wan, J. Saito, M. Alam, and M. A. Gilles-Gonzalez. An oxygen-sensing diguanylate cyclase and phosphodiesterase couple for C-di-GMP control. *Biochem.*, 48(41):9764–74, October 2009.
- [22] L. G. Wayne and C. D. Sohaskey. Non-replicating persistence of *Mycobacterium tuberculosis*. *Annu. Rev. Microbiol.*, 55(1):139–163, 2001. PMID: 11544352.
- [23] M. H. Vos, L. Bouzahir, H. Lambry, J.-C. Luo, J. J. Eaton-Rye, A. Ioanoviciu, Ortiz de Montellano P. R., and U. Liebl. Ultrafast ligand dynamics in the heme-based GAF sensor domains of the histidine kinases DosS and DosT from *Mycobacterium tuberculosis*. *Biochem.*, 51(1):159–166, 2012.
- [24] H. M. Girvan and A. W. Munro. Heme sensor proteins. *J. Biol. Chem.*, 288(19):13194–13203, 2013.
- [25] S. Aono, H. Nakajima, K. Saito, and M. Okada. A Nobel Heme Protein that Acts as a Carbon Monoxide-Dependent Transcriptional Activator in *Rhodospirillum rubrum*. *Biochem. Biophys. Res. Commun.*, 228(3):752–756, 1996.
- [26] D. Shelver, R. L. Kerby, Y. He, and G. P. Roberts. Carbon monoxide-induced activation of gene expression in *Rhodospirillum rubrum* requires the product of Cooa, a member of the cyclic AMP receptor protein family of transcriptional regulators. *J. Bacteriol.*, 177(8):2157–63, 1995.
- [27] H. Shaobin, R. W. Larsen, D. Boudko, C.W. Riley, E Karatan, M. Zimmer, G.W. Ordal, and M. Alam. Myoglobin-like aerotaxis transducers in archaea and bacteria. *Nature*, 403:540–544, 2000.
- [28] K. Kitanishi, K. Kobayashi, Y. Kawamura, I. Ishigami, T. Ogura, K. Nakajima, J. Igarashi, A. Tanaka, and T. Shimizu. Important roles of Tyr43 at the

- putative heme distal side in the oxygen recognition and stability of the Fe(II)-O<sub>2</sub> complex of YddV, a globin-coupled heme-based oxygen sensor diguanylate cyclase. *Biochem.*, 49(49):10381–93, December 2010.
- [29] J.W. Denninger and M.A. Marletta. Guanylate cyclase and the NO/cGMP signaling pathway. *Biochim. Biophys. Acta, Bioenerg.*, 1411(2-3):334–350, 1999.
- [30] G. P. Roberts, R. L. Kerby, H. Youn, and M. Conrad. CooA, a paradigm for gas sensing regulatory proteins. *J. Inorg. Biochem.*, 99(1):280–92, 2005.
- [31] T. Uchida, H. Ishikawa, S. Takahashi, K. Ishimori, I. Morishima, K. Ohkubo, H. Nakajima, and S. Aono. Heme environmental structure of CooA is modulated by the target DNA binding: Evidence from resonance Raman spectroscopy and CO rebinding kinetics. *J. Biol. Chem.*, 273(32):19988–19992, 1998.
- [32] I. K. Dhawan, D. Shelver, M. V. Thorsteinsson, G. P. Roberts, and M. K. Johnson. Probing the heme axial ligation in the CO-sensing CooA protein with magnetic circular dichroism spectroscopy. *Biochem.*, 38(39):12805–12813, 1999.
- [33] M. Borjigin, H. Li, N. D. Lanz, R. L. Kerby, G. P. Roberts, and T. L. Poulos. Structure-based hypothesis on the activation of the CO-sensing transcription factor CooA. *Acta Crystallogr., Sect. D: Biol. Crystallogr.*, 63:282–7, 2007.
- [34] S. Kumazaki, H. Nakajima, T. Sakaguchi, E. Nakagawa, H. Shinohara, K. Yoshihara, and S. Aono. Dissociation and recombination between ligands and heme in a CO-sensing transcriptional activator CooA. A flash photolysis study. *Int. J. Biol. Chem.*, 275(49):38378–83, December 2000.
- [35] M. H. Vos, A. Battistoni, C. Lechauve, M. C. Marden, L. Kiger, A. Desbois, E. Pilet, E. de Rosny, and U. Liebl. Ultrafast heme-residue bond formation in six-coordinate heme proteins: implications for functional ligand exchange. *Biochem.*, 47(21):5718–23, 2008.
- [36] T. Yamashita, L. Bouzhir, J.-C. Lambry, U. Liebl, and M. H. Vos. Ligand dynamics and early signaling events in the Heme domain of the sensor protein Dos from *Escherichia coli*. *J. Biol. Chem.*, 283(4):2344–2352, 2008.
- [37] G. Giardina, S. Rinaldo, K. a Johnson, A. Di Matteo, M. Brunori, and F. Cutruzzolà. NO sensing in *Pseudomonas aeruginosa*: structure of the transcriptional regulator DNR. *J. Mol. Biol.*, 378(5):1002–15, May 2008.

- [38] G. Giardina, S. Rinaldo, N. Castiglione, M. Caruso, and F. Cutruzzolà. A dramatic conformational rearrangement is necessary for the activation of DNR from *Pseudomonas aeruginosa*. Crystal structure of wild-type DNR. *Proteins Struct. Funct. Bioinf.*, 77(1):174–180, October 2009.
- [39] S. Rinaldo, N. Castiglione, G. Giardina, M. Caruso, A. Arcovito, S. D. Longa, P. D’Angelo, and F. Cutruzzola. Unusual heme binding properties of the dissimilative nitrate respiration regulator, a bacterial nitric oxide sensor. *Antioxid. Redox Signaling*, 17(9):1178–89, 2012.
- [40] V.V. Apanasovich, E.G. Novikov, N.N. Yatskov, R.B.M. Koehorst, T.J. Schaafsma, and A. Hoek. Study of the Zn-porphyrin structure by fluorescence spectroscopy methods. *J. Appl. Spectrosc.*, 66(4):613–616, 1999.
- [41] S. Kuznetsova, G. Zauner, R. Schmauder, O. A. Mayboroda, A. M. Deelder, T. J. Aartsma, and G. W. Canters. A Forster-resonance-energy transfer-based method for fluorescence detection of the protein redox state. *Anal. Biochem.*, 350(1):52–60, 2006.
- [42] J.-L. Martin and M. H. Vos. Femtosecond measurements of geminate recombination in heme proteins. In J. Everse, K. D. Vandegriff, and R. M. Winslow, editors, *Hemoglobins Part C: Biophysical Methods*, volume 232 of *Methods Enzymol.*, pages 416–430. Academic Press, 1994.
- [43] X. Ye, A. Demidov, and P. M. Champion. Measurements of the photodissociation quantum yields of MbNO and MbO<sub>2</sub> and the vibrational relaxation of the six-coordinate heme species. *J. Am. Chem. Soc.*, 124(20):5914–24, 2002.
- [44] W. Wang, X. Ye, A. A. Demidov, F. Rosca, T. Sjodin, W. Cao, M. Sheeran, and P. M. Champion. Femtosecond multicolor pump-probe spectroscopy of ferrous cytochrome *c*'. *J. Phys. Chem. B*, 104(46):10789–10801, 2000.
- [45] S. Cianetti, M. Negrerie, M. H. Vos, J.-L. Martin, and S. G. Kruglik. Photodissociation of heme distal methionine in ferrous cytochrome *c* revealed by subpicosecond time-resolved resonance Raman spectroscopy. *J. Am. Chem. Soc.*, 126(43):13932–13933, 2004.
- [46] S. G. Kruglik, A. Jasaitis, K. Hola, T. Yamashita, U. Liebl, J.-L. Martin, and M. H. Vos. Subpicosecond oxygen trapping in the heme pocket of the oxygen sensor FixL observed by time-resolved resonance Raman spectroscopy. *Proc. Natl. Acad. Sci.*, 104(18):7408–7413, 2007.

- [47] M. H. Vos and J.-L. Martin. Femtosecond processes in proteins. *Biochim. Biophys. Acta*, 1411(1):1–20, 1999.
- [48] U. Liebl, L. Bouzhir, L. Kiger, M. C. Marden, J.-C. Lambry, M. Negrederie, and M. H. Vos. Ligand binding dynamics to the Heme domain of the oxygen sensor Dos from *Escherichia coli*. *Biochem.*, 42(21):6527–6535, 2003.
- [49] E. Pilet, A. Jasaitis, U. Liebl, and M. H. Vos. Electron transfer between hemes in mammalian cytochrome *c* oxidase. *Proc. Natl. Acad. Sci.*, 101(46):16198–16203, 2004.
- [50] J. R. Lakowicz. *Principles of Fluorescence Spectroscopy*. Springer, New York, USA, third edition, 2010.
- [51] E. Haustein and P. Schwille. Trends in fluorescence imaging and related techniques to unravel biological information. *HFSP journal*, 1(3):169–80, 2007.
- [52] J. Krieger, K. Toth, and J. Langowski. *Practical Course Biophysics: Absorption and Fluorescence Spectroscopy, Fluorescence Correlation Spectroscopy*. German Cancer Research Center, Germany. <http://www.dkfz.de/Macromol/teaching/files/fcspractical.pdf>.
- [53] H. Szmajcinski and J. R. Lakowicz. Fluorescence lifetime-based sensing and imaging. *Sens. Actuators*, 29:16–24, 1995.
- [54] S. Arzhantsev and M. Maroncelli. Design and characterization of a femtosecond fluorescence spectrometer based on optical Kerr gating. *Appl. Spectrosc.*, 59(2):206–20, 2005.
- [55] J. Xu and J. R. Knutson. Ultrafast fluorescence spectroscopy via upconversion: Applications to biophysics. *Methods Enzymol.*, 450:159–183, 2008.
- [56] B. Valeur. *Molecular Fluorescence: Principles and Applications*. Wiley-VCH, Germany, 2009.
- [57] Guide to streak cameras, 2002. HAMAMATSU PHOTONICS K.K., Systems Division. <http://www.hamamatsu.com>.
- [58] T. Gustavsson, A. Sharonov, and D. Markovitsi. Thymine, thymidine and thymidine 5'-monophosphate studied by femtosecond fluorescence upconversion spectroscopy. *Chem. Phys. Lett.*, 351(3-4):195–200, 2002.

- [59] A. Cannizzo, O. Bräm, G. Zgrablic, A. Tortschanoff, A. Ajdarzadeh, Oskouei, F. van Mourik, and M. Chergui. Femtosecond fluorescence upconversion setup with broadband detection in the ultraviolet. *Opt. Lett.*, 32(24):3555–3557, Dec 2007.
- [60] X. X. Zhang, C. Wurth, L. Zhao, U. Resch-Genger, N. P. Ernsting, and M. Sajadi. Femtosecond broadband fluorescence upconversion spectroscopy: Improved setup and photometric correction. *Rev. Sci. Instrum.*, 82(6):063108, 2011.
- [61] R. Schanz, S.A. Kovalenko, V. Kharlanov, and N. P. Ernsting. Broad-band fluorescence upconversion for femtosecond spectroscopy. *Appl. Phys. Lett.*, 79(5):566–568, 2001.
- [62] S. P. Laptенок, P. Nuernberger, A. Lukacs, and M. H. Vos. *Subpicosecond kerr-gate spectrofluorometry*. From Fluorescence Spectroscopy and Microscopy: Methods and Protocols. Engelborghs, Y. and Visser, A.J.W.G., Eds., Springer, Berlin, Germany, in press.
- [63] H. Wallrabe and A. Periasamy. Imaging protein molecules using FRET and FLIM microscopy. *Curr. Opin. Biotechnol.*, 16(1):19–27, February 2005.
- [64] N. J. Emptage. Fluorescent imaging in living systems. *Curr. Opin. Pharmacol.*, 1(5):521–5, 2001.
- [65] M. V. Thorsteinsson, R. L. Kerby, M. Conrad, H. Youn, C. R. Staples, W. N. Lanzilotta, T. J. Poulos, J. Serate, and G. P. Roberts. Characterization of variants altered at the N-terminal proline, a novel heme-axial ligand in CooA, the CO-sensing transcriptional activator. *J. Biol. Chem.*, 275(50):39332–8, December 2000.
- [66] Atto 390, <https://www.atto-tec.com/attotecshop/product-info.php?language=en&info=p1-ATTO-390.html>, updated 2011.
- [67] Alexa fluor 488 dye, <http://fr-fr.invitrogen.com/site/fr/fr/home/brands/Molecular-Probes/Key-Molecular-Probes-Products/alexa-fluor/Alexa-Fluor-488-Secondary-Antibodies.html>, 2013.
- [68] A. Fersht. *Structure and Mechanism in Protein Science*. A guide to Enzyme Catalysis and Protein Folding. W.H. Freeman and Company, seventh edition, 1999.

- [69] H. Komori, S. Inagaki, S. Yoshioka, S. Aono, and Y. Higuchi. Crystal structure of CO-sensing transcription activator CooA bound to exogenous ligand imidazole. *J. Mol. Biol.*, 367(3):864–871, 2007.
- [70] S. Chen, J. Vojtechovsky, G. N. Parkinson, R. H. Ebright, and H. M. Berman. Indirect readout of DNA sequence at the primary-kink site in the CAP-DNA complex: DNA binding specificity based on energetics of DNA kinking. *J. Mol. Biol.*, 314(1):63–74, 2001.
- [71] F. Jähnig. Structural order of lipids and proteins in membranes: evaluation of fluorescence anisotropy data. *Proc. Natl. Acad. Sci.*, 76(12):6361–5, 1979.
- [72] T. Heyduk and J. C. Lee. Application of fluorescence energy transfer and polarization to monitor *Escherichia coli* cAMP receptor protein and lac promoter interaction. *Proc. Natl. Acad. Sci.*, 87(5):1744–8, March 1990.
- [73] A. O. Grillo, M. P. Brown, and C. A. Royer. Probing the physical basis for Trp repressor-operator recognition. *J. Mol. Biol.*, 287(3):539–54, April 1999.
- [74] R. A. Copeland. *Enzymes. A practical Introduction to Structure, Mechanism, and Data Analysis*. Wiley-VCH, New York, USA, second edition, 2000.
- [75] N. Castiglione, S. Rinaldo, G. Giardina, and F. Cutruzzolà. The transcription factor DNR from *Pseudomonas aeruginosa* specifically requires nitric oxide and haem for the activation of a target promoter in *Escherichia coli*. *J. Microbiol.*, 155(9):2838–44, 2009.
- [76] E. Rusinova, V. Tretyachenko-Ladokhina, O. E. Vele, D. F. Senear, and J. B. Alexander-Ross. Alexa and Oregon Green dyes as fluorescence anisotropy probes for measuring protein-protein and protein-nucleic acid interactions. *Anal. Biochem.*, 308(1):18–25, September 2002.
- [77] S. Ranjit and M. Levitus. Probing the interaction between fluorophores and DNA nucleotides by fluorescence correlation spectroscopy and fluorescence quenching. *Photochem. Photobiol.*, 88(4):782–791, 2012.
- [78] L. Mendonça. *Dynamique conformationnelle des protéines étudiée par dichroïsme circulaire résolu en temps*. PhD thesis, Ecole Polytechnique, Laboratoire d’Optique et Biosciences, INSERM U696, CNRS UMR 7645, 2013.
- [79] T. Dartigalongue. *Dynamique conformationnelle de la myoglobine suivie par dichroïsme circulaire résolu temporellement*. PhD thesis, Ecole Polytechnique,

Laboratoire d'Optique et Biosciences, INSERM U696, CNRS UMR 7645, ENSTA, 2005.

- [80] S. M. Kelly, T. J. Jess, and N. C. Price. How to study proteins by circular dichroism. *Biochim. Biophys. Acta*, 1751(2):119–139, 2005.
- [81] A. Rodger and B. Nordén. *Circular Dichroism & Linear Dichroism*. Oxford University Press, New York, EEUU, second edition, 2008.
- [82] I. V. Rubtsov, T. Zhang, H. Nakajima, S. Aono, G. I. Rubtsov, S. Kumazaki, and K. Yoshihara. Conformational dynamics of the transcriptional regulator CooA protein studied by subpicosecond mid-infrared vibrational spectroscopy. *J. Am. Chem. Soc.*, 123(41):10056–62, October 2001.
- [83] J. J. Snellenburg, S. P. Liptonok, R. Seger, K. M. Mullen, and I. H. M. van Stokkum. Glotaran: a Java-based Graphical User Interface for the R-package TIMP. *J. Stat. Software*, 49(3):1–22, 2012.
- [84] A. Benabbas, V. Karunakaran, H. Youn, T. L. Poulos, and P. M. Champion. Effect of DNA binding on geminate CO recombination kinetics in the CO-sensing transcription factor, CooA. *J. Biol. Chem.*, 2012.
- [85] M. Puranik, S. B. Nielsen, H. Youn, A. N. Hvitved, J. L. Bourassa, M. Case, C. Tengroth, G. Balakrishnan, M. V. Thorsteinsson, J. T. Groves, G. L. McLendon, G. P. Roberts, J. S. Olson, and T. G. Spiro. Dynamics of carbon monoxide binding to CooA. *J. Biol. Chem.*, 279(20):21096–108, 2004.
- [86] E. R. Henry, J. H. Sommer, J. Hofrichter, W. A. Eaton, and M. Gellert. Geminate recombination of carbon monoxide to myoglobin. *J. Mol. Biol.*, 166(3):443–451, 1983.
- [87] K. Yamamoto, H. Ishikawa, S. Takahashi, K. Ishimori, I. Morishima, H. Nakajima, and S. Aono. Binding of CO at the Pro2 side is crucial for the activation of CO-sensing transcriptional activator CooA: 1H-NMR spectroscopic studies. *J. Biol. Chem.*, 276(15):11473–11476, 2001.
- [88] T. Zhang, I.V. Rubtsov, H. Nakajima, S. Aono, and K. Yoshihara. Effect of mutation on the dissociation and recombination dynamics of CO in transcriptional regulator CooA: A picosecond infrared transient absorption study. *Biochem.*, 45(30):9246–9253, 2006. PMID: 16866371.

- [89] D. Ionascu, F. Gruia, X. Ye, A. Yu, F. Rosca, C. Beck, A. Demidov, J. S. Olson, and P. M. Champion. Temperature-Dependent Studies of NO Recombination to Heme and Heme proteins. *J. Am. Chem. Soc.*, 127(48):16921–16934, 2005.
- [90] M. Negrerie, L. Bouzahir, J.-L. Martin, and U. Liebl. Control of nitric oxide dynamics by guanylate cyclase in its activated state. *J. Biol. Chem.*, 276(50):46815–46821, 2001.
- [91] V. Srajer, L. Reinisch, and P.M. Champion. Protein fluctuations, distributed coupling, and the binding of ligands to the heme proteins. *J. Am. Chem. Soc.*, 110:6656–6670, 1988.
- [92] S. Sardiwal, S. L. Kendall, F. Movahedzadeh, S. G. C. Rison, N. G. Stoker, and S. Djordjevic. A GAF domain in the hypoxia/NO-inducible *Mycobacterium tuberculosis* DosS protein binds Haem. *J. Mol. Biol.*, 353(5):929–936, 2005.
- [93] E. H. S. Sousa, J. R. Tuckerman, G. Gonzalez, and M.-A. Gilles-Gonzalez. DosT and DevS are oxygen-switched kinases in *Mycobacterium tuberculosis*. *Protein Sci.*, 16(8):1708–1719, 2007.
- [94] G. Silkstone, A. Jasaitis, M. T. Wilson, and M. H. Vos. Ligand dynamics in an electron transfer protein. Picosecond geminate recombination of carbon monoxide to heme in mutant forms of cytochrome *c*. *J. Biol. Chem.*, 282(3):1638–49, January 2007.
- [95] G. Silkstone, G. Stanway, P. Brzezinski, and M. T. Wilson. Production and characterisation of Met80X mutants of yeast iso-1-cytochrome *c*: spectral, photochemical and binding studies on the ferrous derivatives. *Biophys. Chem.*, 98(1-2):65–77, 2002.
- [96] P. Brzezinski and M. T. Wilson. Photochemical electron injection into redox active proteins. *Proc. Natl. Acad. Sci.*, 94(12):6176–6179, 1997.
- [97] G. Silkstone, A. Jasaitis, M. H. Vos, and M. T. Wilson. Geminate carbon monoxide rebinding to a *c*-type haem. *Dalton Trans.*, 0:3489–3494, 2005.
- [98] P. F. Flynn, R. J. Bieber Urbauer, H. Zhang, A. L. Lee, and A. J. Wand. Main chain and side chain dynamics of a heme protein:  $^{15}\text{N}$  and  $^2\text{H}$  NMR relaxation studies of *R. capsulatus* Ferrocycytochrome *c2*. *Biochem.*, 40(22):6559–6569, 2001. PMID: 11380250.

- [99] G. V. Louie and G. D. Brayer. High-resolution refinement of yeast iso-1-cytochrome *c* and comparisons with other eukaryotic cytochromes *c*. *J.Mol. Biol.*, 214(2):527–555, 1990.
- [100] M.A. Gilles-Gonzalez. Oxygen signal transduction. *IUBMB Life*, 51(3):165–173, 2001.
- [101] K. Nakajima, K. Kitanishi, K. Kobayashi, N. Kobayashi, J. Igarashi, and T. Shimizu. Leu65 in the heme distal side is critical for the stability of the Fe(II)-O<sub>2</sub> complex of YddV, a globin-coupled oxygen sensor diguanylate cyclase. *J. Inorg. Biochem.*, 108:163–70, March 2012.
- [102] D. Antoniani, P. Bocci, A. Maciag, N. Raffaelli, and P. Landini. Monitoring of diguanylate cyclase activity and of cyclic-di-GMP biosynthesis by whole-cell assays suitable for high-throughput screening of biofilm inhibitors. *Appl. Microbiol. Biotechnol.*, 85(4):1095–1104, 2010.
- [103] D.A. D’Argenio and S.I. Miller. Cyclic di-GMP as a bacterial second messenger. *J. Microbiol.*, 150(8):2497–2502, 2004.
- [104] M. Laberge and T. Yonetani. Common dynamics of globin family proteins. *IUBMB Life*, 59(8-9):528–534, 2007.
- [105] U. Liebl, L. Bouzhir, M. Negrerie, J.-L. Martin, and M. H. Vos. Ultrafast ligand rebinding in the heme domain of the oxygen sensors FixL and Dos: general regulatory implications for heme-based sensors. *Proc. Natl. Acad. Sci.*, 99(20):12771–6, 2002.
- [106] A. Jasaitis, K. Hola, L. Bouzhir, J.-C. Lambry, V. Balland, M.H. Vos, and U. Liebl. Role of distal arginine in early sensing intermediates in the heme domain of the oxygen sensor FixL. *Biochem.*, 45(19):6018–6026, 2006.
- [107] J. C. Owrutsky, M. Li, B. Locke, and R. M. Hochstrasser. Vibrational relaxation of the CO stretch vibration in hemoglobin-CO, myoglobin-CO, and protoheme-CO. *J. Phys. Chem.*, 99(13):4842–4846, 1995.
- [108] L. Jia, C. Bonaventura, J. Bonaventura, and J.S. Stamler. S-nitrosohaemoglobin: a dynamic activity of blood involved in vascular control. *Nature*, 380(6571):221–226, 1996.
- [109] V.L. Dawson. Nitric oxide: Role in neurotoxicity. *Clin. Exp. Pharmacol. Physiol.*, 22(4):305–308, 1995.

- [110] J. Park, T. Lee, J. Park, and M. Lim. Photoexcitation dynamics of NO-bound ferric myoglobin investigated by femtosecond vibrational spectroscopy. *J. Phys. Chem. B*, 117(10):2850–2863, 2013.
- [111] D. M. Lawson, C.E.M. Stevenson, C. R. Andrew, and R. R. Eady. Unprecedented proximal binding of nitric oxide to heme: implications for guanylate cyclase. *EMBO*, 19(21):5661–5671, 2000.
- [112] J.W. Petrich, J.-C. Lambry, K. Kuczera, M. Karplus, C. Poyart, and J.-L. Martin. Ligand binding and protein relaxation in heme proteins: a room temperature analysis of NO geminate recombination. *Biochem.*, 30(16):3975–87, 1991.
- [113] S. Kim, G. Jin, and M. Lim. Dynamics of geminate recombination of NO with myoglobin in aqueous solution probed by femtosecond mid-IR spectroscopy. *J. Phys. Chem. B*, 108(52):20366–20375, 2004.
- [114] M. K. Ellison, C. E. Schulz, and W. R. Scheidt. Nitrosyliron (iii) porphyrinates: Porphyrin core conformation and FeNO geometry. Any correlation? *J. Am. Chem. Soc.*, 124(46):13833–13841, 2002. PMID: 12431114.
- [115] G. Silkstone, S. M. Kapetanaki, I. Husu, M. H. Vos, and M. T. Wilson. Nitric oxide binding to the cardiolipin complex of ferric cytochrome *c*. *Biochem.*, 51(34):6760–6, 2012.
- [116] J. Miksovská, C. Suquet, J.D. Satterlee, and R.W. Larsen. Characterization of conformational changes coupled to ligand photodissociation from the heme binding domain of FixL. *Biochem.*, 44(30):10028–10036, 2005.
- [117] T. Parsons. *XL1-Blue competent cells*, Stratagene, An Agilent Technologies division, 2011.
- [118] *BL21 (DE3) Competent Cells*, Technologies, Agilent. [http://www.chem.agilent.com/en-US/Search/Library/\\_layouts/Agilent/PublicationSummary.aspx?whid=72542&liid=6327](http://www.chem.agilent.com/en-US/Search/Library/_layouts/Agilent/PublicationSummary.aspx?whid=72542&liid=6327), 2012.
- [119] J. H. Miller. *Experiments in Molecular Genetics*. Cold Spring Harbor Laboratory Press, New York, 1972.
- [120] T. S. Young, I. Ahmad, J. Yin, and P. G. Schultz. An enhanced system for unnatural amino acid mutagenesis in *E. coli*. *J. Mol. Biol.*, 395(2):361–74, 2010.
- [121] *Plasmid DNA purification*, Macherey-Nagel. [www.m-net.com](http://www.m-net.com), 2010.

- [122] J. Sambrook, E. F. Fritsch, and T. Maniatis. *Molecular Cloning*. A Laboratory Manual. Cold Spring Harbor Laboratory Press, New York, second edition, 1989.
- [123] *QuikChange II Site-Directed Mutagenesis Kit*, <http://www.chem.agilent.com/Library/usermanuals/Public/200521.pdf>, revised 2012.
- [124] *Purification of Polyhistidine-Tagged Proteins*, Macherey-Nagel. [www.mn-net.com](http://www.mn-net.com), 2006.
- [125] J. E. Coligan, B. M. Dunn, D. W. Speicher, and P. T. Wingfield. *Short Protocols in Protein Science*. A Compendium of Methods from Current Protocols in Protein Science. John Wiley & Sons, 2003.
- [126] Expasy sib bioinformatics resource portal, <http://www.expasy.org/genomics>, Updated 2012.
- [127] W. W. Parson. *Modern Optical Spectroscopy*. With Exercises and Examples from Biophysics and Biochemistry. Springer-Verlag, Heidelberg, Germany, first student edition, 2009.
- [128] D. Shelver, R. L. Kerby, Y. He, and G. P. Roberts. CooA, a CO-sensing transcription factor from *Rhodospirillum rubrum*, is a CO-binding heme protein. *Proc. Natl. Acad. Sci.*, 94(21):11216–20, October 1997.
- [129] P. K. Smith, R. I. Krohn, G. T. Hermanson, A. K. Mallia, F. H. Gartner, M. D. Provenzano, E. K. Fujimoto, N. M. Goeke, B. J. Olson, and D. C. Klenk. Measurement of protein using bicinchoninic acid. *Anal. Biochem.*, 150(1):76–85, 1985.
- [130] R. L. Fork, O. E. Martinez, and J. P. Gordon. Negative dispersion using pairs of prisms. *Opt. Lett.*, 9(5):150–152, May 1984.
- [131] A. Migus, C. V. Shank, E. P. Ippen, and R. L. Fork. *IEEE J. Quantum Electron.*, 18(101), 1982.
- [132] R. Breinbauer and M. Kohn. Azide Alkyne Coupling: A Powerful Reaction for Bioconjugate Chemistry. *ChemBioChem*, 4(11), 2003.
- [133] *Click-iT Protein Reaction Buffer Kit*, Invitrogen, MP10276. <http://tools.invitrogen.com/content/sfs/manuals/mp10276.pdf>, 2010.
- [134] W. Chin, S. W. Santoro, A. B. Martin, D. S. King, L. Wang, and P. G. Schultz. Addition of *p*-azido-l-phenylalanine to the genetic code of *Escherichia coli*. *J. Am. Chem. Soc.*, 124(31):9026–9027, 2002.

- [135] What is the chemical composition of air?, Extracted from CRC Handbook of Chemistry and Physics, edited by David R. Lide, 1997. <http://chemistry.about.com/od/chemistryfaqs/f/aircomposition.htm>, updated 2013.
- [136] C. M. Harris and V. Massey. The reaction of reduced xanthine dehydrogenase with molecular oxygen: Reaction kinetics and measurement of superoxide radical. *J. Biol. Chem.*, 272(13):8370–8379, 1997.
- [137] E. P. Ippen and C. V. Shank. Picosecond response of a high-repetition-rate CS optical Kerr gate. *Appl. Phys. Lett.*, 26(3):92–93, 1975.
- [138] H. Kanbara, H. Kobayashi, T. Kaino, T. Kurihara, N. Ooba, and K. Kubodera. Highly efficient ultrafast optical Kerr shutters with the use of organic nonlinear materials. *J. Opt. Soc. Am. B*, 11(11):2216–2223, Nov 1994.
- [139] E. Antonini and M. Brunori. *Hemoglobin and Myoglobin in their Reactions with Ligands*. North Holland - American Elsevier Publishing Co., Netherlands, first edition, 1971.

## RESUMÉ

Des protéines à base de l'hème sont impliquées dans une large gamme de fonctions biologiques, y compris la respiration, le transport de l'oxygène et la détoxification des xénobiotiques. Surtout, les protéines senseurs bactériens à base de l'hème exploitent les propriétés de liaison de l'hème pour détecter les gaz environnementaux. Cette thèse focalise sur l'étude de la dynamique interne des hémoprotéines senseurs à gaz 6-coordonnées CooA, de *Rhodospirillum rubrum* et DNR de *Pseudomonas aeruginosa*, qui sont impliquées dans l'adaptation du métabolisme de l'organisme à son environnement. CooA et DNR sont des facteurs de transcription qui se lient à l'ADN lors de l'activation par des molécules diatomiques gazeuses, permettant ainsi à la transcription de gènes spécifiques. Les deux protéines senseur potentiellement subissent un important changement conformationnel délocalisé lors de la liaison du ligand physiologique à l'hème (CO pour CooA et NO pour DNR). Ici des techniques avancées de spectroscopie optique sont utilisées pour étudier le mécanisme et la voie moléculaire de l'activation / désactivation dans cette classe de protéines.

Des interactions protéine-ADN ont été étudiées avec des techniques de fluorescence à l'équilibre et ultrarapide femtoseconde, en utilisant des substrats d'ADN marqués. Une liaison de l'ADN, sensible au ligand physiologique, dans la gamme d'affinité nanomolaire a été déduite des expériences d'anisotropie. Du « quenching » de la fluorescence du marqueur fluorescent par transfert d'énergie à l'hème natif a été observée et la vitesse de ce processus, qui reflète la distance hème-substrat, a été déterminé directement des cinétiques mesurées de la fluorescence.

Des expériences d'absorption femtosecondes transitoires ont été réalisées afin d'étudier la dynamique de ligands dans CooA et DNR proche de l'hème. Dans DNR, après photodissociation de NO, une recombinaison géminée particulièrement rapide et efficace a été observée. Cela renforce fortement l'hypothèse que des senseurs à NO agissent comme des pièges à ligands. En outre, les barrières énergétiques liées à la migration de CO ont été déterminées dans les deux protéines senseurs par des études de la dépendance de la température. Toutes les protéines senseurs 6-coordonnées, qui fonctionnent par l'échange d'un résidu interne et de la molécule de gaz en tant que ligand de l'hème, démontrent une recombinaison sans barrières et une évation thermiquement activée du CO de la poche de l'hème. En revanche, la barrière pour l'évasion du CO apparaît plus faible ou même absente pour les systèmes 5-coordonnées, comme cela a été trouvé pour le senseur à hème mycobactérien DosT. Pour des raisons de comparaison, les barrières énergétiques ont également été étudiées dans la protéine de transfert d'électrons cytochrome *c*. Ici, un mécanisme plus complexe de barrières multiples a été déduit. Cette propriété est proposée de provenir de la nature plutôt rigide de cette protéine non-senseur, qui contient un hème 6-coordonnée et est dépourvu de voies d'entrée de ligand à l'état natif.

Enfin, les processus primaires dans les domaines de l'hème, de type sauvage et de mutants, du senseur à oxygène YddV, récemment découvert dans *Escherichia coli*, ont été étudiés. En particulier, un rôle important dans la dynamique de ligands a été élucidé pour le résidu tyrosine distale. Ce résidu, qui forme des liaisons hydrogène avec O<sub>2</sub> et NO liés à l'hème, a un effet remarquablement discriminant: après dissociation respective de l'hème, il assiste fortement à la reliaison de l'O<sub>2</sub>, mais favorise l'évasion du NO de la poche de l'hème.

### Mots-clés :

1. Protéines senseurs à base d'hème
2. Dynamique des ligands
3. Barrières énergétiques
4. CooA
5. DNR
6. YddV
7. Spectroscopie ultrarapide
8. Fluorescence

## ABSTRACT

Heme-proteins are involved in a large range of biological functions, including respiration, oxygen transport and xenobiotic detoxification. Importantly, bacterial heme-based sensor proteins exploit the ligation properties of heme to sense environmental gases. This thesis focuses on internal dynamics studies of the 6-coordinate heme-based gas sensor proteins CooA, from *Rhodospirillum rubrum* and DNR from *Pseudomonas aeruginosa* that are involved in adaptation of the metabolism of the organism to their environment. CooA and DNR, belonging to the important family of catabolite gene activator proteins, are transcription factors that bind DNA upon gas activation, thus enabling transcription of specific genes. Both sensor proteins are thought to undergo a large and delocalized conformational change upon binding of the physiological ligand to the heme (CO for CooA and NO for DNR). Here advanced optical spectroscopy techniques are used to investigate the mechanism and molecular pathway of activation/desactivation in this class of proteins.

DNA-protein interactions were studied with steady-state and femtosecond ultrafast time resolved fluorescence techniques, using labeled DNA substrates. Physiological ligand-sensitive DNA binding in the nanomolar affinity range was deduced from anisotropy experiments. Quenching of the fluorescence label by energy transfer to the native heme in the protein moiety of the complex was observed, and the rate of this process, reflecting the heme-substrate distance, was determined directly from the measured fluorescence decays. This observation opens the perspective of mapping out the global protein conformational changes using time-resolved FRET techniques.

The primary processes in heme-based sensor switching mechanisms concern ligand binding and ligand dissociation from the heme. Femtosecond transient absorption experiments were performed in order to study the ligand dynamics in CooA and DNR in the vicinity of the heme. In DNR, upon photodissociation of NO, particularly fast and efficient geminate recombination was observed. This strongly strengthens the hypothesis that NO-sensors act as ligand traps. Also, the energetic barriers involved in CO migration have been determined in both sensor proteins by temperature dependence studies. All 6-coordinate heme-based sensor proteins that function via the exchange of an internal residue and the gas molecule as a heme ligand, display barrierless recombination and a thermally activated CO-escape out of the heme pocket. By contrast, the barrier for the CO-escape appears smaller or absent for 5-coordinate systems, as has been found for the mycobacterial heme-sensor DosT. These findings point to a general mechanism, where similar protein motions are required for both, ligand *exchange* and ligand *escape*. For reasons of comparison, the energetic barriers have also been studied in ligand binding variants of the electron transfer protein cytochrome *c*. Here, a more complex mechanism of multiple barriers in the ligand escape pathway was deduced. This feature is proposed to reflect the rather rigid nature of this non-sensor protein, which contains a 6-coordinate heme and is devoid of ligand entry pathways in the native state.

Finally, the primary processes occurring in the wild type and mutant heme domains of the recently discovered oxygen sensor YddV from *Escherichia coli* were investigated. In particular, an important role in the ligand dynamics was elucidated for the distal tyrosine residue. This residue hydrogen bonds to heme-bound O<sub>2</sub> and NO molecules and was found to have a remarkably discriminating effect: after respective dissociation from the heme, it strongly promotes O<sub>2</sub> rebinding, but favors NO escape from the heme pocket.

### Key words:

1. Heme-based sensor proteins
2. Ligand dynamics
3. Energetic barriers
4. CooA
5. DNR
6. YddV
7. Ultrafast spectroscopy
8. Fluorescence